Irregular Rupture Evolution During the Large/Great Earthquakes: Resolved by High-Frequency Radiation Sources and Co-seismic Slip Distribution

January 2019

Ryo OKUWAKI

Irregular Rupture Evolution During the Large/Great Earthquakes: Resolved by High-Frequency Radiation Sources and Co-seismic Slip Distribution

A Dissertation Submitted to

the Graduate School of Life and Environmental Sciences,

the University of Tsukuba

in Partial Fulfillment of the Requirements

for the Degree of Doctor of Philosophy in Science

(Doctoral Program in Earth Evolution Sciences)

Ryo OKUWAKI

Contents

Irregular Rupture Evolution During the Large/Great Earthquakes: Resolved by High-Frequency Radiation Sources and Co-seismic Slip Distribution

Abstract

Earthquake is a dynamic shear rupture on a fault surface. Detailed imaging by using the real seismic waveforms is crucial to understand diverse rupture evolution during an earthquake. Waveform backprojection (BP) has been used for unwrapping the hidden irregularity of the rupture-front propagation during the large and great earthquakes by tracking the spatiotemporal locations of the high-frequency radiation sources. Such advances in our capability of rupture imaging have been made by the BP's applicability to the high-frequency waveforms since high-frequency radiation is induced by the sudden change of the rupture-front propagation. However, the causality of the irregular rupture propagation and the high-frequency radiation has been still unclear due to the limited resolution of the BP image. Furthermore, the BP image has a possible bias, which may be critical for evaluating the widely-accepted idea of the depth-dependent rupture segmentation of the subduction zone.

This dissertation is devoted to exploring the causal relationship between the high-frequency radiation and the irregular rupture propagation, by focusing on examining the role of barrier in a fault system, which is thought as the main cause of rupture irregularity. Rupture processes of the M_W 7.9 2008 Wenchuan, China and the M_W 8.3 2015 Illapel, Chile, earthquakes are studied by using a hybrid backprojection (HBP) method; a variant of the BP techniques that enhances the image resolution. The analyses of these earthquakes highlight the significant role of the two end-members of the barriers;

geometric and inhomogeneous barriers, which are characteristics of the fault system of the inland and subduction zone earthquakes, respectively. Intense high-frequency radiations and the scattering of slip vectors are observed at the geometric barriers (fault-segment boundaries), suggesting that the rupture propagation is decelerated, and the resultant stress concentration may trigger and accelerate the subsequent rupture across the barrier. We also show that the inhomogeneous barrier (heterogeneity of fault strength without obvious geometrical discontinuity), also controls the irregular rupturing paths in a manner of avoiding the barrier, resulting in up- and down-dip-zigzagging migration of the rupture front.

The latter half of this dissertation is assigned to the review of the mathematical expressions and the clarification of the meaning of the BP and HBP images, revealing that the signal intensity of the BP and HBP images is proportional to the amplitude of the Green's function, which results in the signal intensity being depth dependent and not directly comparable to the slip motion. Thus, the BP and HBP images are inherently biased when they are used for discussing slip motion, and the widely-accepted idea of the depth-dependent rupture property of the subduction zone megathrust earthquakes may not be valid. In order to relate the BP and HBP images to slip motion on a fault surface, the variant BP techniques, called kinematic BP and HBP methods, are proposed. The original BP and HBP images remain useful for assessing the spatiotemporal strength of the wave radiation, which is related to the amplitude of the Green's function, whereas the kinematic BP and HBP methods are suitable for imaging the slip motion that is responsible for the high-frequency radiation produced during the rupture process.

Keywords: Earthquake rupture, Rupture irregularity, High-frequency radiation, Uncertainty in source imaging, Backprojection, Waveform inversion

List of Figures

List of Tables

1 | General introduction

Earthquake is one of the intense geophysical phenomena, which can be described as a dynamic shear rupture along the fault interface (e.g., Aki and Richards, 2002). Resolving the spatial and temporal evolution of the earthquake rupture in detail with observation data has long been an endeavor since 1970s (e.g., Trifunac, 1974). One principal tool for rigorous imaging of the earthquake rupture is waveform inversion (e.g., Olson and Apsel, 1982; Hartzell and Heaton, 1983; Ji et al., 2002; Yagi and Fukahata, 2011a). It resolves the spatiotemporal dislocation of fault (slip) in a finite parametric model space, by sufficiently reproducing the observed waveforms at the Earth's surface. The waveform inversion has widely been used to prove the heterogeneous distribution of slip (e.g., Beroza and Spudich, 1988), and the kinematic information drawn from the data has been indispensable for evaluation of the dynamic simulation of earthquake rupture and the laboratory experiments (e.g., Quin, 1990; Miyatake, 1992; Okubo and Dieterich, 1984).

However, in practice, the waveform inversion suffers from the non-uniqueness of the resultant slip distribution. The slip model of an earthquake is often different from the ones obtained from the different researches and different inversion schemes (Beresnev, 2003; Mai et al., 2017). The inversion procedure requires the modeling constraints for adequately representing the slip in a finite model space and stabilize the solution; for example, rupture extents, rupture velocity, slip function on a discretized source node, and the Green's function. The inappropriate selection of such constraints often violates the inversion solution and makes it non-unique, and especially, the uncertainty of the Green's function is the main source of modeling error (Yagi and Fukahata, 2011a). Due to our insufficient knowledge of the Earth's interior, it is basically difficult to rigorously

represent the Green's function; a response due to an internal force (unit slip along the fault) to a receiver (station on an Earth's surface). Introducing the uncertainty of the Green's function into the data covariance matrix has been the fundamental utilization in the inversion scheme for mitigating the effects of the uncertainty of the Green's function (Yagi and Fukahata, 2011a; Minson *et al.*, 2013; Duputel *et al.*, 2014).

Due to the inevitable requirement for the adequate reproduction of waveforms in the source inversion, however, the frequency range where the waveform inversion can be applied is limited to the low frequency (e.g., Okuwaki *et al.*, 2014). According to the theoretical studies, the higher-frequency waves (above 1 Hz) are generated by the abrupt change of the rupture-front velocity and/or slip rate (Madariaga, 1977; Bernard and Madariaga, 1984; Spudich and Frazer, 1984; Madariaga *et al.*, 2006; Beresnev, 2017), which is a key phenomenon to understand the detailed and complex rupture evolution that may not be well captured by using the waveform inversion. Thus, tracking when, where, and how the high-frequency waves are radiated from the source region during the earthquake should be critical for the more detailed, finer-scale imaging of the earthquake rupture process.

To overcome the difficulty in handling the higher-frequency waveforms, and to clarify more detailed rupture evolution, waveform backprojection (BP) (Ishii *et al.*, 2005, 2007) has been a strong tool for the last 15 years in the source-imaging community. For the BP method, imaging the spatiotemporal evolution of the high-frequency sources is made by just staking (summing) the observed waveforms that are shifted by the theoretical travel times of the possible source locations. Based on the relative strength of the coherency of the stacked waveforms, the spatiotemporal location of the wave-radiation sources can be obtained, which is often referred to the similar idea of the computerized tomography (CT) scanning in the medical field. With the prominent feature of the BP method that does not need to reproduce observed waveforms, the BP can be applied to the higher-frequency waveforms. After the successful application to the M_W 9.2 2004 Sumatra-Andaman earthquake (Ishii *et al.*, 2005), the BP has been useful for easy-estimate of the spatiotemporal evolution of earthquake rupture, which has been overlooked by analyses

of low-frequency waveforms by kinematic source inversion alone, including, for example, irregular rupture migration within the complex fault system (e.g., Uchide *et al.*, 2013; Okuwaki and Yagi, 2018), cascade evolution of asperity ruptures (e.g., Okuwaki *et al.*, 2014, 2016), triggering of very early aftershocks (e.g., Kiser and Ishii, 2013; Fan and Shearer, 2016), multiple branching ruptures (e.g., Meng *et al.*, 2012b; Fan *et al.*, 2016), frequency-dependent wave radiation of subduction zone megathrust earthquakes (e.g., Kiser and Ishii, 2011; Yao *et al.*, 2013; Satriano *et al.*, 2014; Yin *et al.*, 2016), and mechanisms of deep earthquakes (Suzuki and Yagi, 2011; Kiser *et al.*, 2011; Ye *et al.*, 2013).

Following the development of the BP method, a hybrid BP (HBP) method has been proposed by Yagi *et al.* (2012a). The HBP method improves the original BP method by mitigating the dummy imaging of the depth phases (pP and sP phases), which distorts the temporal distribution of the high-frequency radiation (Yagi *et al.*, 2012a; Okuwaki *et al.*, 2014), by introducing the cross-correlation function between the observed waveforms and theoretical Green's function (a detailed description of the HBP method is appeared on chapter 3). The HBP method can be applied to the globally observed stations that cover the large variation of the radiation pattern, which improves the spatial resolution of projected image upon the original BP image.

The series of development of the BP techniques has made it possible to track the high-frequency radiation sources, and opened a window into the extreme complexity of the earthquake rupture process (e.g., Meng *et al.*, 2012b). However, clarifying the deterministic relationship between the high-frequency radiation and the irregularity in rupture propagation is still left unsettled in the observational side. One critical factor that controls the rupture irregularity is *barrier*. The barrier is the geometrical and/or mechanical discontinuity of the strength of the fault (e.g., Aki, 1979), but its role on the rupture irregularity is not well captured in the observations, even by the BP method. In the chapter 2, we tackled on this problem. We further developed the HBP technique, in which we explicitly assumed the complex geometry of the fault segments and allowed the spatiotemporal variation of the rake angle, which make it possible to connect the irregular

rupture evolution and the geometrical discontinuity of the fault system. We clarified the deterministic relationship between the rupture irregularity and the geometric barriers through the application of the refined HBP method (Yagi *et al.*, 2012a; Okuwaki *et al.*, 2014) to the M_W 7.9 2008 Wenchuan, China, earthquake. We also tried to clarify the role of the inhomogeneous barrier, which is another end-member of the barrier of spatial heterogeneity of strength without obvious geometric discontinuity of fault system. We analyzed the source process of the M_W 8.3 2015 Illapel, Chile, earthquake, with the integrated use of the HBP method and the waveform inversion, by evaluating the migration of the high-frequency sources within the smooth slip area and the region of the dense, swarm earthquake, which may work as the inhomogeneous barrier.

Uncertainty in the BP image is another fundamental problem in earthquake source imaging, that is left unsolved. As introduced above, there are plenty of studies that documented the source evolution related to the high-frequency radiation. The easiness of computation and the robustness of the result are enough for making the BP method so popular in the earthquake source imaging community, and today, the BP method is even utilized as the automatic routine of estimating the rupture extent of large earthquakes (Incorporated Research Institutions for Seismology Data Services Products: BackProjection; https://ds.iris.edu/ds/products/backprojection/). However, behind such a popularity of the BP method, the physical meaning of the BP image and the theoretical background of the BP method, that are essential bases for discussing the rupture property through the BP image, are still ambiguous. The accumulation of the BP observations in the last decade has been used to deduce the well-known idea of the rupture segmentation along depth of the subduction zone (e.g., Lay *et al.*, 2012), together with the comparison of the co-seismic slip distribution resolved by the waveform inversion. Based on the spatial relationship of the intense high-frequency sources located along the down-dip part of the large slip zone, the depth-dependent rupture property has been proposed in the subduction zone megathrust earthquakes. However, we have little basis of the theoretical background and/or uncertainty of the BP method, which can be used to evaluate the idea of the rupture segmentation. In the last five years, kicked off by

the pioneering study of Fukahata *et al.* (2014), clarifying the theoretical background of the BP method and the hidden uncertainty/bias in the BP image has been an active research field in the source imaging community (e.g., Meng *et al.*, 2016; Fan and Shearer, 2017). In chapter 3, we clarified the theoretical background of the BP and HBP methods, and found that the BP and HBP images have inherent depth-dependent bias. Plus, we proposed the variants of the BP and HBP methods that suppress the depth-dependent bias, which may provide the more intuitive view of the earthquake rupture process, that is consistent with the theoretical knowledge of the high-frequency radiation.

The deterministic relationship between the irregularity of earthquake rupture and the geometric/inhomogeneous barriers would provide the better constraints for the hazard assessment of future large earthquakes, since the resonant frequencies of buildings lie in the frequency band for the high-frequency waves applied in this thesis (Clinton, 2006; Snieder and Şafak, 2006; Kohler *et al.*, 2007). Observational basis for the relationship between rupture irregularity and the barriers may highlight the importance for integration of the seismological data with the different types of observation in a wide scale range, such as geological and geodetic information including the satellite images, which may provide primary sources for the barrier or extrinsic factor that controlls the complex earthquake-rupture propagation. Irregular, complex rupture evolution, in the various tectonic settings (e.g., intraslab and oceanic transform fault; Okuwaki and Yagi, 2017; Hicks *et al.*, In prep.; Okuwaki *et al.*, In prep.), has been recently reported from the works using the newly developed waveform inversion (Shimizu *et al.*, In prep.). Better imaging techniques for the high-frequency waveforms developed in this thesis, will be used for evaluating such independent findings in a various tectonic settings for the unified understanding of the earthquake source physics.

The author notes that some chapters in this dissertation are based upon the following published articles:

Okuwaki, R. and Yagi, Y., 2018. Role of geometric barriers in irregular-rupture evolution during the 2008 Wenchuan earthquake, *Geophys. J. Int.*, **212**(3), 1657–1664, doi:10.1093/gji/ggx502.

Okuwaki, R., Yagi, Y., Aránguiz, R., González, J., and González, G., 2016. Rupture Process During the 2015 Illapel, Chile Earthquake: Zigzag-Along-Dip Rupture Episodes, *Pure Appl. Geophys.*, **173**(4), 1011–1020, doi:10.1007/s00024-016-1271-6.

Okuwaki, R., Kasahara, A., Yagi, Y., Hirano, S., and Fukahata, Y., 2019. Backprojection to image slip, *Geophys. J. Int.*, **216**(3), 1529–1537, doi:10.1093/gji/ggy505.

2 | Barriers and rupture irregularity

How an earthquake rupture evolves; including nucleation, acceleration, deceleration and/or termination are fundamental questions in earthquake source physics. The idea of *barrier* (Das and Aki, 1977; Aki, 1979) is one of the critical factors for answering these questions. In this chapter, we show that two types of barrier; geometric barrier and inhomogeneous barrier (Fig. 2.1), should play a key role on controlling the irregular rupture evolution, through the detailed analyses of the M_W 7.9 2008 Wenchuan, China and the M_W 8.3 2015 Illapel, Chile, earthquakes.
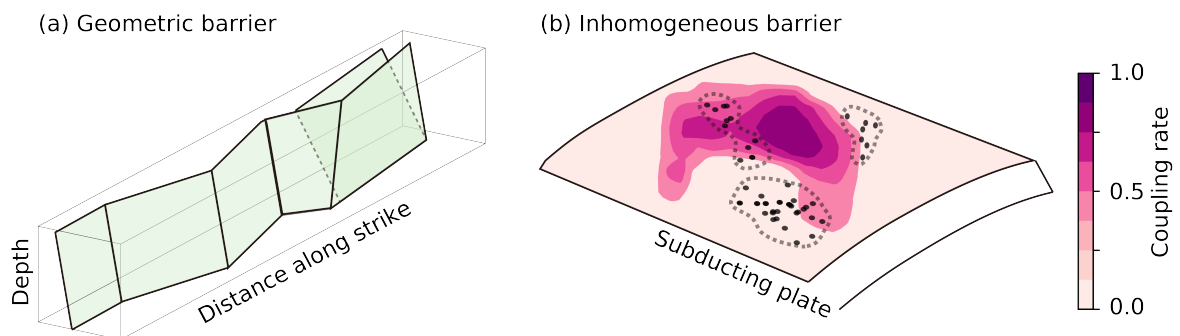
Figure 2.1 Schematic figure of the (a) geometric and (b) inhomogeneous barriers. (a) Colored rectangles represent the fault segments. (b) Color shows the interseismic coupling of the plate boundary. Dense pinkish areas and dots are the possible large slip areas and small patches of slip (earthquake swarms). Inhomogeneous barrier is denoted as the region outlined by dashed line.

2.1 | Geometric barrier

It is known that an earthquake fault has a geometric complexity and discontinuity in a wide scale range in nature referred to as *barrier* (Aki, 1979; King and Nábělek, 1985; Wesnousky, 2008), including steps and jogs that leads to the rupture irregularity when the rupture front encounters the spot where the material strength is greater than the regional-tectonic stress, and/or due to the dynamic-stress disturbance (Aki, 1979; Das and Aki, 1977; Kase and Day, 2006). Abrupt changes of slip velocity and/or rupture velocity are induced and the high-frequency waves are enhanced by such irregularities according to the theoretical studies of the earthquake rupture (Madariaga, 1977; Bernard and Madariaga, 1984; Spudich and Frazer, 1984; Madariaga *et al.*, 2006). Considering the resonant frequency of buildings, where and how the high-frequency waves are radiated are the center of concern for both the seismologists and engineers (Clinton, 2006; Snieder and Şafak, 2006; Kohler *et al.*, 2007). Particularly because many earthquakes in dense-populated inland areas involve geometric complexity in their fault systems (Sekiguchi, 2000; Wright *et al.*, 2001; Michel and Avouac, 2002; Xu *et al.*, 2009a), assessing the generation mechanism of high-frequency waves along these fault systems in detail may provide valuable information about rupture evolution that can be used to mitigate future-earthquake hazard.

In 1990s, envelope inversion has been developed for analysis of the the high-frequency waveforms (e.g., Gusev and Pavlov, 1991; Zeng *et al.*, 1993; Kakehi and Irikura, 1996). The envelope inversion utilizes to fit the observed and computed envelope of the high-frequency seismograms, instead of fully reproducing the complex phases of the high-frequency waveforms in the conventional waveform inversion. The detailed source process associated with the generation of high-frequency waves has been investigated by using the envelope inversion. For example during the 1995 Kobe, Japan, earthquake, Kakehi *et al.* (1996) found that the high-frequency wave sources were located around the step over of the fault system, which was interpreted as the step over acted as a geometric barrier and the high-frequency waves were emitted when the rupture from jumped across the barrier. The complementary distribution of the high-frequency sources and the inverted

slip distribution inferred by using the low-frequency waveforms has also found for the M_W 7.1 1989 Loma Prieta, California, earthquake Zeng *et al.* (1993) and the M_W 7.6 1993 Kushiro-oki, Japan, earthquake Kakehi and Irikura (1996). However, as reviewed in detail by Nakahara (2008), this complementarity is not always true, but sometimes the high-frequency sources and the large slip area collocated (e.g., the M_W 7.7 1993 Hokkaido Nansei-oki, Japan, earthquake (Kakehi and Irikura, 1997) and the M_S 7.1 1994 Northridge, California, earthquake (Hartzell *et al.*, 1996)), which may partly be resulted from the insufficient spatial resolution of the envelope inversion (e.g., Kakehi and Irikura, 1997).

Following the developments of the envelope inversion, Backprojection (BP) techniques were first applied to the great 2004 Sumatra-Andaman earthquake (Krüger and Ohrnberger, 2005; Ishii *et al.*, 2005), and have since made it possible to track sources of the high-frequency waves. Further developments of BP techniques have uncovered the hidden-rupture images of earthquake rupture that had previously been difficult to resolve by the kinematic waveform inversion alone, for example, multiple branching ruptures and the triggering of asperity ruptures (e.g., Meng *et al.*, 2012b; Fan *et al.*, 2016; Allmann and Shearer, 2007). Enhancement of the spatial resolution of the projected image by adopting the globally observed stations, not limited to the arrays, with good azimuthal coverage (Walker *et al.*, 2005; Allmann and Shearer, 2007; Yagi *et al.*, 2012a; Okuwaki *et al.*, 2014; Fan and Shearer, 2015) is another advance for the observation of high-frequency radiation. It has become available for discussion of the relationship between the high-frequency-enhanced rupture evolution and the geometric complexity of the fault system by the integrated analysis of the BP method and the waveform inversion (e.g., Uchide *et al.*, 2013). However due to the limited resolution in depth of the BP method (e.g., Xu *et al.*, 2009b), it has been difficult to image sources of high-frequency waves that are possibly extending to deeper part of fault. Besides, the spatiotemporal variation of focal mechanism, related to the geometric feature of the fault system, is not explicitly taken into account by the BP method, and may not be well enough resolved so that we could discuss the role of geometric barrier on the rupture evolution. The Hybrid BP

(HBP) method (Yagi *et al.*, 2012a; Okuwaki *et al.*, 2014); a variant of the BP methods, ensures better resolution at depth by using the differences of travel times and phase amplitudes between the P-phase and depth phases (pP and sP), extracted by cross correlation of observed waveforms with the theoretically computed Green's functions. An explicit use of the Green's functions enables us to assume fault geometry, and the HBP method can then be used to assess how fault geometry is related to the emission of high-frequency waves, and to irregular rupture propagation.

2.1.1 The 2008 Wenchuan, China, earthquake

The M_W 7.9 2008 Wenchuan, China, earthquake is knows as the earthquake involves the distinguished surface ruptures revealed by the analyses of the Global Positioning System (GPS) and interferometric synthetic aperture radar (InSAR) data, suggesting that co-seismic rupture propagated along a multi-segment fault system characterized by steps and sub-parallel faults (Xu *et al.*, 2009a; Hashimoto *et al.*, 2010; Fielding *et al.*, 2013; Wan *et al.*, 2017) (Fig. 2.2). Thus, the 2008 Wenchuan earthquake should be one of the notable research subjects for investigating the relationship between geometric complexity in a fault system and irregular rupture propagation by analysis of high-frequency waveforms. The mapped-surface ruptures of the 2008 Wenchuan earthquake generally trend northeast along the Longmen Shan thrust belt, which lies along the eastern margin of the Tibetan Plateau in an area where the elevation of the land rises steeply westward from 500 m to more than 4000 m above the Sichuan basin (Burchfiel *et al.*, 2008). Focal mechanisms of relocated aftershocks and seismic reflection data have shown that the fault dipping steepens from southwest to northeast of the epicenter (Yu *et al.*, 2010; Hubbard and Shaw, 2009; Hubbard *et al.*, 2010). A notable feature of the fault system is that both the southern Beichuan fault (SBF) segment and the sub-parallel Pengguan segment are cut by the Xiaoyudong fault (XDF), a small, vertical tear fault that strikes roughly perpendicular to the Beichuan and Pengguan fault segments (Liu-Zeng *et al.*, 2012) and works as a kink for both of them (Fig. 2.2). The XDF has attracted the attention of seismologists because of its possible role in irregular rupture
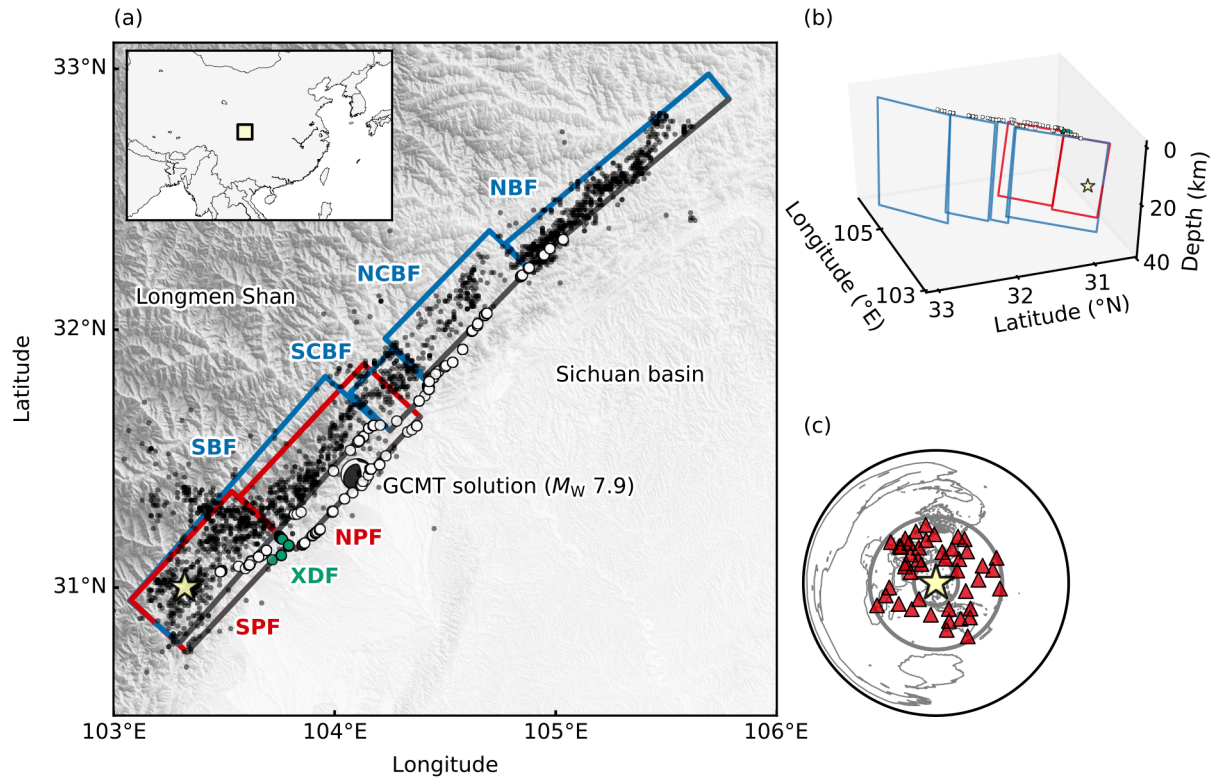
Figure 2.2 Summary plots of the study area, model setting, and data used in this chapter (a) Star denotes the epicenter. Black dots are the relocated aftershocks (Yu *et al.*, 2010). Beach ball represents the Global Centroid Moment Tensor solution (http://www.globalcmt.org, last accessed on August 12, 2017). White and green circles are the locations of surface ruptures along the Beichuan-Pengguan segments and the XDF, respectively, (Xu *et al.*, 2009a). Blue and red rectangles are the presumed fault segments used as the model-fault planes in this study (SBF, south Beichuan fault; SCBF, south-central Beichuan fault; NCBF, north-central Beichuan fault; NBF, north Beichuan fault; SPF, south Pengguan fault; and NPF, north Pengguan fault). Gray lines represent the shallowest edge of each fault segment. The 2010 Global Multi-resolution Terrain Elevation Data 7.5-arcsecond spaced mean elevations (Danielson and Gesch, 2011) is used for the background topography. Inset shows the study area of (a). (b) Three-dimensional view of the model-fault segments. The Beichuan and the Pengguan segments are represented by blue and red lines. Star denotes the hypocenter. White and green circles show the measurement points where the surface rupture was observed along the Beichuan-Pengguan segments and the XDF segment (Xu *et al.*, 2009a). (c) Station distribution (triangles). The star marks the epicenter, and the gray circles denote the epicentral distances of 30° and 90°.

propagation along the fault system (e.g., Hartzell *et al.*, 2013).

The co-seismic slip patterns of the 2008 Wenchuan earthquake have been proposed in numerous seismic source models constructed by solely or jointly inverting the seismic waveforms observed at teleseismic or near-field distances, the GPS data, and the InSAR data (Shen *et al.*, 2009; Yagi *et al.*, 2012b; Fielding *et al.*, 2013; Hartzell *et al.*, 2013), and the common knowledge drawn from these studies are the almost unilateral rupture propagation towards northeast involving several sub-patches of large slip and the variable slip motions generally rotating from reverse to right-lateral faulting as rupture front propagates northeast from the epicenter. The BP studies using the high-frequency ($\sim$1 Hz) teleseismic P waveforms (Xu *et al.*, 2009b; Zhang and Ge, 2010) have also shown that the rupture propagated almost unilaterally toward northeast with the average speed of 2.8 to 3.0 km/s, which is consistent with the inverted slip models using the low-frequency waveforms, and pointed out that there are several bursts of high-frequency wave radiation that coincide with the areas suffering severe damages (Xu *et al.*, 2009b). However, because the BP images are only projected at the surface and have insufficient resolution along the dip directions, evaluations of high-frequency wave radiations in a context of the complex fault geometry have yet been done.

Here we estimate a spatiotemporal distribution of high-frequency wave radiators by using the globally observed teleseismic P waveforms of the 2008 Wenchuan earthquake, and discuss a role of geometric barriers along the fault system that controls the irregular rupture evolution.

2.1.2 Model faults for the 2008 Wenchuan earthquake

We covered a possible source region of the Beichuan fault and its sub-parallel, Pengguan fault with seven rectangular fault segments composed of discretized source nodes with spatial intervals of 2 km $\times$ 2 km along the strike and dip directions to ensure the sufficient-spatial resolution of the HBP method (Fig. 2.2 and Table 2.1). Each fault segment is arranged to trace the surface ruptures mapped by the filed surveys (Xu *et al.*, 2009a) and the geodetic measurements of the SAR pixel offsets (Field-

Table 2.1 Geometric parameters of fault segments for the 2008 Wenchuan earthquake.

Segment	Strike (°)	Dip (°)	Length (km)	Width (km)
SBF	221	45	130	42
SCBF	224	54	28	42
NCBF	224	54	66	42
NBF	230	70	114	42
SPF	223	34	66	42
NPF	223	34	80	42

ing *et al.*, 2013). The selection of the dip angle and the depth-extent for each fault segment is guided by the focal mechanisms of the relocated aftershocks (Yu *et al.*, 2010) and the three-dimensional fault model constructed by using the seismic reflection and the surface geological data (Hubbard and Shaw, 2009; Hubbard *et al.*, 2010). Non-uniqueness of the assumption of the fault model is considered by using the single monoplane fault model (Fig. 2.3), and we confirmed that the arbitrariness of the geometrical-model setting does not affect the whole discussion presented in chapter 4. We did not include the XDF into the fault model since its length (∼7 km) (Liu-Zeng *et al.*, 2012) is close to the spatial resolution of the HBP method for the high-frequency waveforms (Fig. 2.4). We adopted the epicenter (31.002°N, 103.32°E) determined by the U.S. Geological Survey, National Earthquake Information Center (`https://earthquake.usgs.gov/earthquakes/eventpage/usp000g650`). Hypocentral depth was assumed to be on 15 km depth as the initial rupture point where the SBF and the south Pengguan fault (SPF) intersect at that depth in our fault model.
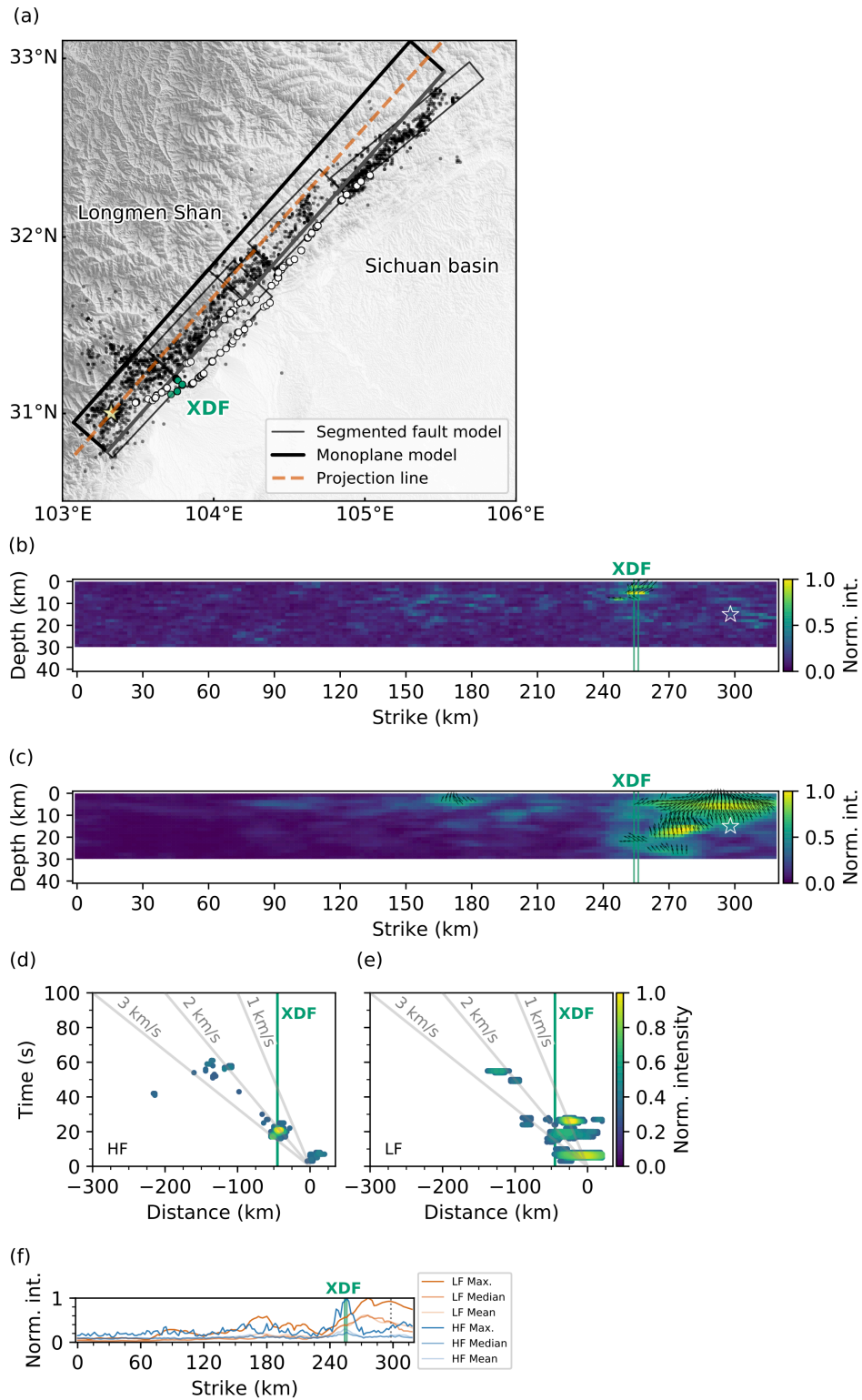
Figure 2.3 Caption next page.

Figure 2.3 Alternative results by using monoplane-model fault. (a) Map showing the epicenter (star), the relocated aftershocks (black dots) (Yu *et al.*, 2010), locations of surface ruptures along the Beichuan-Pengguan segments (white circles) and the XDF (green circles) (Xu *et al.*, 2009a), the monoplane model fault (thick black rectangle) used for the validation of the main analyses (Fig. 2.5) and the synthetic tests of the HBP method (Fig. 2.4), and the segmented model fault (thin black rectangles; Fig. 2.2). The monoplane model fault was constructed based on the fault geometry of the SBF (Table 1) with the length of 320 km and the width of 42 km. Gray lines represent the shallowest edge of each fault segment. Orange line is the projection line drawn from the epicenter along the strike (221°) direction, used for generating Figs. 3, S1d, S1e, S2c, and S2d. Background topography is derived from 2010 Global Multi-resolution Terrain Elevation Data 7.5-arcsecond spaced mean elevations (Danielson and Gesch, 2011). (b) Spatial distribution of high-frequency sources in a strike vs. depth view. Background colors represent normalized signal intensities. Arrows show rake angles, which for clarity are shown only on source cells for which signal intensities are greater than 0.5. Green lines indicate the estimated location of the XDF and the star marks the hypocenter. (c) Same as Fig. 2.3b, but for the low-frequency result. (d) Colored circles indicate the spatiotemporal distribution of locations of high-frequency (HF) signals along the monoplane model fault. Color scheme is the same as in Fig. 2.5. For clarity, only sources of normalized intensity greater than 0.3 are shown. The abscissae are distances from the epicenter along the strike (221°) direction, and the ordinate is an elapsed time from the hypocentral time. The estimated locations of the XDF (green line) and reference rupture speeds (gray lines) are also shown. (e) Same as Fig. 2.3d, but for the low-frequency (LF) result. (f) Distributions of maximum, median, and mean values of signal intensity along the dip direction of the monoplane model fault. The abscissae give distances along strike from the left-bottom corner of the model fault, and the ordinate is a normalized signal intensity. Cold and warm colors represent the high- and low-frequency (HF and LF) results, respectively. The estimated locations of the XDF (green lines) and the location of the hypocenter (gray dotted line) are also shown.

(a)

(b)

(c) HF

(d) LF
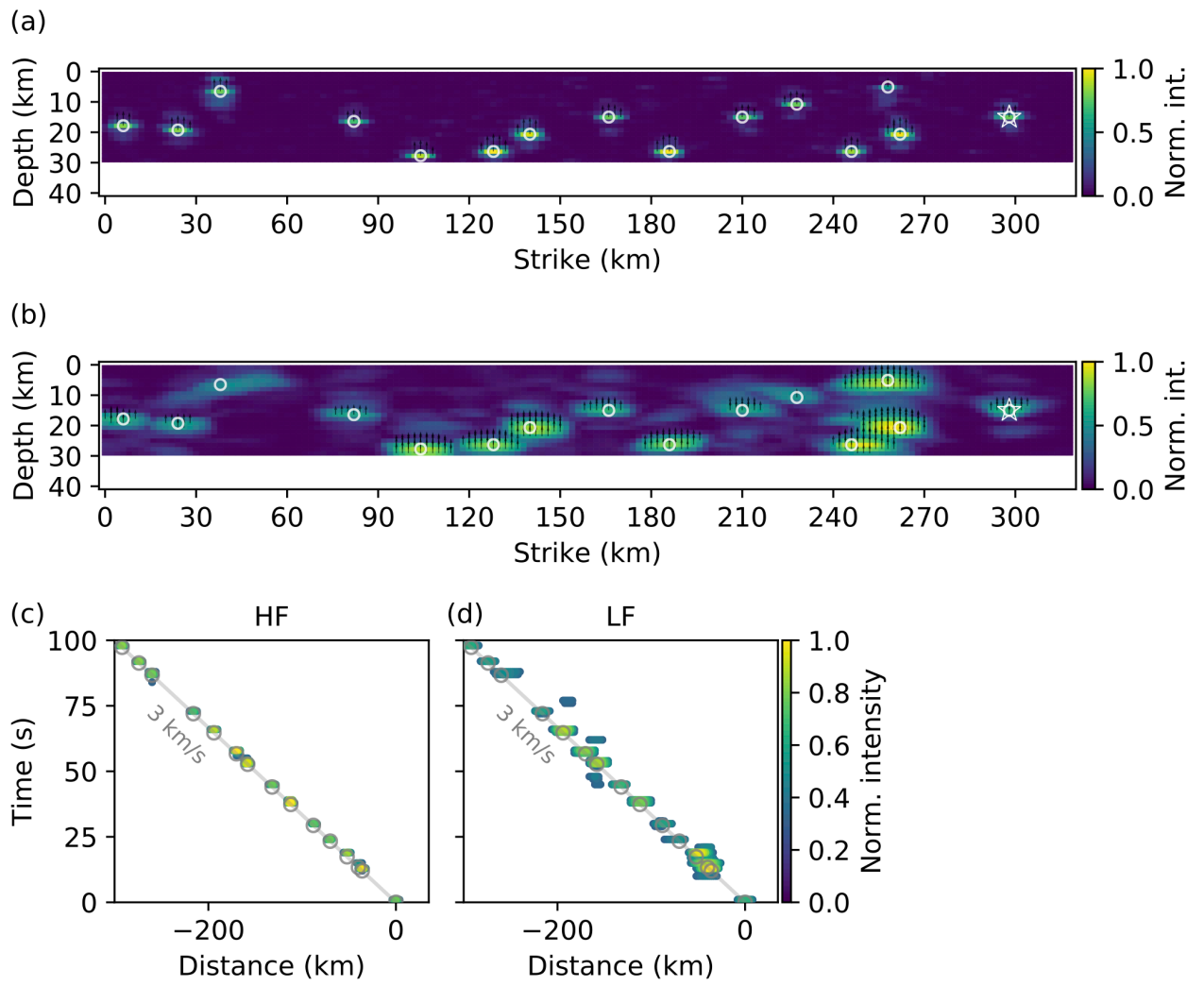
Figure 2.4 Caption next page.

Figure 2.4 Synthetic test of the HBP method. (a) Spatial distribution of high-frequency sources in a strike vs. depth view. Background colors represent normalized signal intensities. Arrows show rake angles, which for clarity are shown only on source cells for which signal intensities are greater than 0.5. The star marks the hypocenter. We generated synthetic waveforms with multiple point sources depicted as white circles located along the monoplane model fault presented in Fig. 2.3. Each point source has the uniform potency generated with the rise time of 0.25 s of the triangle slip-rate function, and we assumed that each rise of the slip-rate function was triggered by the constant-propagating rupture front at 3 km/s. The Green's functions for generating the synthetic waveforms were calculated as the same procedure for the HBP analysis adopted in this study. (b) Same as Fig. 2.4a, but for the low-frequency result. (c) Colored circles indicate the spatiotemporal distribution of locations of high-frequency (HF) signals along the monoplane model fault. Color scheme is the same as in Fig. 2.5. For clarity, only sources of normalized intensity greater than 0.3 are shown. The abscissae are distances from the epicenter along the strike (221°) direction, and the ordinate is an elapsed time from initial rupture time. The locations of synthetic point sources (gray circles) and the reference rupture speed at 3 km/s (gray line) are also shown. (d) Same as Fig. 2.4c, but for the low-frequency (LF) result.

2.1.3 Data processing for estimating the high- and low-frequency sources

We used 44 vertical-component P-waveforms of the 2008 Wenchuan earthquake, recorded at the Global Seismograph Network (GSN) stations at teleseismic distances (between $30°$ and $90°$), downloaded through the Incorporated Research Institutions for Seismology Data Management Center (IRIS DMC; Fig. 2.2c). We selected the data to ensure good azimuthal coverage and sufficient signal to noise ratio. We manually picked the first arrival of the P-phase on each waveform, and deconvolved the instrumental response to velocity at a sampling rate of 0.05 s.

The spatiotemporal distribution of high- and low-frequency radiation sources were obtained by solving the following equations:

$$c_{ij}(t, \phi_k, \delta_k, \lambda_k) = \frac{u_j(t) \hat{\times} G_{ij}(t, \phi_k, \delta_k, \lambda_k)}{\sqrt{\int u_j^2(t)dt} \cdot \sqrt{\int G_{ij}^2(t, \phi_k, \delta_k, \lambda_k)dt}}, \tag{2.1}$$

$$r_i(t, \phi_k, \delta_k, \lambda_k) = \sum_j a_j |c_{ij}|^{\frac{1}{N}} \cdot \frac{c_{ij}}{|c_{ij}|}(t, \phi_k, \delta_k, \lambda_k), \tag{2.2}$$

$$s_i(t) = \max_k |r_i|^N \cdot \frac{r_i}{|r_i|}(t, \phi_k, \delta_k, \lambda_k). \tag{2.3}$$

First, we calculated the normalized cross correlation function c_{ij} of the observed waveform u_j at jth station and the corresponding Green's function G_{ij} for each pair of jth station and ith source node (eq. 2.1). r_i is then calculated by stacking N-th root of the c_{ij} for all the stations by preserving each sign of c_{ij}, where a_j is a controlling factor to prevent possible bias due to the station distribution (eq. 2.2). In this study, we introduced components of focal mechanism k (strike ϕ_k, dip δ_k, and rake λ_k, defined by Aki and Richards (2002)) on each source node for calculating Green's functions, and we finally obtained the signal intensity s_i at each source node that maximizes N-th power of r_i among the components of focal mechanism (eq. 2.3). Note that strike and dip angles were fixed for each fault segment (Table 2.1), and the range of rake angle, between $0°$ and $180°$ with an increment of $5°$, was constrained by geological surveys of

Table 2.2 Near-source structure used to calculate Green's functions for the 2008 Wenchuan earthquake.

V_P (km/s)	V_S (km/s)	Density (10^3kg/cm^3)	Thickness (km)
4.50	2.51	2.45	4.50
5.00	2.88	2.54	2.00
6.10	3.53	2.74	11.35
6.50	3.71	2.83	12.76
6.90	3.93	2.92	21.35
8.02	4.46	3.31	0.00

the surface ruptures, which show that the reverse faulting is dominant in the vertical off-sets (Xu *et al.*, 2009a; Yu *et al.*, 2010). Eqs. (2.2) and (2.3) represent the N-th root stacking ($N = 4$) (Muirhead and Datt, 1976) to enhance the signal to noise ratio of the c_{ij}. Green's functions were computed based on the method of Kikuchi and Kanamori (1991). The travel times, the geometrical spreading factors, and the ray parameters were calculated with the ak135 model (Kennett *et al.*, 1995), and the CRUST1.0 model (Laske *et al.*, 2013) was used to construct the near-source structure (Table 2.2) for calculation of the Haskell propagator matrix in the Green's function. High-frequency (0.5 to 2.0 Hz) and low-frequency (0.1 to 0.5 Hz) Butterworth bandpass filters were applied to both the observed waveforms and the Green's functions before cross correlation for the high- and low-frequency analyses, respectively.

2.1.4 High-frequency sources

Our analysis showed that sources of high-frequency (0.5 to 2.0 Hz) waves with strong signal intensity were concentrated near geometric discontinuities of the fault system where the XDF cuts the middle part of the SBF ($\sim$70 km along strike), and where it crosses near the boundary between the SPF and the north Pengguan fault (NPF) segments at 5 to 10 km depth at 15 to 25 s from the hypocentral time (Figs. 2.5a, 2.6a and 2.7a). Other sources of high-frequency waves of modest intensity were observed at the northeastern edge of the NPF and at the boundaries between the SBF and the
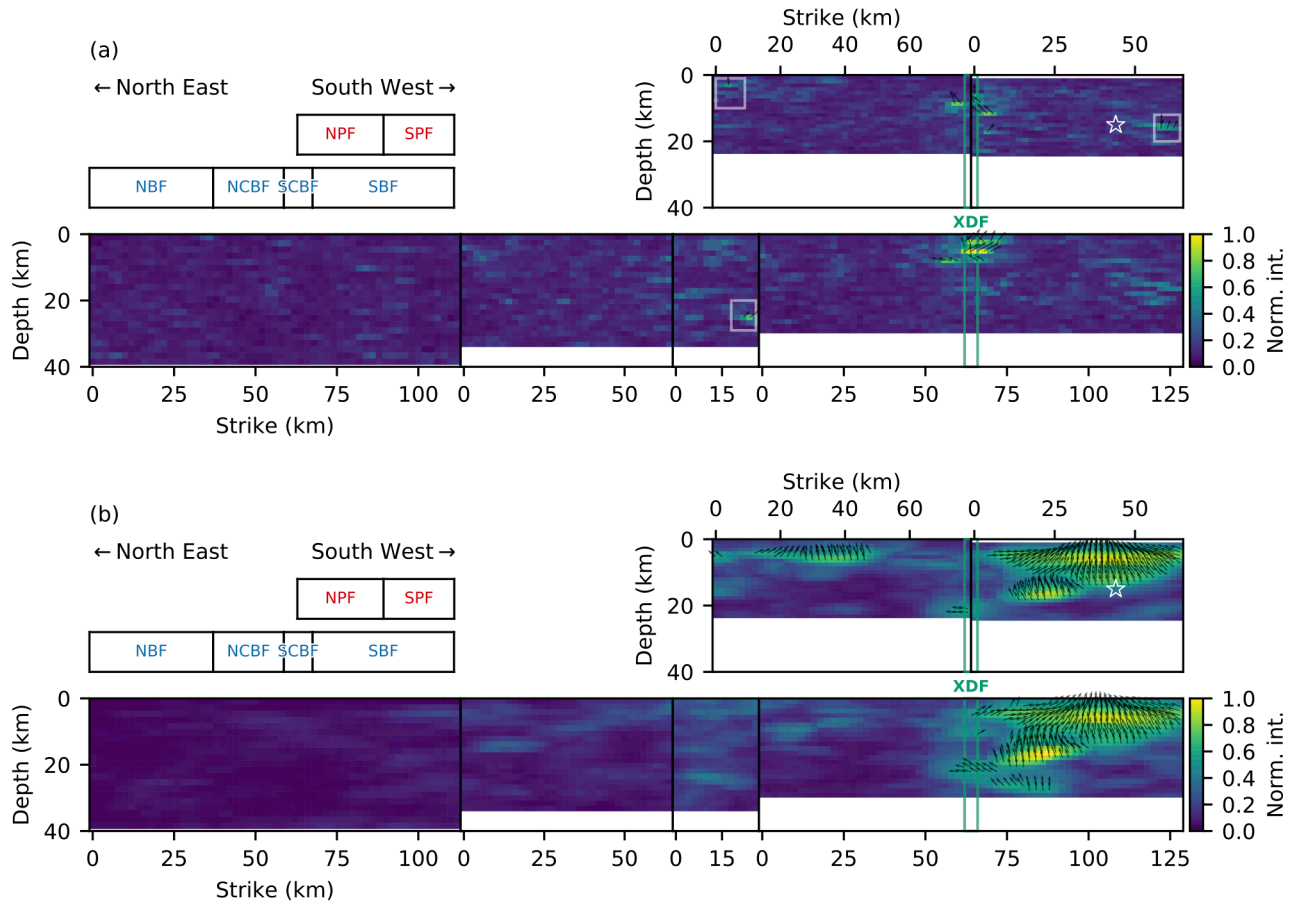
Figure 2.5 (a) Cross section of the high-frequency sources in a strike-depth view. Star denotes the hypocenter. Estimated location of the XDF is shown as green lines. Background colors represent normalized signal intensities. Arrows show rake angles, which for clarity are shown only on source cells for which signal intensities are greater than 0.5. White rectangles represent the locations of modest intensity of high-frequency sources. (b) Same as Fig. 2.5a, but for the low-frequency result. Configuration of the fault segments is summarized at top-left corner on each panel. See caption of Fig. 2.2a for fault segment names.
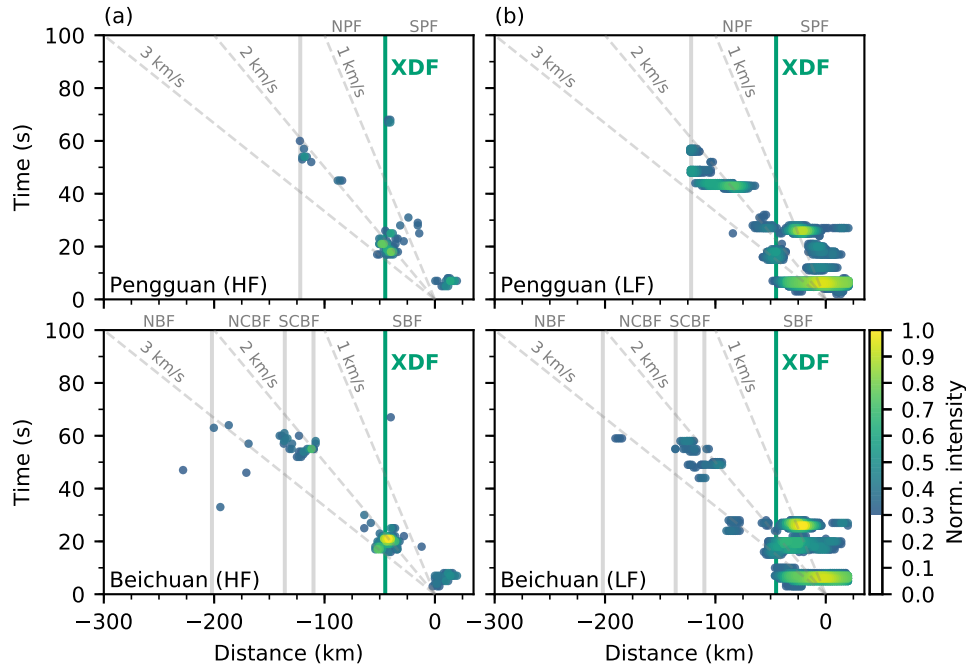
Figure 2.6 Spatiotemporal distribution of sources of high- and low-frequency waves. (a) Colored circles indicate the spatiotemporal distribution of locations of high-frequency (HF). Color scheme is the same as in Fig. 2.5. For clarity, only sources of normalized intensity greater than 0.3 are shown. The abscissae are distances from the epicenter along the strike (221°) direction, and the ordinate is an elapsed time from the hypocentral time. The estimated locations of the XDF (green line) and reference rupture speeds (gray dashed lines) are also shown. Gray solid lines represent the segment boundaries. (b) Same as Fig. 2.6a, but for the low-frequency (LF) result.
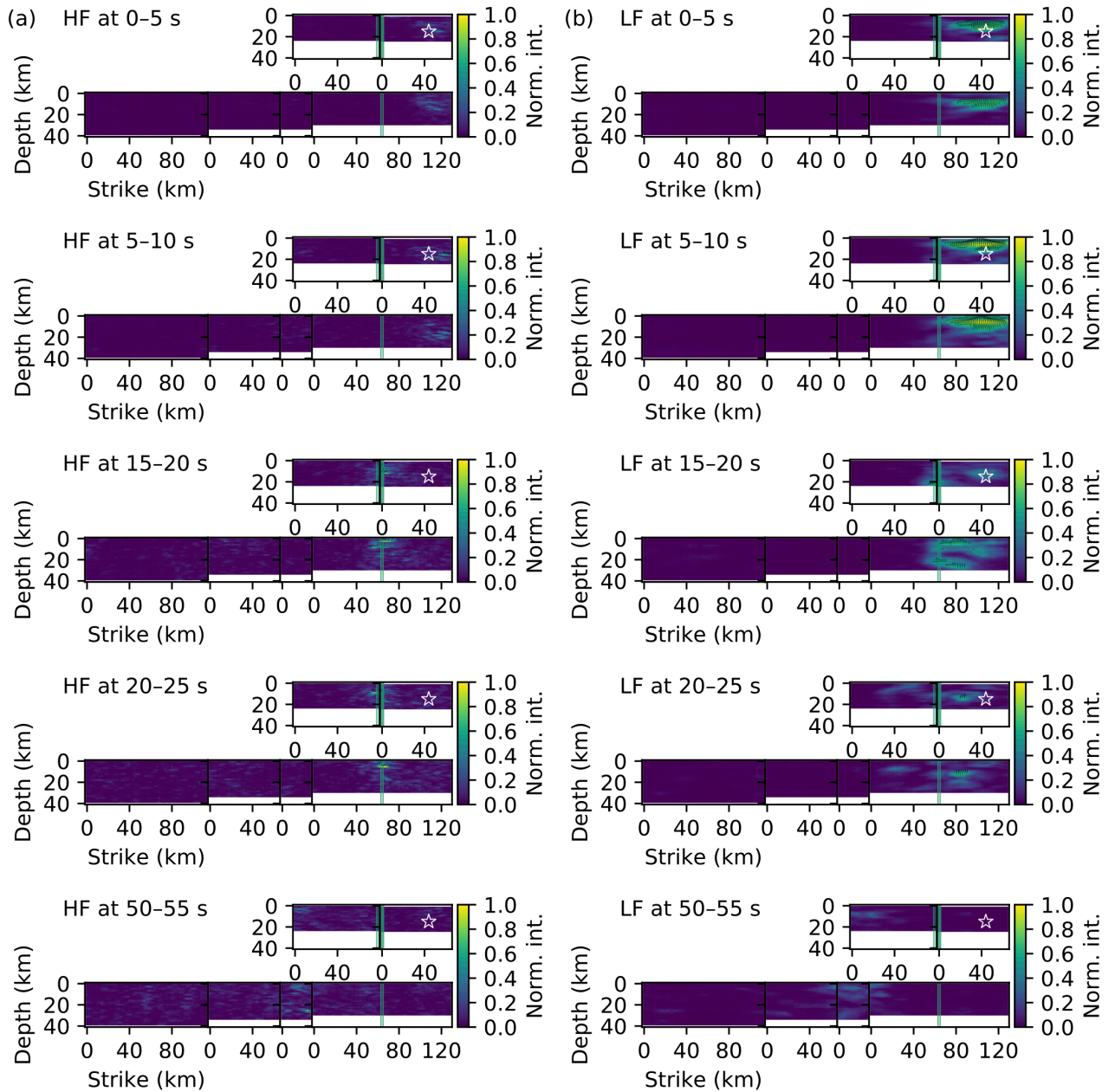
Figure 2.7 Selected snapshots of Fig. 2.5. (a) Selected snapshots of the high-frequency (HF) result shown in Fig. 2.5a taken at interval of 5 s. Background color represents the normalized signal intensity. Time range from the hypocentral time where the snapshot is taken is denoted at left-top of each panel. Layout of fault segments is the same as Fig. 2.5a. Arrows show rake angles, which for clarity are shown only on source cells for which signal intensities are greater than 0.5. Green lines indicate the estimated location of the XDF and the star marks the hypocenter. (b) Same as Fig. 2.7a, but for the low-frequency (LF) result.

south-central Beichuan fault (SCBF) segments, and between the SCBF and the north-central Beichuan fault (NCBF) at 50 to 60 s from the hypocentral time (Figs. 2.5a and 2.6a). The estimated rupture velocity was 2 to 3 km/s along the strike direction of the SBF (221°) from the epicenter (Fig. 2.6a), assuming that the high-frequency P waves were radiated from the rupture front. Rupture front generally propagated toward northeast from the epicenter, but for the first ∼10 s from the earthquake origin time, high-frequency sources with modest intensity appeared southwest of the epicenter along both the SBF and the SPF (Fig. 2.6a), suggesting that the source process involved the bilateral propagation soon after the initiation of rupture. The southwestward rupture was also observed on the SPF, after the strong bursts of high-frequency waves near its intersection with the XDF. Notably, the rake angles for the sources with intense high-frequency radiations showed scattered distribution (Fig. 2.5a), making it difficult to retrieve a typical direction of slip motion, unlike in the low-frequency result that we will see in the following section.

2.1.5 Low-frequency sources

We estimated the locations of sources of low-frequency (0.1 to 0.5 Hz) waves as we did for the high-frequency waveforms (Figs. 2.5b, 2.6b and Fig. 2.7b). Intense low-frequency radiations were observed in the middle of the SBF and the SPF, showing the complementary locations with those for the high-frequency locations, which located near the geometric discontinuities of the fault, as we presented in the previous section. The distributions of low-frequency sources on the sub-parallel SBF and SPF are similar, as are those of the SCBF and the northeastern edge of the NPF (Fig. 2.5b), because the spatial resolution of the low-frequency sources is inferior to that of the high-frequency sources (Fig. 2.4), and the spatial resolution is within the spatial distance between the fault segments for the low-frequency sources resolved by the HBP method. The sources of low-frequency waves propagated mainly northeastward until ∼20 s after the hypocentral time, but thereafter they migrated bilaterally southwestward and northeastward from the XDF (Fig. 2.6b). The southwestward propagation quickly ceased ∼30 s after the

hypocentral time, whereas the northeastward propagation continued until ∼50 s from the hypocentral time (Fig. 2.6b). Note that estimation of rupture velocity from the low-frequency data is difficult because of the spatial resolution. The rake angles for the intense low-frequency sources showed smoother distribution that those for the high-frequency sources (Fig. 2.5b). Reverse faulting is dominant for the southwestern part of the SBF and the middle part of the SPF, whereas right-lateral faulting is evident near the XDF.

2.2 | Inhomogeneous barrier

Inhomogeneous barrier; another end-member of barrier (e.g., Aki, 1979), is a spatial heterogeneity of strength of the fault, which is known to control the earthquake-rupture evolution. The inhomogeneous barrier is classified as the barrier without the obvious geometric discontinuity. Aki (1979) introduced to the inhomogeneous barrier as the stopping point of earthquake rupture, associated with the anomaly of the seismic velocity, existence of volcanos, and the seamount subduction (e.g., Kelleher and McCann, 1976). Recently, Holtkamp and Brudzinski (2014) reported that the rupture area of the subduction zone megathrust earthquake is often surrounded by the region where the active earthquake swarm occurs, which is a intense seismicity where the decay of seismicity rate does not follow the Omori's law (e.g., Llenos *et al.*, 2009), and the earthquake swarm may be a proxy for the inhomogeneous barrier against the earthquake rupture. In this section, we investigated the possible role of the inhomogeneous barrier on the dynamic earthquake rupture evolution through the analysis of the source process of the M_W 8.3 2015 Illapel, Chile, earthquake, where the intense earthquake swarm has been observed in and around the rupture area (e.g., Lemoine *et al.*, 2001; Nishikawa and Ide, 2017), by using the hybrid backprojection and the waveform inversion.

2.2.1 The 2015 Illapel, Chile, earthquake

The M_W 8.3 2015 Illapel, Chile, earthquake occurred at north central Chile, and the coast near the source region experienced the severe shaking (the maximum Mercalli intensity scale of VIII was observed in the Coquimbo region) and tsunami (Aránguiz *et al.*, 2016). The focal mechanism for this earthquake, determined by the Global Centroid Moment Tensor project (GCMT: http://www.globalcmt.org/CMTsearch.html) shows a low-angle thrust faulting (Fig. 2.8), indicating that the 2015 Illapel earthquake was an interplate earthquake where the Nazca plate is subducting beneath the South America plate at a rate of about 74 mm/y (DeMets *et al.*, 2010, Fig. 2.8). Following the mainshock, a tsunami struck the coast with a significant impact near the source region,
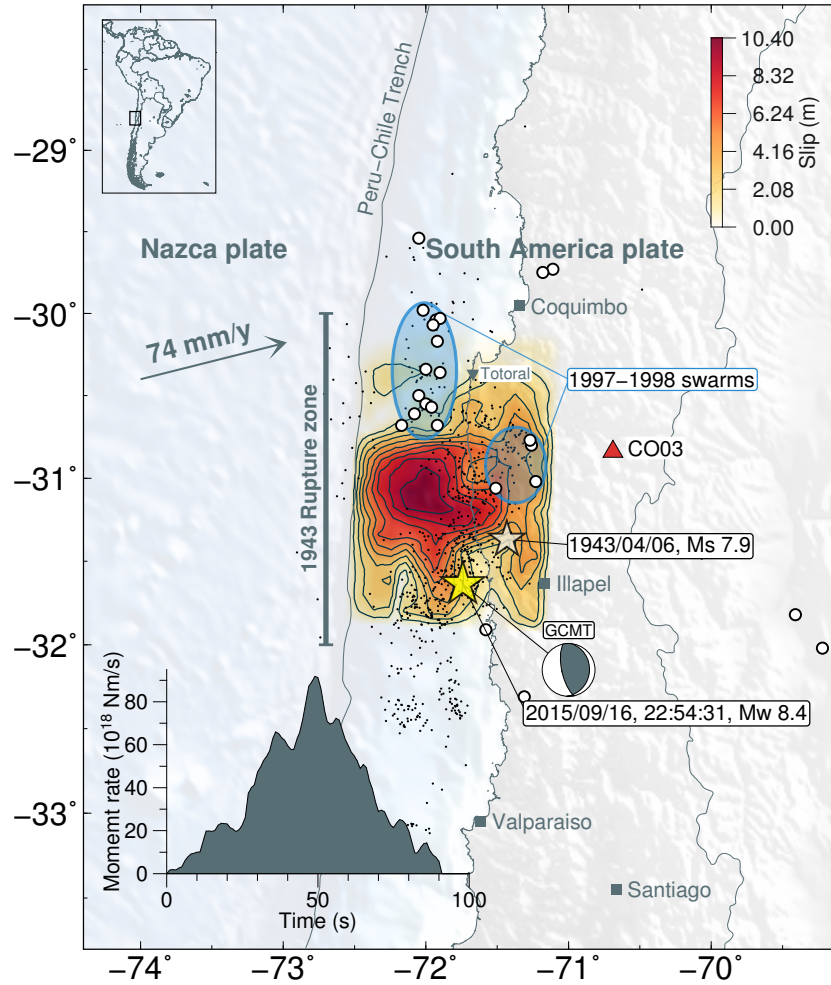
Figure 2.8 The epicenters of the 2015 Illapel earthquake (CSN) and the 1943 Illapel earthquake (Centennial Catalog; Engdahl, 2002) are denoted as yellow and white stars, respectively. Epicenters of 1-week-aftershock (M ≥ 3 and shallower than 50 km depth, CSN) are drawn as black dots. Inset is a moment-rate function obtained by the finite-fault inversion. Beach ball is the focal mechanism determined by the GCMT project. The estimated rupture length of the 1943 Illapel earthquake is shown as the vertical bar (Beck *et al.*, 1998). The relative motion of the Nazca plate to the fixed South America plate, employing the MORVEL model (DeMets *et al.*, 2010) is represented by arrows. The relocated epicenters of the 1997-1998 swarms (5.5 ≤ mb ≤ 6.2; Pardo *et al.*, 2002) are shown as open black circles. The estimated area where the 1997-1998 earthquake swarm (Lemoine *et al.*, 2001) is denoted as blue-rimmed areas. The station C003, which is used for the analysis of the strong motion records in section 4.2.4, is shown as red triangle. The slip contour is every 1.04 m. Background topography and bathymetry are from ETOPO1 (Amante and Eakins, 2009).

and the maximum run-up was observed at Totoral village (Fig. 2.8), where it reached 10.8 m (Aránguiz *et al.*, 2016).

The source region of the 2015 Illapel earthquake belongs to the seismically active Coquimbo-Illapel region (30° to 32°S). The greatest historical Chilean earthquake covering this area was the 1730 earthquake whose magnitude is estimated to be M_S 8.5 to 9 (Lomnitz, 2004), and its rupture area is estimated to be extended from Coquimbo (30°S) down to the northern part (35°S) of the rupture zone of the 2010 Maule, Chile, earthquake (e.g., Udías *et al.*, 2012). The last significant earthquake in this region, but much smaller than the 1730 earthquake, was the M_S 7.9 1943 Illapel earthquake (Centennial Catalog; Engdahl, 2002), and its source region overlaps the rupture area of the 2015 Illapel earthquake (Beck *et al.*, 1998, Fig. 2.8). Estimated source region of the 1943 Illapel earthquake overlaps the rupture area of the 2015 Illapel earthquake (Fig. 1). After the occurrence of the 1943 Illapel earthquake, the seismic gap along the Coquimbo-Illapel region was partially reactivated during 1997–1998 by M6 swarm events (1997–1998 earthquake sequence; Lemoine *et al.*, 2001; Pardo *et al.*, 2002) (Fig. 2.8). Seismicity rate in the northern part (29.5° to 31°S) of Coquimbo-Illapel region suddenly increased on July 1997 when some M6 shallow-thrust events occurred along the plate interface, and the M_W 7.1 1997 Punitaqui earthquake (15 October 1997) followed these earthquake sequence (Lemoine *et al.*, 2001). The 1997 Punitaqui earthquake was inside the Nazca plate below the down-dip edge of the seismogenic zone and characterized by a normal faulting moment tensor (Lemoine *et al.*, 2001; Pardo *et al.*, 2002). Several M6 inter-plate earthquakes followed the 1997 Punitaqui earthquake by the end of 1998, and the seismicity rate remains higher than that before the 1997–1998 earthquake sequence (Gardi *et al.*, 2006). Gardi *et al.* (2006) found that the 1997–1998 swarms can be explained as a result of the stress transfer from the aseismic slip (65 mm/y) below the down-dip edge of the seismogenic zone. Moreno *et al.* (2010) derived the plate-interface locking degree before the M_W 8.8 2010 Maule Chile earthquake during 1996–2008 by using the global positioning system (GPS) observations, and pointed out that the middle part of the Coquimbo-Illapel region (31°S) is highly locked (almost

100% coupled) and has a potential of occurrence of future earthquake. Métois *et al.* (2013) also used the GPS data to invert a degree of interplate coupling and showed a heterogeneous distribution of locking degree along the plate interface: almost 100% coupled at 15 to 25 km depth from center to south of the Coquimbo-Illapel area, and relatively low coupling in the north of the Coquimbo-Illapel area which corresponds to the north region where the active swarm activity had been observed in 1997 to 1998. Based on the plate-coupling degree inferred from the GPS measurements and the swarm activity along the Coquimbo-Illapel region, the 2015 Illapel earthquake occurred where the stress build-up has been conducted non-uniformly in both space and time after the occurrence of the 1943 Illapel earthquake.

In this section, we aim to investigate a detailed rupture history of the 2015 Illapel earthquake. We modeled a seismic source model by estimating the spatiotemporal distribution of inverted slip and high-frequency (0.3 to 2.0 Hz) radiation sources. We used the finite-fault slip inversion method taking into account the uncertainty of the Green's function (Yagi and Fukahata, 2011a) and the HBP method (Yagi *et al.*, 2012a; Okuwaki *et al.*, 2014) to track the high-frequency sources. The integrated use of the inversion and the HBP method by using a wide range of frequency contents of the teleseismic records is essential for resolving the detailed rupture history, because the high-frequency waves (around 1 Hz) are generated by abrupt changes in rupture velocity and/or slip-rate (e.g., Madariaga, 1977; Bernard and Madariaga, 1984; Spudich and Frazer, 1984), and the high-frequency signal can be an index of the rapid change of rupture behavior that is difficult to be resolved solely with low-frequency waveforms (Okuwaki *et al.*, 2014; Yagi and Okuwaki, 2015). By comparing the inverted slip and high-frequency source distributions, we present a complex, seismic source model involving two rupture episodes characterized by along-dip, zigzagging rupture propagation at variable rupture speeds.
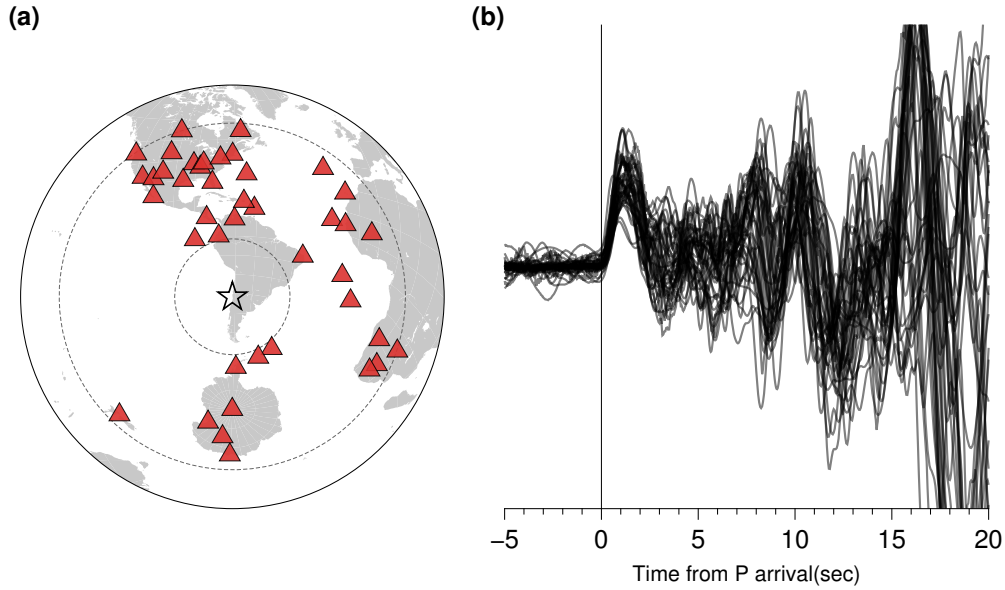
Figure 2.9 (a) Teleseismic stations used for both the waveform inversion and the HBP analyses. The epicenter and the stations are denoted as star and triangles. Reference teleseismic distances at 30° and 90° are represented as dashed lines. (b) Unfiltered traces of the teleseismic records used in both the finite-fault inversion and the HBP, normalized by the maximum amplitude of each trace. The X axis is the time from the first arrival of P-phase.

2.2.2 Data processing for estimating the high-frequency sources and the co-seismic slip distribution

We downloaded 42 teleseismic, vertical component of P-waveforms through the Incorporated Research Institutions for Seismology - Data Management Center (IRIS-DMC; Fig. 2.9a). The data were selected to ensure good azimuthal coverage and high signal-to-noise ratios. The first rise of the P-phase on each seismogram was manually picked (Fig. 2.9b), and we excluded the data whose P-phase is difficult to be reliably picked (Fig. 2.10). The instrument response of each waveform was deconvolved to velocity with the sampling rates of 0.05 s for the HBP analysis and 1.0 s for the inversion analysis. The data were then filtered into frequency bands of 0.3 to 2.0 Hz for the HBP analysis and 0.001 to 0.36 Hz for the inversion analysis.

Spatiotemporal distribution of high-frequency sources is estimated by the HBP method (Yagi *et al.*, 2012a; Okuwaki *et al.*, 2014) (a sensitivity test is shown in Fig. 2.11). High-
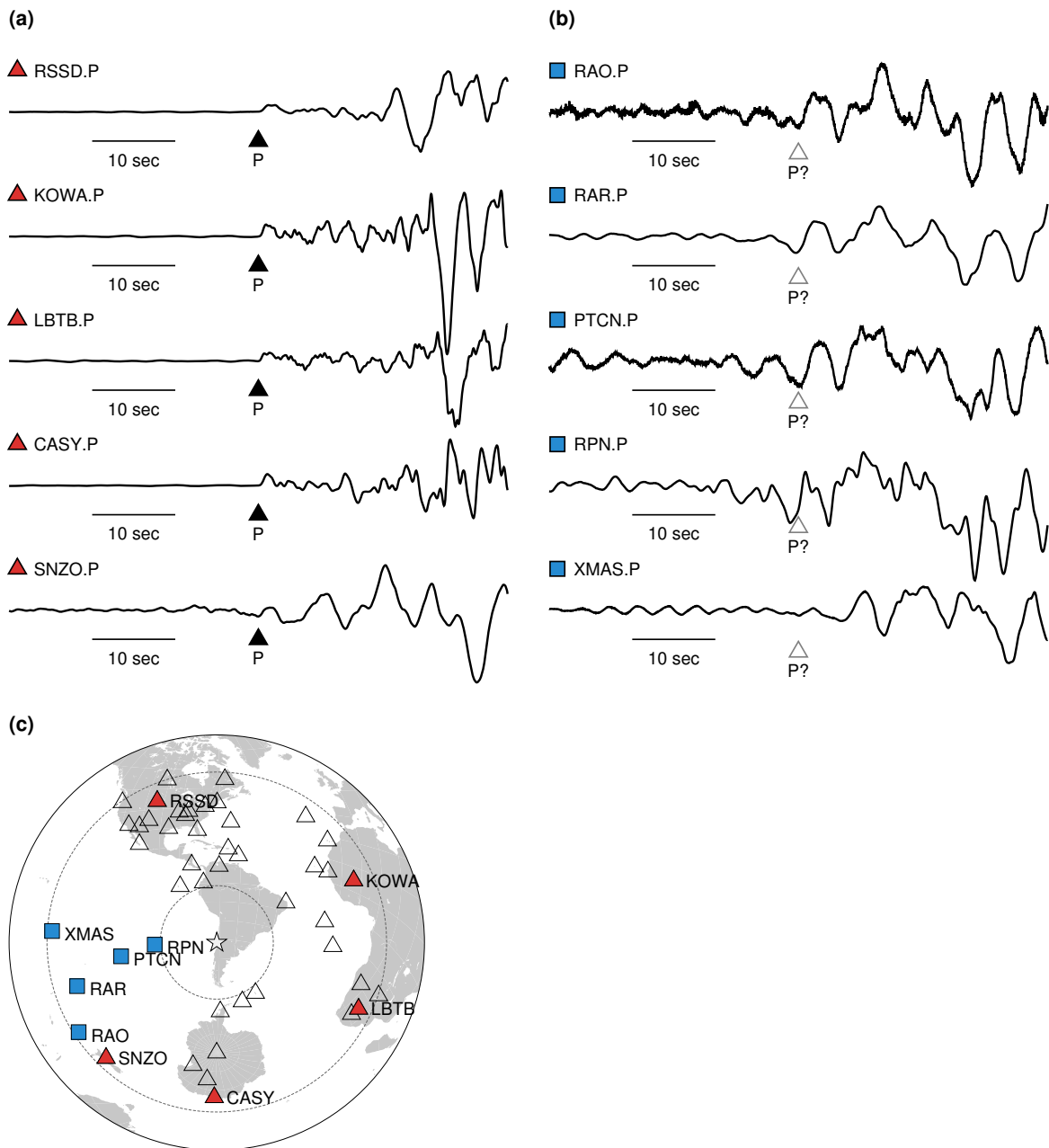
Figure 2.10 Comparison of the waveforms at the GSN-broadband network between (a) the ones that are used in this study and (b) not used in this study. Each trace is the vertical component of unfiltered velocity waveform, and normalized by its maximum absolute amplitude. Closed triangle on each trace of (a) indicates the onset of the P-phase that is manually picked. Open triangle on each trace on (b) indicates the estimated onset of P-phase that is hardly or not reliably picked, compared to the traces on (a). (c) Open and closed red triangles are the stations applied in this study, and the squares are the GSN-broadband stations that are not used in this study corresponding to the traces depicted in (b).

frequency signals from the target ith source node along the fault is extracted by solving the following equations,

$$S_l(t) = |s_l(t)|^N \cdot \frac{s_l(t)}{|s_l(t)|}, \tag{2.4}$$

$$s_l(t) = \sum_j A_j |w_{jl}(t)|^{\frac{1}{N}} \cdot \frac{w_{jl}(t)}{|w_{jl}(t)|}, \tag{2.5}$$

$$w_{jl}(t) = \frac{\dot{u}_j \hat{\times} \dot{G}_{jl}^{\text{calc}}(t)}{\max_{0 \le \alpha \le T} \sqrt{\int_0^T \dot{u}_j^2(\tau + \alpha) d\tau} \cdot \sqrt{\int_0^T \left(\dot{G}_{jl}^{\text{calc}}\right)^2 (\tau) d\tau}}, \tag{2.6}$$

$$\dot{u}_j \hat{\times} \dot{G}_{jl}^{\text{calc}} = \sum_{l'} \left(\dot{D}_{l'} * \dot{G}_{jl'}^{\text{true}}\right) \hat{\times} \dot{G}_{jl}^{\text{calc}}(t),$$

$$= \left(\dot{D}_l * \dot{G}_{jl}^{\text{true}}\right) \hat{\times} \dot{G}_{jl}^{\text{calc}} + \sum_{l' \ne l} \left(\dot{D}_{l'} * \dot{G}_{jl'}^{\text{true}}\right) \hat{\times} \dot{G}_{jl}^{\text{calc}}(t). \tag{2.7}$$

Eqs. (2.4) and (2.5) represent the non-linear Nth root stacking (e.g., Muirhead and Datt, 1976) of the normalized cross-correlation ($\hat{\times}$) function w_{jl} between the observed waveform $\dot{u}_j$ at jth station and the theoretically calculated Green's function $\dot{G}_{jl}^{\text{calc}}$, which enhances the signal to noise ratio of the image. Since the observed waveform are represented as the summation of the convolution ($*$) of the impulsive slip-rate $\dot{D}_l$ and the true Green's function $\dot{G}_{jl}^{\text{true}}$ along all the source nodes l', the cross-correlation function is unfolded as Eq. (2.7). The first term of the right hand side of Eqs. (2.7) is the contribution from the target lth source node (signal part) and the second term is the contribution from the other ($l' \ne l$) source nodes (noise part). If we calculate the better Green's function that is similar to the true Green's function, we can get a high coherence of the cross correlation function because the noise part is cancelled out by stacking, and the signal from the target lth source node that is related to the slip motion $\dot{D}_l$ can be extracted at high resolution. High-frequency (0.3–2.0 Hz) butter-worth band pass

filter is applied to both the observed waveform and the Green's function before cross-correlation, and we adopted $N = 4$ for the Nth root stacking in this study. The HBP method is a variant of the backprojection (BP) method (Ishii *et al.*, 2005). The HBP method can mitigate the systematic delay of projected images of high-frequency sources distorted by the depth phases (pP and sP phases) in the BP method, and by using globally observed waveforms it can produce higher-resolution images than array-based BP methods (e.g., Walker *et al.*, 2005; Okuwaki *et al.*, 2014; Fan and Shearer, 2015). The HBP image can be used as a constraint for the waveform inversion, since it does not require *a priori* assumption of the maximum rupture velocity, rupture direction, and the rupture duration (Okuwaki *et al.*, 2014).

Kinematic waveform inversion methods have been developed since 1980s (e.g., Olson and Apsel, 1982; Hartzell and Heaton, 1983) and applied to the numerous earthquakes to resolve a spatiotemporal behavior of rupture propagation. We estimate the spatiotemporal distribution of co-seismic slip by adopting the inversion formulation developed by Yagi and Fukahata (2011a). This inversion scheme is based on a multi-time window inversion (e.g., Hartzell and Heaton, 1983) that flexibly solves multiple slip events during an earthquake. What is improved from conventional inversion formulations is an introduction of errors (uncertainty) in Green's function (Eq. 6 in Yagi and Fukahata (2011a)), which had been a major source of modeling errors in waveform inversion (e.g., Yagi and Fukahata, 2011a). The strength of the smoothening constraint for the inverted slip and the data covariance matrix including the uncertainty in Green's function are objectively determined by minimizing the Akaike's Bayesian Information Criterion (ABIC Akaike, 1980), which is expressed as Eq. 26 in Yagi and Fukahata (2011a)). Such advantageous features of this inversion formulation are confirmed by applying, for example, for the 2011 Tohoku-oki earthquake (Yagi and Fukahata, 2011b) and the 2008 Wenchuan, China, earthquake (Yagi *et al.*, 2012b). In the 2011 Tohoku-oki earthquake, Yagi and Fukahata (2011b) shows that the modeling errors are regarded as signals, and the slip distribution is distorted by the errors if we neglect the data covariance components originated from the uncertainty in Green's function. In the 2008 Wenchuan earthquake,
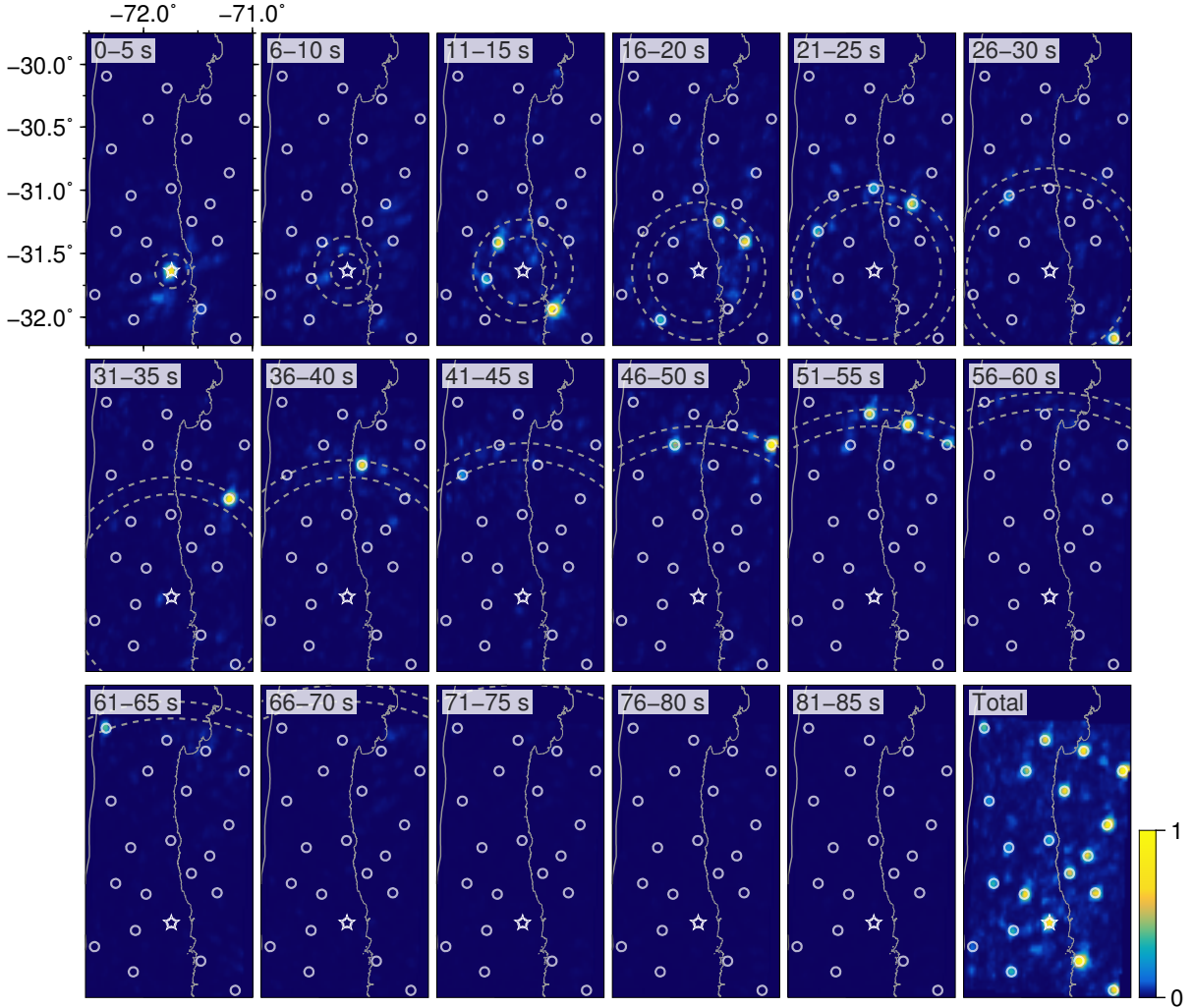
Figure 2.11 Resolution test of the HBP method. 21 nodes, depicted white circles in the above panels, are randomly picked as point sources. Each point source has a triangle slip-velocity function with a half-rise time of 0.25 s and its onset is triggered by a rupture front expanding from the hypocenter and propagating along the fault at constant speed of 3 km/s. Synthetic waveforms were calculated at the sampling rate of 0.05 s (20 Hz), and then filtered in high-frequency (0.3 to 2.0 Hz) band. The fault geometry, adopted stations, and the procedure of the HBP analysis are the same as written in the Data and Methods section. Above panels shows the snapshots of the high-frequency sources every 5 s. The dotted circles on each snapshot represent the rupture fronts at the beginning and the ending time of each snapshot (e.g., rupture fronts at 0 s and 5 s for the snapshot "0–5 s"). As can be seen in the right-bottom panel, the strength of response from the multiple point sources at the shallower part is, in general, weaker than that at the deeper part, despite the fact that we placed the exact same amplitude of the slip velocity function at the point sources. This imaging-artifact may come from the difference of the amplitude of Green's functions along depth due to the assumed velocity structure near the source, and needs to be considered when interpreting the real observation.

more reliable slip-rake angles, that have consistency with the geological observations, are extracted by accounting for the modeling errors due to the uncertainty in Green's function (Yagi *et al.*, 2012b).

For both the HBP and the inversion analyses, the fault geometry was constructed with the constant strike and dip angles being 2.7° and 15.0°, respectively, based on the W phase source inversion by Duputel et al. (`http://wphase.unistra.fr/events/illapel_2015/index.html`, last accessed on 16 November 2015) and the slab geometry around the source region (Hayes *et al.*, 2012; Tassara and Echaurren, 2012). The initial rupture point adopted (assumed hypocenter) was the epicenter (determined by the Centro Sismológico Nacional, Universidad de Chile (CSN: `http://www.sismologia.cl`)) of 31.637°S, 71.741°W, and 25 km depth. For the HBP analysis, the rake angle on each source node was assumed to be pure thrust motion relative to the plate-motion direction, referring the MORVEL model (DeMets *et al.*, 2010). The validity of assumption of the rake angle is tested against the variable rake angles interpolated from the inversion result (Fig. 2.12). From a simple observation of the teleseismic records, there is a clear directivity of rupture toward northern azimuth (Fig. 2.13), and the aftershocks during 1 week following the main shock are densely distributed around and northern part of the epicenter (Fig. 2.8). A preliminary HBP and the BP results hitherto published (Ye *et al.*, 2016a; Melgar *et al.*, 2016) indicates that the high-frequency signals are located northern part of the epicenter. Guided by these information, total available rupture area for both the inversion and the HBP analyses is assumed to be 190 km length and 130 km width, and the initial rupture point is set at 30 km from the southern edge of the fault model. A maximum rupture velocity for the inversion analysis is assumed to be 1.8 km/s based on the preliminary HBP analysis, and the alternative results assuming various maximum rupture velocities are provided in Figs 2.14 and 2.15. The source-node interval along strike and dip directions were 2 km by 2km for the HBP analysis and 10 km by 10 km for the inversion analysis. For the inversion analysis, slip-rate function on each source node was represented as linear B splines with a time length of 35 s and a time interval of 1.0 s, and total source duration was set to be 90 s. Green's functions
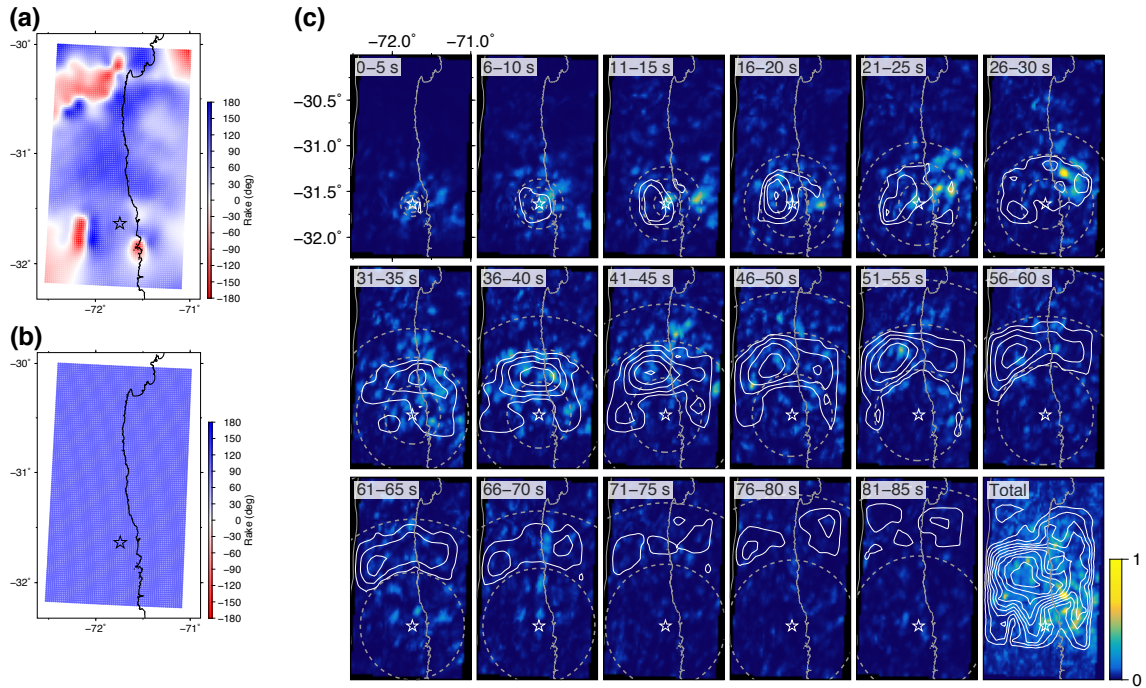
Figure 2.12 The HBP result assuming the variable rake angle obtained from the inversion analysis. Since the node interval for the HBP analysis is finer (2×2 km) than that for the inversion (10×10 km), we distribute the rake angle on each source node for the HBP analysis by linear-interpolating the inverted rake angle. (a) The distribution of the rake angles, which is interpolated from the inversion result, and (b) the distribution of the pure thrust rake angles adopted for the main HBP analysis in the manuscript. (c) Snapshots of the source model taken at every 5 s, with the static distribution at the right-bottom panel and the time is denoted at top-left on each panel. Color represents the normalized intensity of high-frequency signals obtained by the HBP method. For the snapshots, contours are the slip-rate distribution every 0.11 m/s. For the static slip distribution, the contours shows the slip distribution every 1.04 m. The reference rupture-front speeds, expanding from the hypocenter at constant speeds of 1, 2, and 3 km/s are represented as dashed circles. Star denotes the epicenter.

35
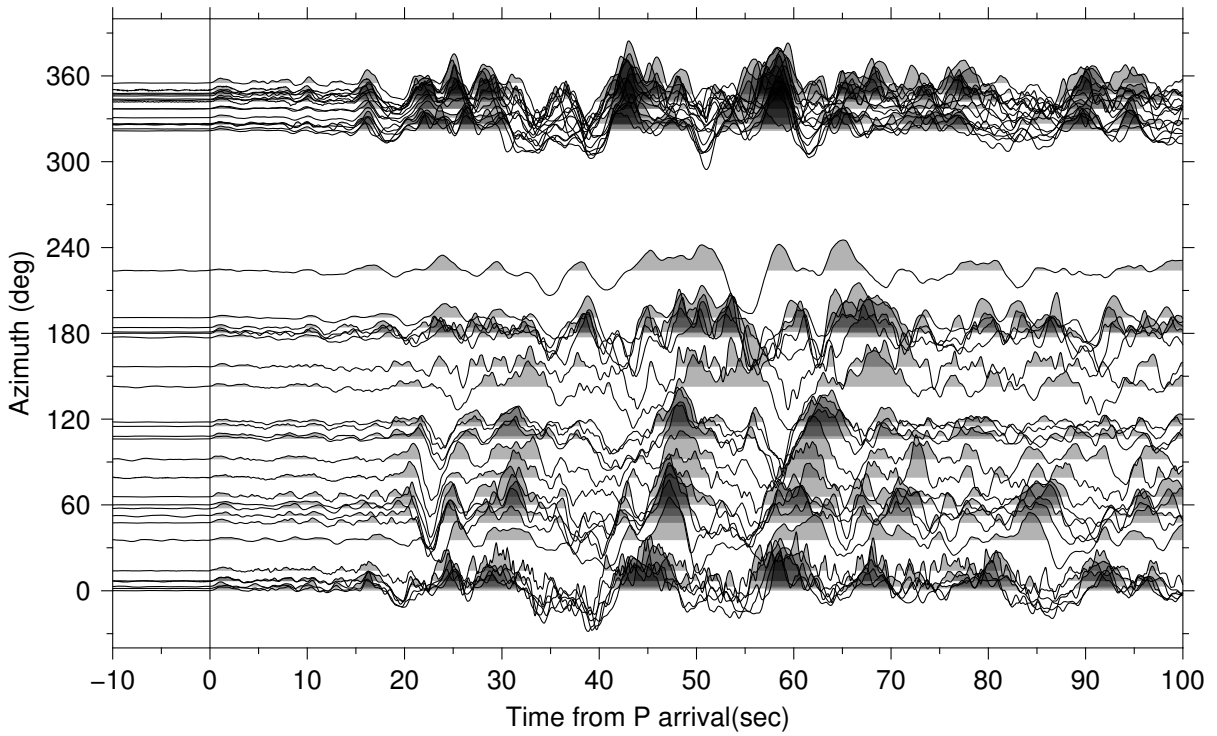
Figure 2.13 Normalized traces of the unfiltered vertical component of P waveforms sorted by azimuth. The set of stations is the same as used in the inversion and the HBP analyses. Positive side of each trace is shaded.

(a) 1.5 km/s (peak slip 11.0 m)

(b) 1.8 km/s (peak slip 10.4 m)

(c) 2.1 km/s (peak slip 9.9 m)

(d) 2.4 km/s (peak slip 8.1 m)
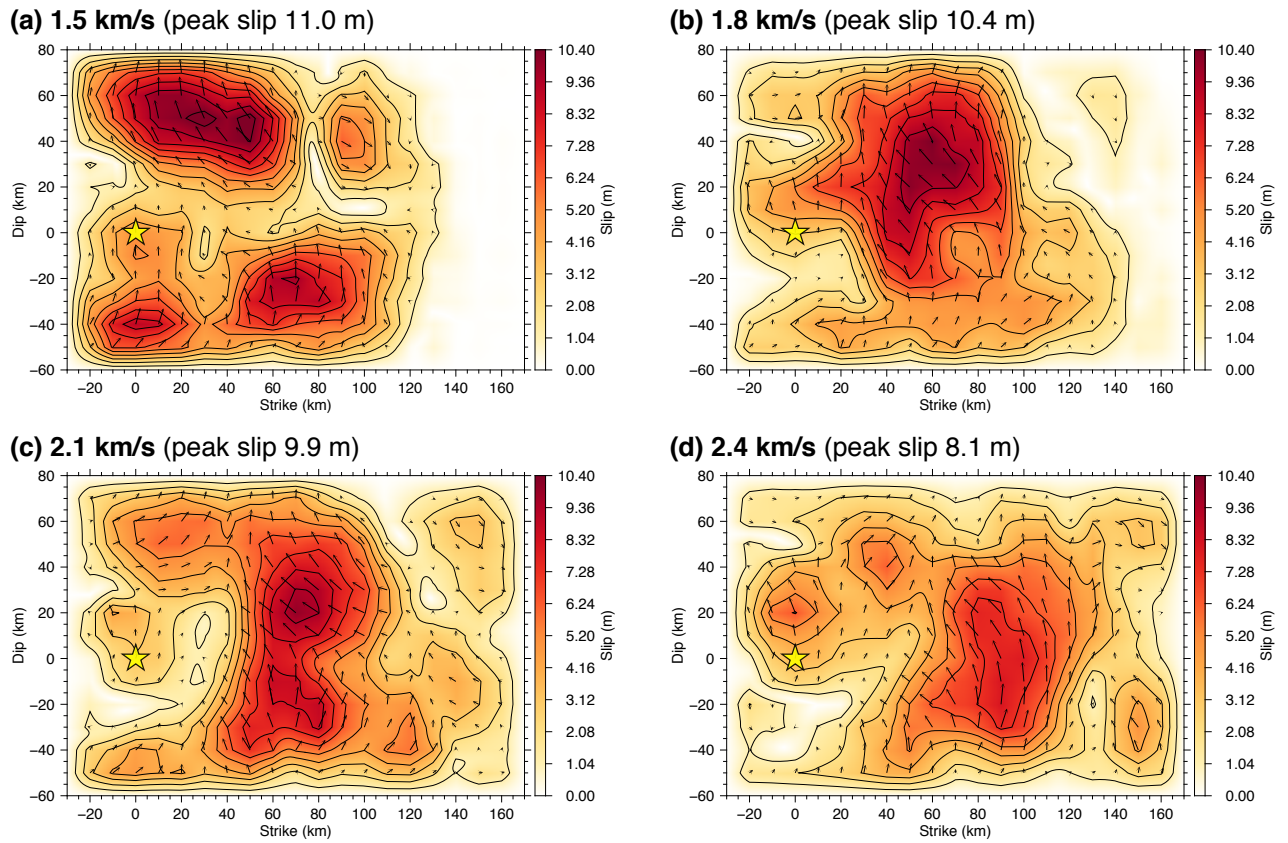
Figure 2.14 Comparison of the slip models from the different assumptions of the maximum rupture velocity of (a) 1.5, (b) 1.8, (c) 2.1, and (d) 2.4 km/s. A contour on each figure represents every 1.04 m slip, and the color map is common for all slip models as the main analysis (b). The star and the arrow denote the hypocenter and the slip vector, respectively.
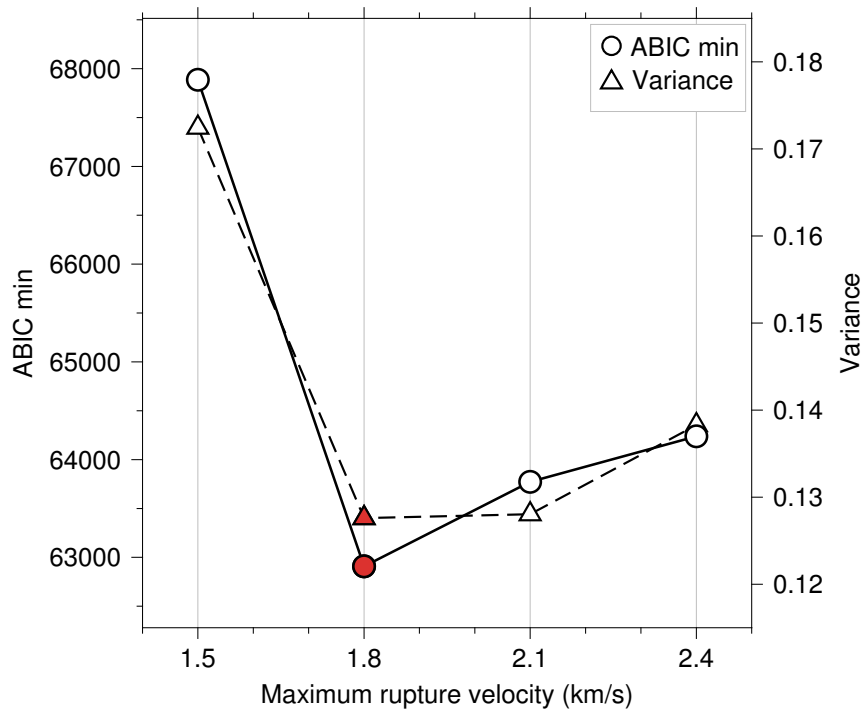
Figure 2.15 The plot shows the assumed maximum rupture velocity versus the minimum value of the ABIC and the variance between the observed waveforms and the synthetics shown in Fig. 2.14. Red symbols are from the result of the main analysis assuming 1.8 km/s rupture velocity.

Table 2.3 Near-source structure used to calculate Green's functions for the 2015 Illapel Chile earthquake

V_P (km/s)	V_S (km/s)	Density (10^3kg/cm^3)	Thickness (km)
1.50	0.00	1.02	4.00
4.80	2.77	2.72	4.00
5.50	3.18	2.72	4.00
6.00	3.46	2.86	4.00
6.40	3.70	2.86	6.00
6.80	3.93	3.03	8.00
7.80	4.32	3.42	0.00

are calculated based on the method of Kikuchi and Kanamori (1991) with the local velocity structure (Table 2.3) extracted from the tomographic 2-D velocity-depth model of Contreras-Reyes *et al.* (2014) and the CRUST1.0 model (Laske *et al.*, 2013). Travel times, geometrical spreading factors and ray parameters for the pair of each source node and station are calculated with the ak135 model (Kennett *et al.*, 1995).

2.2.3 Co-seismic slip evolution

The total slip distribution and the moment-rate function are shown in Fig 2.8. The slip-rake angles obtained by the waveform inversion are generally consistent with the thrust motion against the plate convergence (Fig. 2.16). Large slip focuses on shallow, up-dip portion of the fault plane where a maximum slip reaches 10.4 m at 72 km northwest of the epicenter. The total seismic moment release leads to 3.3×1021 Nm (M_W 8.3). Slight difference in the seismic moment from other study (e.g., 2.67×10^{21} Nm Ye *et al.*, 2016b) may be due to the differences in the assumption of the model-fault geometry and the resultant locations of the inverted slip along the dip direction, since the seismic moment depends on assumed rigidity, which increases with depth.

Fig. 2.17 shows the spatiotemporal distribution of slip-rate and high-frequency sources, and we project the Fig. 2.17 into the strike (Fig. 2.18a) and dip directions (Fig. 2.18b) in order to present the details of the rupture propagation history. For the first 25
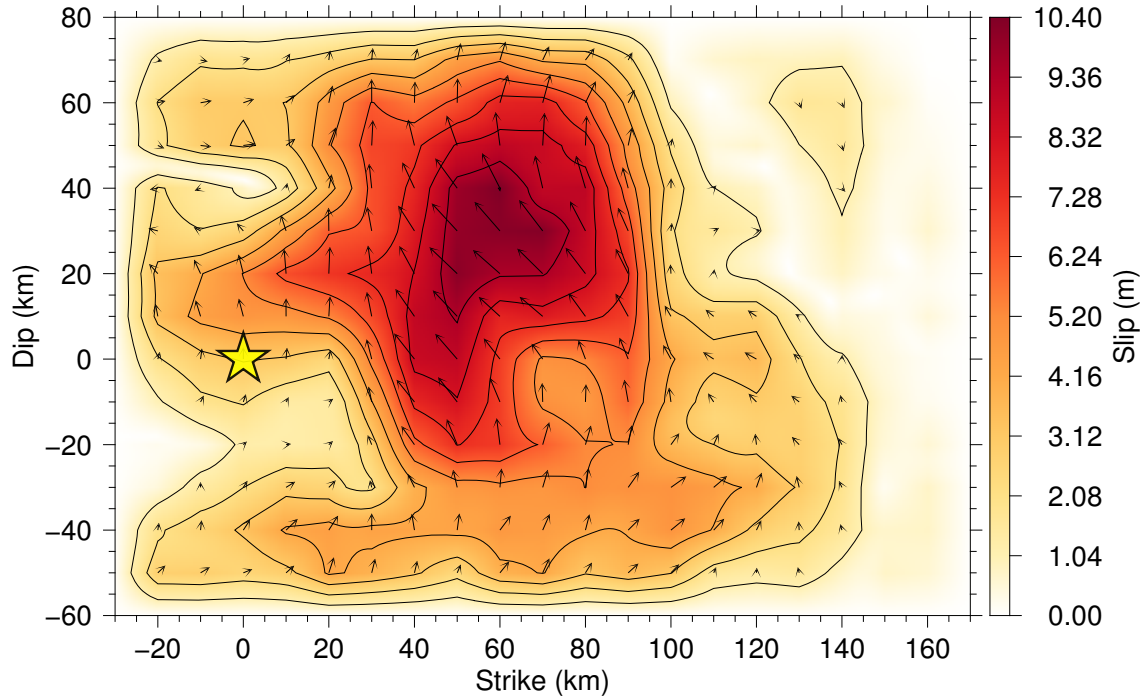
Figure 2.16 Total slip distribution for the main analysis in a strike-dip view. The star
and the arrow denote the hypocenter and the slip vector, respectively. The
contour outlines the slip every 1.04 m.

s after the hypocentral time, the rupture initiated at the hypocenter and propagated

mainly north-westward with rupture speed of 2 km/s, and left large slip-rate area at 16

km northwest of the epicenter. Then from 30 s after the initiation of rupture, the rup-

ture front started propagating from the down-dip portion at 60 km northeast from the

epicenter. The rupture front propagated to the shallow, up-dip part of the fault plane,

and brought about the largest slip at 72 km northwest of the epicenter at 50 s from the

hypocentral time, where the peak seismic moment release-rate (8.8×10^{19} Nm/s) was

obtained, and the slip terminated at 90 s.

2.2.4 Evolution of high-frequency sources

Spatiotemporal distribution of high-frequency sources shows that relatively weak strength

of high-frequency sources initially propagated down-dip, northeast of the epicenter, and

then returned to the up-dip portion of the fault plane at the speed of 2 km/s (Fig.
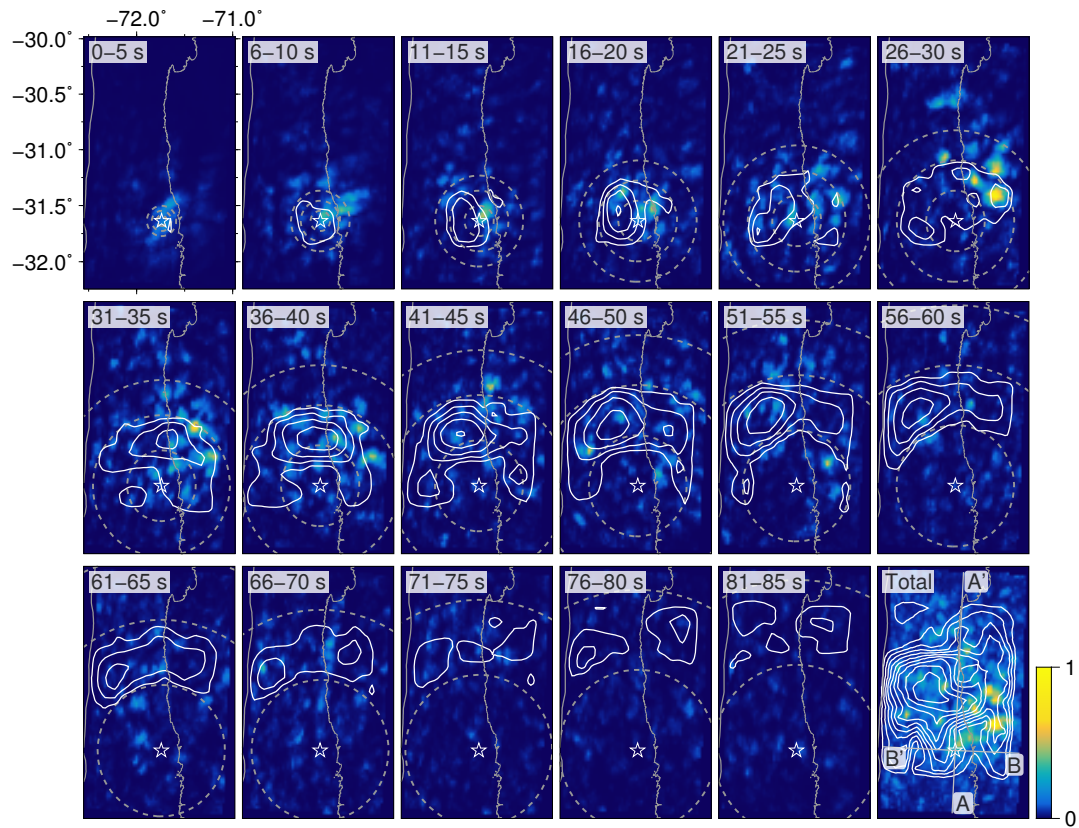
Figure 2.17 Snapshots of inverted slip-rate and high-frequency source evolution taken at 5 s interval, and the relevant time window is denoted at top-left on each panel. The color represents the relative intensity of the high-frequency signal. Solid contour shows the slip-rate distribution drawn at 0.11 m/s interval. Dashed contour shows the reference rupture speed expanding from the hypocenter at 1, 2, and 3 km/s. The static slip distribution (1.04 m contour) and the high-frequency sources are shown in the right-bottom panel. Lines A–A' and B–B' are corresponding to the projections of Figs. 2.18a and b.
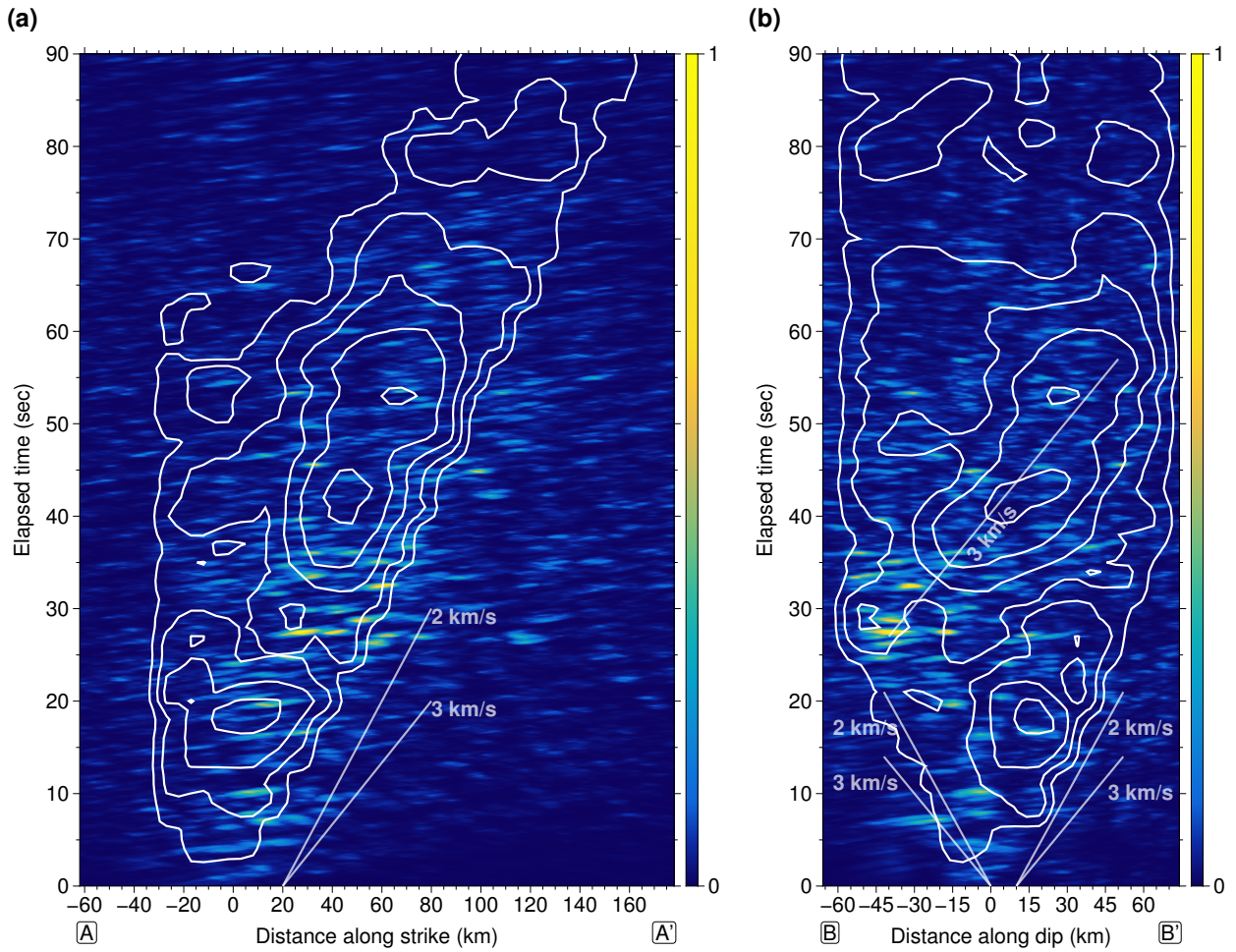
Figure 2.18 Time evolution of the slip-rate and the high-frequency sources along (a) the strike and (b) dip directions. Abscissa represents the distance from the epicenter along (a) the strike and (b) dip directions. Ordinate is the elapsed time from the hypocentral time. Solid lines are the reference rupture speeds. Background color and contour interval is the same as Fig. 2.17.

2.18b). From 20 s, the high-frequency sources started propagating down-dip again at the speed of 3 km/s along the dip direction, and at 25 s to 27 s the relatively strong high-frequency radiation was observed at 60 km northeast of the epicenter. From 30 s to 90 s, high-frequency sources seemed to propagate up-dip at the speed of about 3 km/s along the dip direction (Fig. 2.18b). The strength of high-frequency sources is relatively weak at this sequence, and the high-frequency radiation ceased after 80 s.

3 | Uncertainty in backprojection image

As shown in the last chapter, the BP technique should be a strong tool for imaging the high-frequency sources, and hence the rupture irregularity. However, the relationship between the BP image and the fault slip is still unclear, which should be an obstacle for the direct comparison with the co-seismic slip distribution resolved by the waveform inversion, and the physical interpretation of the BP image. In this chapter, we clarify the theoretical background of the BP and HBP methods, and show that the BP and HBP images have an inherent depth-dependent bias. We then propose the new formulations for the BP and HBP methods that suppress the depth-dependent bias and relate the BP image to the slip motion along the fault interface.

3.1 | Introduction to backprojection: What is left unsolved?

Waveform backprojection (BP) is a technique for tracking the source evolution of specific seismic phases (e.g., the P phase) during an earthquake (see Kiser and Ishii, 2017, for a comprehensive review of BP). Owing to its robustness and applicability to high-frequency waveforms, BP has been used for extracting information about earthquake-rupture evolution that is missed by the analyses of low-frequency waveforms by kinematic source inversion, including, for example, complex rupture evolution associated with the geometric features of a fault system (Meng *et al.*, 2012a; Uchide *et al.*, 2013; Vallée and Satriano, 2014; Okuwaki and Yagi, 2018), cascading asperity ruptures (Okuwaki *et al.*, 2014, 2016), triggering ruptures of very early aftershocks (D'Amico *et al.*, 2010; Kiser and Ishii, 2013; Fan and Shearer, 2016), multiple branching ruptures (Meng *et al.*, 2012b; Satriano *et al.*, 2012; Fan *et al.*, 2016, 2017), frequency-dependent wave radiation of subduction zone megathrust earthquakes (Kiser and Ishii, 2011; Wang and Mori, 2011; Yao *et al.*, 2013; Satriano *et al.*, 2014; Yin *et al.*, 2016, 2018), and mechanisms of deep earthquakes (Suzuki and Yagi, 2011; Kiser *et al.*, 2011; Ye *et al.*, 2013).

High-frequency waves are generated by abrupt changes of rupture velocity and/or slip velocity according to theoretical works and dynamic simulation of rupture propagation (Madariaga, 1977; Bernard and Madariaga, 1984; Spudich and Frazer, 1984; Madariaga *et al.*, 2006; Beresnev, 2017). Fluctuation of rupture evolution can be cased when the source area involves barriers or asperities, inluding fault roughness along the fault surface (Das and Aki, 1977; Aki, 1979; Dunham *et al.*, 2011; Shi and Day, 2013; Bruhat *et al.*, 2016; Mai *et al.*, 2017). The series of observations using the BP techniques have shown that the intense high-frequency radiation occurs just before the rupture-front penetrates a large-slip region or geometric barriers (e.g., Uchide *et al.*, 2013; Yagi and Okuwaki, 2015; Okuwaki and Yagi, 2018), which is consistent with our theoretical understanding of the generation of high-frequency radiation. However, in the case of some subduction-zone megathrust earthquakes, a distinct anti-correlation between the high-frequency sources and large-slip zone with respect to depth has been reported. The intense high-frequency signal tends to locate at down-dip part of the shallow large slip area, which

may reflect the rupture of heterogeneous, small high-stress patches. This finding leads to the idea that rupture properties within these subduction zones are segmented along depth (Koper *et al.*, 2012; Lay *et al.*, 2012; Ye *et al.*, 2016b). This idea may be useful for a unified understanding of subduction-zone megathrust earthquakes involving the apparent diversity of source rupture evolution.

However, the tendency of lacking intense high-frequency signal at the shallow part of the seismogenic zone generally observed through application of BP methods may not directly draw conclusion that the intensity of kinematic features responsible for high-frequency radiation increases with depth. Since the observations show that the rupture front often goes along both up-dip and down-dip directions (e.g., M_W 9.0 2011 Tohoku-oki, Japan and M_W 8.3 2015 Illapel, Chile, earthquakes; Meng *et al.*, 2011; Melgar *et al.*, 2016; Meng *et al.*, 2018), it is plausible that there exist kinematic features around the rupture tip or the healing front (e.g., Madariaga *et al.*, 2006) even at shallow. In fact, as shown in Section 4.3.4, BP and HBP images are not simple representation of kinematic features of the source process, and they have an inherent depth-dependent bias that is proportional to the amplitude of the Green's function.

In this chapter, we propose variant BP techniques that enable us to extract kinematic features of rupture evolution from high-frequency waveform data. We first review the mathematical representation of the BP method, following the pioneering work of Fukahata *et al.* (2014), who have clarified the theoretical background of the BP techniques and showed that a BP image can be related to slip motion as either slip velocity or slip acceleration. However, because Fukahata *et al.* (2014) basically considered the case of a point source, they did not discuss in detail the normalizing factor adopted for the BP methods. We point out the importance of the normalizing factor, which plays a critical role in the resultant signal intensity for the case of multiple-point sources. We consider both the original time-domain BP method (e.g., Ishii *et al.*, 2005) and the Hybrid back-projection (HBP) method (Yagi *et al.*, 2012a; Okuwaki *et al.*, 2014) that we introduced in the previous chapters. We clarify the theoretical meaning of the signal intensity obtained by the BP and HBP methods, which depends on the amplitude of the Green's

function and is not directly related to the slip motion. We examine this theoretical outcome through numerical experiments using synthetic waveforms generated with the controlled-synthetic sources, and confirm that the resultant signal intensity obtained by the original BP and HBP methods have an inherent depth dependence, which is originated from the specific design of the normalizing factor. We propose new variants of the BP and HBP methods; called kinematic BP and HBP methods, by taking the effect of the normalizing factor into account. The kinematic BP and HBP methods allow us to remove the depth-dependent bias in the original BP and HBP images and retrieve signal intensities that are related to slip velocity or slip acceleration. We test the newly proposed methods through the numerical experiments and application to the real waveforms of the M_W 8.3 2015 Illapel, Chile, earthquake, and confirm that the relative signal intensity is related to the slip motion by the kinematic BP and HBP methods.

3.2 | Depth dependence in the BP and HBP images

In this section, we investigate the mathematical expressions of the original BP and HBP methods, following the pioneering works by Ishii *et al.* (2005, 2007); Yagi *et al.* (2012a); Fukahata *et al.* (2014). Particularly, we consider the role of the normalizing factors in the implementations and their effect on the resultant signal intensity, which was not addressed in detail by Fukahata *et al.* (2014). We then perform a numerical test by using synthetic waveforms to demonstrate that both the BP and HBP images have an inherent depth dependence that is proportional to the amplitude of the Green's function for a unit-step slip.

3.2.1 Representation of BP

A BP image is made by stacking observed waveforms as follows:

$$s_i^{\mathrm{BP}}(t) = \sum_j w_j \frac{u_j(t + t_{ij}^p)}{A_j}, \tag{3.1}$$

where $s_i^{\mathrm{BP}}(t)$ is the signal intensity of the BP image at the ith source location at hypocentral time t (where $t = 0$ corresponds to the origin time of the earthquake), and $u_j(t + t_{ij}^p)$ is the observed waveform at the jth station that is time-shifted by the theoretical travel time of the P phase t_{ij}^p between the ith source location and the jth station. For simplicity, we neglect the calibration of travel time error (Ishii $et\ al.$, 2007; Fan and Shearer, 2017) and the slowness correction (Meng $et\ al.$, 2016). w_j is a weighting factor for each waveform, which is introduced to avoid spatial bias due to the station distribution; w_j is usually designed to be negatively correlated with station density and sums to 1, that is, $\sum_j w_j = 1$ (details are shown in Section 3.2.3). The normalizing term A_j is given by the root-sum-square of the observed waveform,

$$A_j = \mathrm{pol}(u_j) \cdot \sqrt{\int_0^T u_j^2(\tau + t_j^p) d\tau}, \qquad (3.2)$$

where $\mathrm{pol}(u_j) \in \{-1, +1\}$ is the polarity of the first motion of waveform u_j, t_j^p is the P-phase arrival time at the jth station, and T is the waveform length. The normalizing factor can also be represented by the maximum amplitude of the observed waveform, although these forms of the normalizing factor were not presented explicitly in the relevant papers. In this study, we use the representation in eq. (3.2), because of its similarity to the normalizing factor in the HBP method defined in eq. (3.8). The observed waveform u_j can be expressed as

$$u_j(t) = \sum_{i'} \left(a_{i'} * G_{i'j} \right)(t)$$
$$= \left(a_i * G_{ij} \right)(t) + \sum_{i'(\neq i)} \left(a_{i'} * G_{i'j} \right)(t), \qquad (3.3)$$

where a_i is the slip motion at the ith source location on the fault surface, $*$ denotes convolution, and we neglect the background noise of the observed waveform for simplicity. The Green's function G_{ij} in eq. (3.3) is the deformation at the jth station due to a unit-step slip on the ith subfault. For the velocity data u_j, slip motion a_i may represent slip velocity if the Green's function is a propagator from slip velocity to far-field velocity,

or slip acceleration if the Green's function is a propagator from slip velocity to far-field displacement (Fukahata *et al.*, 2014). Hereafter, we refer to the slip motion a_i as slip velocity, considering together that the waveform u_j is velocity data and the Green's function G_{ij} is for unit-step slip velocity. By substituting eq. (3.3) into eq. (3.1), we get the following expression for the signal intensity,

$$s_i^{\mathrm{BP}}(t) = \sum_j \frac{w_j}{A_j} \left((a_i * G_{ij})(t + t_{ij}^p) + \sum_{i'(\neq i)} (a_{i'} * G_{i'j})(t + t_{ij}^p) \right). \qquad (3.4)$$

As shown in eq. (3.4), eq. (3.1) is divided into two terms: the first term is the signal that corresponds to the contribution from the ith source, and the second term is noise, which is the contribution from other i'th locations. If the noise term can be assumed to be suppressed by stacking (Fukahata *et al.*, 2014) as,

$$\sum_j \frac{w_j}{A_j} \left(\sum_{i'(\neq i)} (a_{i'} * G_{i'j})(t + t_{ij}^p) \right) \approx 0, \qquad (3.5)$$

then the signal intensity at the ith location can ideally be represented as

$$s_i^{\mathrm{BP}}(t) \approx \sum_j \frac{w_j}{A_j} (a_i * G_{ij})(t + t_{ij}^p), \qquad (3.6)$$

where the signal intensity at the ith source location s_i^{BP} represents the slip velocity at the ith source location a_i, which scales with the normalizing factor A_j and the Green's function G_{ij}. Hence, the signal intensity s_i^{BP} is not uniquely determined by the amplitude of the slip velocity at the ith source location a_i, but is additionally controlled by a scaling factor composed of A_j and G_{ij}, which depends on the source location because its numerator includes G_{ij}.

3.2.2 Representation of HBP

The HBP image is made by stacking cross-correlation functions of the observed waveform and the Green's function:

$$s_i^{\text{HBP}}(t) = \sum_j w_j \frac{\left(u_j \hat{\times} G_{ij}^p\right)(t)}{A_{ij}} = \sum_j w_j \frac{\int_0^T u_j(\tau) G_{ij}^p(\tau - t) d\tau}{A_{ij}} \tag{3.7}$$

where $\hat{\times}$ denotes cross-correlation, and G_{ij}^p is the theoretical Green's function that corresponds to the deformation due to a unit-step slip velocity. T is the time period of the cross-correlation function of the waveform and the Green's function. The weighting factor w_j is the same as in eq. (3.1), and the normalizing factor A_{ij} is represented as

$$A_{ij} = \sqrt{\int_0^T u_j^2(\tau + t_j^p) d\tau} \cdot \sqrt{\int_0^T G_{ij}^{p\,2}(\tau + t_{ij}^p) d\tau}, \tag{3.8}$$

which is designed to normalize the cross-correlation function in the numerator of eq. (3.7). Eq. (3.3) can be used to expand eq. (3.7) into signal and noise terms as follows:

$$s_i^{\text{HBP}}(t) = \sum_j \frac{w_j}{A_{ij}} \left[\left((a_i * G_{ij}) \hat{\times} G_{ij}^p\right)(t) + \sum_{i'(\neq i)} \left((a_{i'} * G_{i'j}) \hat{\times} G_{ij}^p\right)(t) \right]. \tag{3.9}$$

If the noise term can be assumed to be suppressed by stacking (Fukahata *et al.*, 2014) as

$$\sum_j \frac{w_j}{A_{ij}} \left(\sum_{i'(\neq i)} (a_{i'} * G_{i'j}) \hat{\times} G_{ij}^p \right)(t) \approx 0, \tag{3.10}$$

the final form of the signal intensity is

$$s_i^{\text{HBP}}(t) \approx \sum_j \frac{w_j}{A_{ij}} \left((a_i * G_{ij}) \hat{\times} G_{ij}^p\right)(t). \tag{3.11}$$

The resultant signal intensity at the ith source location s_i^{HBP} represents the slip velocity a_i scaled with a weighting factor w_j, the normalizing factor A_{ij} and the cross-correlation

function of the Green's functions. Eq. (3.11) indicates that the resultant signal intensity of the HBP method is also expected to correlate with the source location because the scaling factor includes the Green's functions.

3.2.3 Numerical test

As seen in eqs. (3.6) and (3.11), the signal intensity of the BP and HBP images is not a simple representation of the slip motion at the specific source location; but rather, it includes additional contributions from the normalizing factors and the Green's functions. We performed a numerical test with synthetic waveforms computed using a known slip velocity a to empirically show how the scaling factors in eqs. (3.6) and (3.11) affect the resultant BP and HBP images. First, we generated synthetic waveforms using 20 point sources that were randomly distributed on a dipping model plane in the Chilean subduction zone (Fig. 3.1a). Each point source has a uniform potency of 4×10^6 m^3 (2×2 km^2 area $\times$ 1 m slip for pure thrust motion against the relative plate motion; DeMets *et al.*, 2010), which is composed of a triangular slip-rate function with a half-rise time of 0.25 s computed at a sampling frequency of 20 Hz (Fig. 3.1d). The model plane is a 190×130 km^2 rectangle with strike and dip angles of 2.7° and 15°, respectively, that has been discretized for point sources with a spatial resolution of 2 km $\times$ 2 km in both strike and dip directions. The initial rupture point (hypocenter) is located at 31.637°S, 71.741°W, and 25-km depth. Each point source is triggered to rupture by the expanding circular rupture front propagating at a constant speed of 3 km/s from the hypocenter (Fig. 3.1c). The Green's function that is convolved with the slip-rate function to generate the synthetic waveforms is calculated by the method of Kikuchi and Kanamori (1991). Near the source area, a layered medium (Table 3.1) is used for calculating the Haskell propagator matrix for the Green's function, and the ak135 model (Kennett *et al.*, 1995) is used to calculate geometrical spreading factors, ray parameters, and travel times. The synthetic waveforms were calculated for the stations at teleseismic distances between 30° to 90° (Fig. 3.1e), and the weighting factor w_j in eqs. (3.1) and
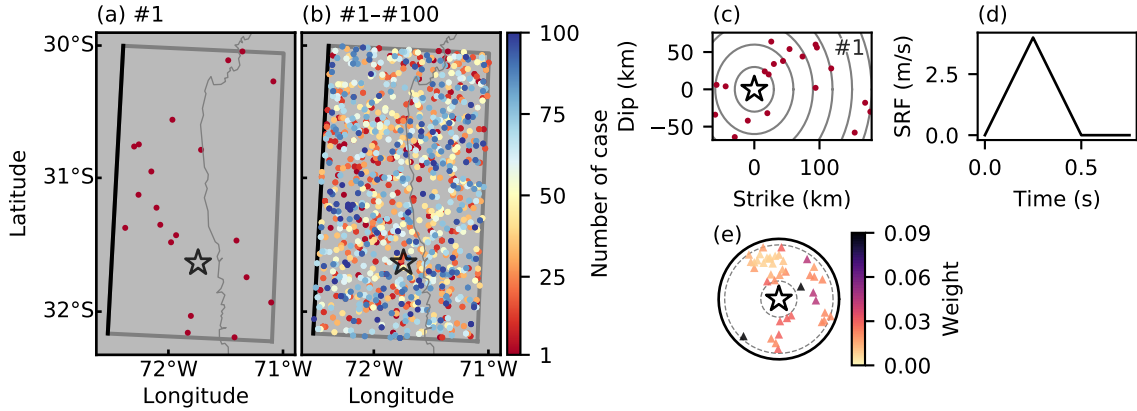
Figure 3.1 (a) The distributions of randomly selected point sources for the case #1 and
(b) all the point sources through the cases #1 to #100 are shown as colored
dots. Star denotes the initial rupture point (epicenter). The model-fault
plane with a dip angle of 15° is outlined by the gray rectangle, with the up-
dip limit as black line. The coastline is shown as thin-gray curved line. (c)
Relation between the point-source location (red dot) and the rupture front
for the case 1. The star denotes the nucleation point. Gray circles represent
the constantly propagating rupture front snapshotted at 10 s interval. (d)
Slip-rate function (SRF) built in each point source. (e) Observation station
distribution denoted as triangles. The star denotes the nucleation point, and
the gray dashed circles show epicentral distances at 30° and 90°. Color of
each triangle represents the weight defined in eq. (3.12).

Table 3.1 Near-source structure used to calculate Green's function.

V_P (km/s)	V_S (km/s)	Density $(10^3 kg/cm^3)$	Thickness (km)
1.50	0.00	1.02	4.00
4.80	2.77	2.72	4.00
5.50	3.18	2.72	4.00
6.00	3.46	2.86	4.00
6.40	3.70	2.86	6.00
6.80	3.93	3.03	8.00
7.80	4.32	3.42	0.00

(3.7) is calculated according to the following rules:

$$w_j = \frac{r_j}{\sum_j r_j},$$
$$r_j = \frac{1}{\sum_{j'} m_{jj'}},$$
$$m_{jj'} = \begin{cases} 1 & (\Delta_{jj'} \leq 20°) \\ 0 & (\Delta_{jj'} > 20°), \end{cases} \tag{3.12}$$

where $\Delta_{jj'}$ is the epicentral distance between a pair of stations. In the BP method, this weighting factor is based on globally distributed stations (e.g., Fan and Shearer, 2015), whereas when the BP method is applied to an array of stations, the weighting factor is represented by, for example, a cosine function (Ishii *et al.*, 2007), and the weight given to the waveform decays with distance from the centre of the station array. Note that in this test, the hypocenter, fault geometry, station configuration, and near-source velocity structures are those used in seismic source study of the M_W 8.3 2015 Illapel, Chile, earthquake (Okuwaki *et al.*, 2016). We used the BP and HBP methods to backproject the synthetic waveforms onto the fault. To show systematic bias independent of specific point-source distributions, we computed backprojection images for 100 cases of 20 randomly selected point sources (Fig. 3.1b).

We then plotted the backprojected signal intensities at the locations of point sources shown in Fig. 3.1(b) both in map view (Figs. 3.2a and b) and along depth (Figs. 3.3a and b). The result shows a clear depth dependence of the backprojected signal intensity on the model fault plane, where the signal intensity increases with the depth of the point sources even though we generated the synthetic waveforms by assuming the same potency at all the point sources. The mean values of the signal intensities measured within 5-km-depth bins monotonically increase from the shallowest to deepest bins; 0.52 ± 0.13 to 0.85 ± 0.12 and 0.55 ± 0.10 to 0.90 ± 0.10 for the original BP and HBP methods, respectively (Figs. 3.3a and b). This depth dependence in both the BP and HBP images reflects the depth dependence of the fractions in eqs. (3.6) and (3.11), which have the Green's functions as their numerator and the normalizing factor
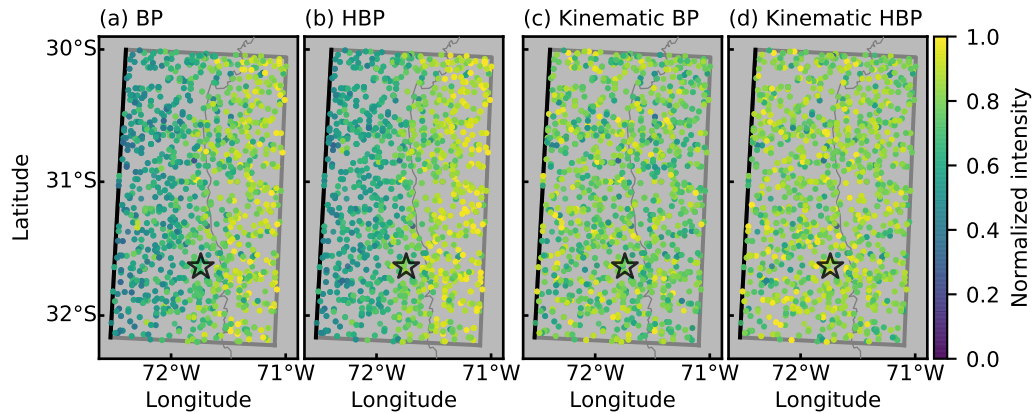
Figure 3.2 Map view of the result with the (a) original BP, (b) original HBP, (c) kinematic BP, and (d) kinematic HBP methods. Color represents the maximum intensity of the backprojected signal among the source duration, which is normalized by the maximum intensity among backprojected images for each case of #1 to #100. The gray rectangle outlines the model fault plane, the black line is the up-dip limit of the fault area, and the star denotes the nucleation point (hypocenter). The thin gray curved line shows the coastline.
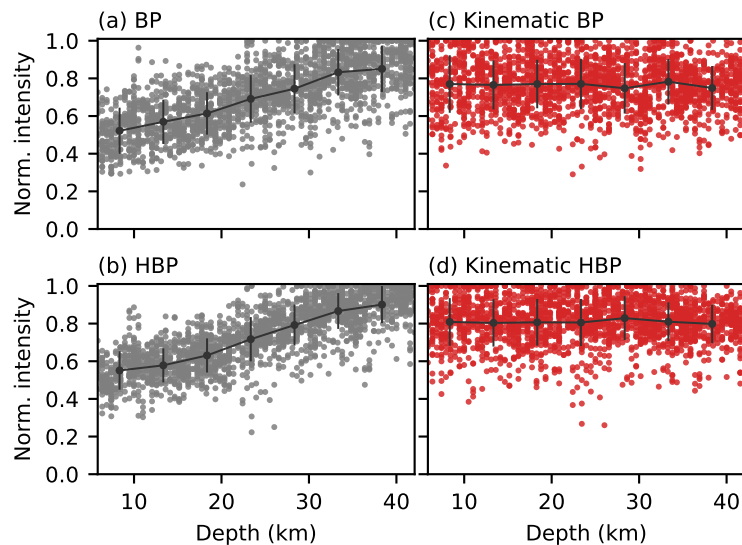
Figure 3.3 Depth view of the normalized intensity of images obtained by the (a) original BP, (b) original HBP, (c) kinematic BP, and (d) kinematic HBP methods. Abscissa is the depth of point sources, and the ordinate is the normalized intensity of the backprojected images. Black dot is the mean value of the signal intensities within each 5-km-depth bin. One standard deviation of the signal intensities within each depth bin is shown as the vertical error bar.
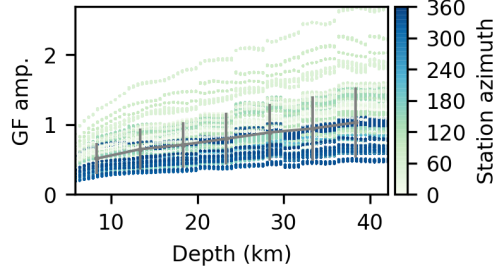
Figure 3.4 Maximum amplitude of Green's functions (GF amp.) for all the pairs of source node and station in 10^{-6}m as a function of depth of the source node, used in both the synthetic tests and the real application. Color represents the station azimuth. Gray vertical line shows the standard deviation of the amplitude within 5-km-depth bins.

as their denominator, because we used the unified amplitude of slip-rate function for generating the synthetic waveforms. In our numerical experiments, we assumed the model-fault plane dipping at 15° embedded in a layered medium (Table 3.1), and the Green's function displays a depth dependence related to the rigidity of the medium and to geometrical spreading factors, both of which become larger with depth (Fig. 3.4). Thus, from both the mathematical expressions and the numerical experiments, we can conclude that the BP and HBP methods are inherently designed to retrieve contributions of wave radiation to entire waveforms, which should be proportional to the amplitude of the Green's functions. Note that the weighting factor w_j fluctuates at most 9% for the station configuration adopted in this numerical test (Fig. 3.1e), which does not significantly affect the signal intensity. The numerical test presented in this chapter extends the result of Fukahata *et al.* (2014), where they did not consider the effect of a scaling factor due to the amplitude of the Green's function, because they considered the case of a single point source and did not take into account the effect that depends on the source location. For the case of multiple-point sources (Fig. 3.1), however, the dependence of the signal intensity on the source location has clearly emerged (Figs. 3.2a and b and 3.3a and b), because the scaling factor is proportional to the amplitude of the Green's function which depends on the source location, which is shown in eqs. (3.6) and (3.11).

3.3 | Beyond the depth-dependent bias: Kinematic BP and HBP methods to image slip motion

The depth dependence of the BP and HBP images (Figs. 3.2a and b and 3.3a and b) highlights the inherent design of the BP and HBP methods, which extracts the relative strength of the wave radiation that is proportional to the amplitude of the Green's function. In other words, the BP and HBP images are biased when they are interpreted as the slip motion, and the BP and HBP images cannot directly be compared to the slip distribution to discuss the rupture property. However, BP and HBP methods are potentially useful for investigating the details of rupture properties or slip motion recorded in high-frequency waveforms. Therefore, it would be convenient if we can design BP and HBP methods to retrieve the slip motion on a fault plane from the backprojected images. For this purpose, we propose variants of the BP and HBP methods in which the normalizing factors in eqs. (3.1) and (3.7) of the original BP and HBP methods are appropriately modified. We then test the proposed methods in the same situation as described in Section 3.2.3 and also apply them to real waveforms of the M_{W} 8.3 2015 Illapel, Chile, earthquake.

3.3.1 Modification in kinematic BP and HBP methods and synthetic test

In order to retrieve the slip motion from the signal intensity, we modify the BP and HBP methods by changing the normalizing factors to cancel out the numerators of the signal terms, G_{ij} in eq. (3.6) and $G_{ij}\hat{\times}G_{ij}^p$ in eq. (3.11). For the BP method, we propose a normalizing factor A_{ij}^{kBP} as

$$A_{ij}^{\mathrm{kBP}} = g_{ij}^p, \tag{3.13}$$

where g_{ij}^p is the amplitude of the first motion of the theoretical Green's function, which corresponds to the first local maximum (or minimum if polarity is down) of the amplitude from the arrival time. For the HBP method, we modify the normalizing factor A_{ij} in

eq. (3.8) by using the theoretical Green's function G_{ij}^p:

$$A_{ij}^{\text{kHBP}} = \int_0^T G_{ij}^{p\,2}(\tau + t_{ij}^p)d\tau. \tag{3.14}$$

The bias in the original BP and HBP images (Section 3.2.3) is expected to be corrected by this modification of the normalizing factors. Thus, the kinematic BP and HBP images should be more directly related to the slip motion on a fault.

The same numerical test that we carried out in Section 3.2.3 is performed to examine how the proposed normalization factors modify the resultant signal intensity. As shown in Figs. 3.2 to 3.5, the depth dependence seen in the original BP and HBP images has mostly disappeared; basically uniform distribution of signal intensity with depth is obtained by the kinematic BP and HBP methods. The mean values of the signal intensities within the shallowest bins have been increased by 1.48 and 1.47 with the kinematic BP and HBP methods, respectively (Fig. 3.3), compared to the mean values of the original results. These results indicate that the input potency used for generating the synthetic waveforms is backprojected onto the point source without the depth-dependent bias.

3.3.2 Theoretical background of kinematic BP and HBP methods

Here, we consider the theoretical background of the kinematic BP and HBP methods, which successfully suppressed the depth-dependent bias, following the procedure taken in Fukahata *et al.* (2014) with the modified normalizing factors of eqs. (3.13) and (3.14).

In the kinematic BP method as well as in the original BP method, we first assume that the Green's function in eq. (3.6) is an impulsive response function (Fukahata *et al.*, 2014), which can be represented by Dirac's delta function with the amplitude of the first motion of the Green's function as a scale factor on the basis that later phases and inelastic attenuation can be neglected:

$$G_{ij}(t + t_{ij}) \approx g_{ij}\delta(t), \tag{3.15}$$
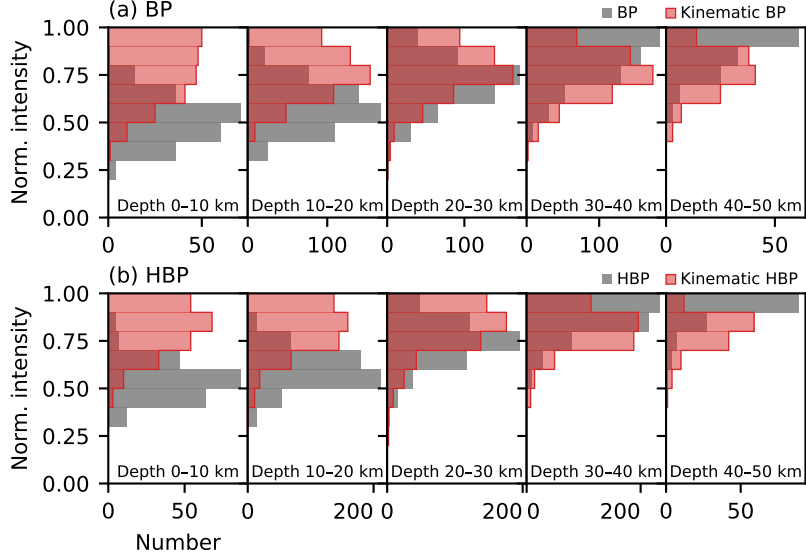
Figure 3.5 Histograms of the normalized intensity of the signals obtained by (a) the original and kinematic BP methods, and (b) the original and kinematic HBP methods.

where g_{ij} is the amplitude of the first motion of the true Green's function, and t_{ij} is the true travel time of the P phase. If we can further assume that the true travel time t_{ij} is approximately equal to the theoretical travel time of t_{ij}^p,

$$t_{ij}^p \approx t_{ij}, \tag{3.16}$$

eq. (3.15) becomes

$$G_{ij}(t + t_{ij}^p) \approx g_{ij}\delta(t). \tag{3.17}$$

Substituting Eq. (3.17) into eq. (3.6), we obtain

$$s_i^{\text{kBP}} = \sum_j \frac{w_j}{A_j} a_i g_{ij}(t). \tag{3.18}$$

If we can compute a Green's function for the P phase that satisfies

$$g_{ij}^p \approx g_{ij}, \tag{3.19}$$

the fraction of the Green's function and the normalizing factor in eq. (3.18) is canceled out in the kinematic BP method because we now have defined the normalizing factor as in eq. (3.13). Hence, the modified signal intensity at the ith source location s_i^{kBP} becomes

$$s_i^{\text{kBP}}(t) \approx a_i(t), \tag{3.20}$$

where we used $\sum_j w_j = 1$. In eq. (3.20) the signal intensity in the kinematic BP method, s_i^{kBP}, directly corresponds to the slip velocity a_i. Which of the Green's function due to unit-step slip velocity or displacement can well satisfy the assumption of eq. (3.17) is hard to be determined (Fukahata *et al.*, 2014), but we note if the effect of the attenuation for the teleseismic body waves can be neglected, the slip motion a_i corresponds to the slip acceleration for the velocity data u_j.

In the kinematic HBP method as well as in the original HBP method, we first assume that the theoretical Green's function is a good approximation of the true Green's function as

$$G_{ij}^p(t) \approx G_{ij}(t). \tag{3.21}$$

Substituting eq. (3.21) into eq. (3.11), we obtain

$$s_i^{\text{kHBP}}(t) \approx \sum_j w_j \frac{\left(\left(a_i * G_{ij}^p \right) \hat{\times} G_{ij}^p \right)(t)}{A_{ij}}. \tag{3.22}$$

If we use the normalizing factor defined by eq. (3.14), the fraction that is composed of the cross-correlation of the Green's functions and the normalizing factor in eq. (3.22) results in the normalized auto-correlation function of the Green's function. Therefore,

if we can assume that the stacked auto-correlation functions is like the Dirac's delta function with certain amplitude (Fukahata *et al.*, 2014), eq. (3.22) becomes

$$\sum_j w_j \frac{\left(G_{ij}^p \hat{\times} G_{ij}^p\right)(t)}{\int_0^T G_{ij}^p{}^2(\tau + t_{ij}^p)d\tau} \approx \delta(t), \tag{3.23}$$

where we used $\sum_j w_j = 1$. Then, the modified signal intensity at the ith source location s_i^{kHBP} is finally expressed as

$$s_i^{\mathrm{kHBP}}(t) \approx a_i(t). \tag{3.24}$$

In eq. (3.24) the signal intensity of the kinematic HBP image, s_i^{kHBP}, directly corresponds to the slip velocity a_i.

3.3.3 Application to the real data

In order to demonstrate how the relative signal intensity is modified by the kinematic BP and HBP methods for the real case, we applied them to the waveforms of the M_{W} 8.3 2015 Illapel, Chile, earthquake with the same procedure adopted by Okuwaki *et al.* (2016), where they used the original HBP method (Fig. 3.6). Here, 4th root stacking (e.g., McFadden *et al.*, 1986) was used to enhance the signal-to-noise ratio of the image, and the data were filtered in the 0.3 to 2.0 Hz frequency band. Compared with the original BP and HBP methods, the signal intensities of the kinematic BP and HBP methods in the region shallower than 25-km depth have been increased by 1.25 and 1.33 of their mean values, respectively (Figs. 3.6c and f), which are similar to the ones for the numerical tests measured within 0 to 25-km-depth bin; 1.28 and 1.31. We note that the mean values of the real applications and the numerical tests may not be simply compared since for the real applications, the mean values were measured among all the point sources in the model fault, while for the numerical tests, we only used the intensities on the input-source points (Fig. 3.1b). Based on the numerical test, we can consider that the depth-dependent bias included in the original BP and HBP method is
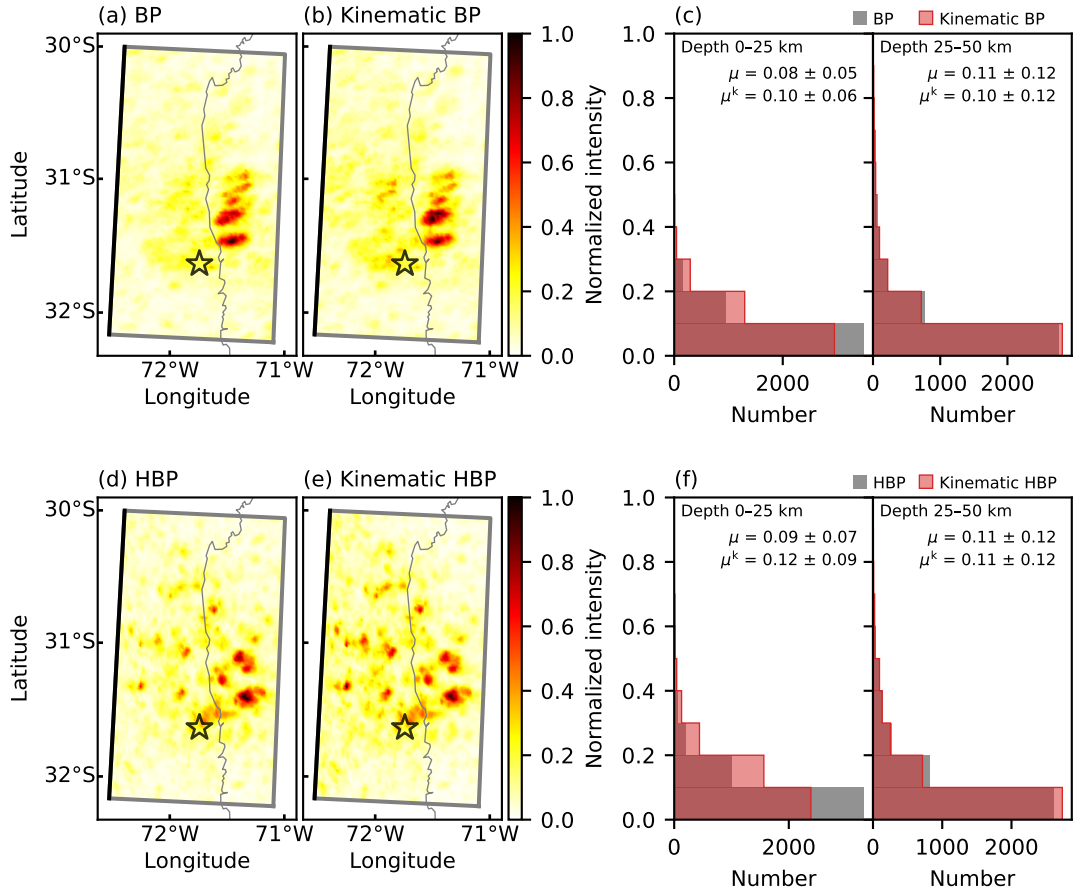
Figure 3.6 Comparison of the real-data application of the original and the kinematic BP and HBP methods for the M_W 8.3 2015 Illapel Chile earthquake. (a, b, d, e) Color represents the normalized intensity of the backprojected signal. The gray rectangle outlines the model fault plane with a dip angle of 15°, the black line on the west side is the up-dip limit of the fault area, and the star denotes the nucleation point (hypocenter). The thin gray curve shows the coastline. (c, f) Histograms of the normalized intensity of the signals obtained by the original and the kinematic BP and HBP methods. μ and μ^k are the mean values of the original and the kinematic BP and HBP signal intensities, respectively.

successfully suppressed by the kinematic BP and HBP methods. The source models of the 2015 Illapel earthquake showed a complex rupture evolution along both the up-dip and down-dip directions (Melgar *et al.*, 2016; An *et al.*, 2017; Yin *et al.*, 2018; Meng *et al.*, 2018), which is more consistent with the image obtained by the kinematic BP and HBP methods. The increased signal in the shallow part should reflect the source of high-frequency radiation from the up-dip rupture propagation. The general difference between the BP and HBP images, especially in the shallow region, reflects the enhancement of the spatial resolution in dip direction of the HBP method by adopting the information of depth phases of the Green's function (Yagi *et al.*, 2012a). While in the region deeper than 25-km depth, the distributions of the signal intensities remain almost the same for the original and kinematic BP and HBP methods (Figs. 3.6c and f). This suggests that the previous discussion of the deep-intense high-frequency radiation, which may result from the rupture of small high-stress patches that accelerate the following large slip (e.g., Okuwaki *et al.*, 2016), should not be affected significantly even by the kinematic BP and HBP methods, at least in the case of the 2015 Illapel earthquake. The real applications suggest that the heterogeneity of the fracture energy or stress drop that perturbs the rupture-front propagation (e.g., Husseini *et al.*, 1975; Fukuyama and Madariaga, 1998) may exist in both shallow and deep part of the fault, though the degree of heterogeneity may be different depending on depth.

4 | General discussion

4.1 | Geometric barrier and rupture evolution

Analytical studies and numerical experiments of rupture propagation have shown that irregular-rupture propagation can enhance high-frequency wave radiations (Das and Aki, 1977; Madariaga, 1977; Bernard and Madariaga, 1984; Spudich and Frazer, 1984). Irregular rupture propagation occurs when rupture front encounters a barrier that stops or slows rupture propagation (Das and Aki, 1977; Aki, 1979). In particular, the role of barriers in the form of geometric discontinuities in fault system has extensively been studied in numerical simulations, suggesting that the geometric barrier contributes to perturbation of rupture evolution (Kase and Day, 2006; Oglesby, 2008; Oglesby and Mai, 2012; Madariaga *et al.*, 2006).

4.1.1 Deceleration and acceleration of rupture front due to geometric barrier

In section 2.1, we showed through the analysis of the 2008 Wenchuan earthquake that the intense high-frequency signals were mainly concentrated around the geometric discontinuities of the fault system; around the XDF cross-cutting the other fault segments, the steps around the northern end of the NPF, and the boundary between the SBF and SCBF segments, which have been recognized as geometric barriers to rupture propagation based on the surface-rupture measurements by pioneering study of the 2008 Wenchuan earthquake (e.g., Fielding *et al.*, 2013). As can be seen from the spatiotemporal evolution of the high-frequency signals (Fig. 2.6a), the high-frequency sources along both the SBF and SPF segments were temporarily arrested around the XDF at 15 s to 25 s from the hypocentral time, and then, further evolved bilaterally into the south-

western and northeastern segments from the XDF. These behavior of the high-frequency signal can be interpreted as deceleration of rupture front when it encountered geometric discontinuity of the XDF, followed by acceleration of rupture front when it came to pass across the XDF and recommenced propagation bilaterally away from the geometric barrier through the adjacent fault segments. The deceleration of rupture front at the XDF inferred from the high-frequency observation is consistent with the independent finding by the inverted slip model, where the deficiency of co-seismic slip or transient suspension of rupture propagation was reported near the XDF at 10 s to 20 s from the hypocentral time (Yagi *et al.*, 2012b). We also note that high-frequency signals of modest intensity at the southwestern ends of the SBF and the SPF during the very early stage of rupture ($\sim$10 s from the hypocentral time) are consistent with the rupture manner inferred from the co-seismic slip model (Hartzell *et al.*, 2013), where they reported southwestward propagation of the co-seismic slip along the Pengguan fault. Thus, we interpret these high-frequency signals to represent stopping phases (Madariaga, 1977) of the initial southward propagation of rupture at the southwestern ends of the SPF and SBF. Bilateral-rupture propagation can also be seen along the SCBF at 50 s to 60 s after the hypocentral time (Fig. 2.6a), and the high-frequency sources observed at the boundaries of the SBF-SCBF and SCBF-NCBF and the northwestern edge of the NPF (Fig. 2.6a) can also be interpreted as the stopping phases or abrupt rupture decelerations.

4.1.2 Complementarity of high- and low-frequency radiations

If we consider the distribution of the maximum, median, and mean values of high- and low-frequency signal intensities along the dip directions of the fault segments (Fig. 4.1), we see that the distributions of sources of high- and low-frequency waves are roughly complementary in the southwestern segments (SBF, SCBF, SPF, and NPF); these distributions are consistent with the underlying theoretical framework, which predicts that propagation of a rupture front at constant speed does not contribute to high-frequency radiations (Spudich and Frazer, 1984). The complementary relationship between the
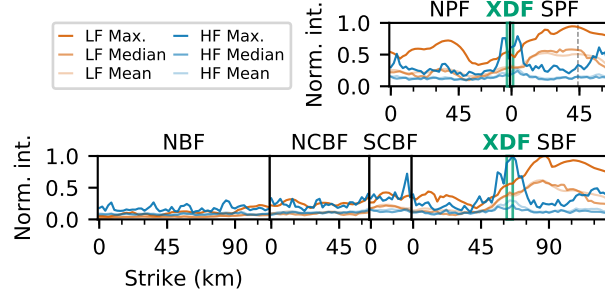
Figure 4.1 Distributions of maximum, median, and mean values of signal intensity along the dip direction of each fault segment (see Fig. 2.2a caption for fault segment names). The abscissae give distances along strike from the left-bottom corner of each fault segment, and the ordinate is a normalized signal intensity. Cold and warm colors represent the high- and low-frequency (HF and LF) results, respectively. The estimated locations of the XDF (green lines) and the location of the hypocenter (gray dotted line) are also shown.

high-frequency sources and the large slip area has generally been reported by the previous studies (Meng *et al.*, 2012a; Uchide *et al.*, 2013; Okuwaki *et al.*, 2014; Grandin *et al.*, 2015; Yagi and Okuwaki, 2015; Okuwaki *et al.*, 2016). We infer that the high-frequency sources should be correspond to the areas where the rupture-front propagation is disturbed by the geometric discontinuities within or between the fault segments, while the low-frequency sources should be corresponding to the region where the smooth and persistent rupture propagation is going along the continuous and linear section of fault segments. A seismic source model for the M_W 7.2 2010 El Mayor-Cucapah earthquake (Uchide *et al.*, 2013) shares general similarity to our result, which also reported the intense high-frequency radiation was observed near the boundaries of fault segments, which can be interpreted as the geometric barriers. While in the northeastern segments (NCBF and NBF) in Fig. 4.1, the relative intensities of high- and low-frequency signals are almost identical, and this may result from either the cases of that the signal intensity for both the high- and low-frequency waves are inherently weak compared to the ones in the southwestern segments, or that the intensities of both the HF and LF waves in the northeastern segments may be contaminated and weaken by the later phases of the main rupture along the southwestern segments. These effects may also explain the

lack of the high-frequency radiation around the boundary between the NCBF and NBF, even though the geometric discontinuity is recognized in the surface ruptures and some amounts of slip are observed in the waveform inversion (e.g., Yagi *et al.*, 2012b).

4.1.3 Difference in rupture irregularity for inland and subduction zone earthquakes

While for the subduction zone earthquakes where there is no such geometrical discontinuities are recognized, the high-frequency wave radiations have been observed at the edges of the large asperity ruptures with the same approach adopted in this study together with the waveform inversion (Okuwaki *et al.*, 2014, 2016), and they interpret that the heterogeneous distribution of the fracture energy or stress drop could be the sources of high-frequency wave radiation where rupture accelerates and triggers the following smooth large slip, which are consistent with the cascading rupture model (Ide and Aochi, 2005). The above descriptions of the rupturing manner for the subduction zone earthquakes, that are observable through the analyses of the high-frequency wave radiation, are not exactly the same as what we here observed in the 2008 Wenchuan earthquake, where the significant geometrical discontinuities exist in the fault system. Our observation could imply that, when the fault system involves the geometric barriers, the observable rupturing manner captured via the teleseismic high-frequency waveforms would be more complex than that for the subduction zone earthquakes in the sense that the high-frequency wave radiation could be observed as a result from the abrupt deceleration or stopping of rupture propagation, or even acceleration of rupture to go through the adjacent-fault segment.

4.1.4 Scattering of rake angles and stress perturbation due to geometric barrier

As shown in Figure 2.5a, the resulting rake angles for the high-frequency model exhibit more scattered behavior than those for the low-frequency model (Fig. 2.5b). Numerical

experiments with non-uniform frictional fault that involves the high strength locations (barriers) retrieve the irregular distribution of the rupture front, resulting heterogeneous distribution of final slip vectors (Mikumo and Miyatake, 1978). The dynamic rupture modeling, assuming the slip weakening law and isotropic friction, has also shown that the rake rotation can be occurred under the condition of low initial shear stress level with spatially variable direction of stress (Guatteri and Spudich, 1998). If we consider the geometric barriers, recognized as the XDF and the steps between the fault segment, as the high strength areas where the shear stress direction is locally changed, the scattering or rotation of rake-angle can be interpreted as a result of higher stress drop than the initial stress level or perturbations of stress at the barriers, and may also be consistent with the field observations of fault exposures showing the intermixed distribution of the vertical and horizontal offsets, especially at around the XDF (Xu *et al.*, 2009a; Yu *et al.*, 2010). However, there is also a possibility that the HBP method does not have enough ability to constrain rake angles from intensity of signals. Since the high-frequency waves contain more complex and scattered phases than those of the low-frequency waveforms, the slight changes of waveform amplitude responsible for the rake variations may be buried or not resolved with the HBP method. For example, even if we fix the rake angle of pre-calculated Green's function as 90° for all the source node, we get the similar result as the ones allowing rake variability of Green's functions for the high-frequency analysis (Fig. 4.2). This instability raised from the high degree of freedom of the rake angle may explain the ghost image of the high-frequency signals shown at -200 km from the epicenter at 30 to 50 s after the origin time shown in Fig. 2.6a. In contrast, the rake angles for the low-frequency model shows smoother distribution than those for the high-frequency model, generally showing reverse faulting at around the hypocenter and the middle parts of the SPF and the southern parts of the SBF, while horizontal slip at around the XDF for both the SPF and the SBF, which are consistent with the seismic source model by using the low-frequency waveforms (Yagi *et al.*, 2012b; Hartzell *et al.*, 2013).

Note that we only draw the representative rake angle for each source node with max-
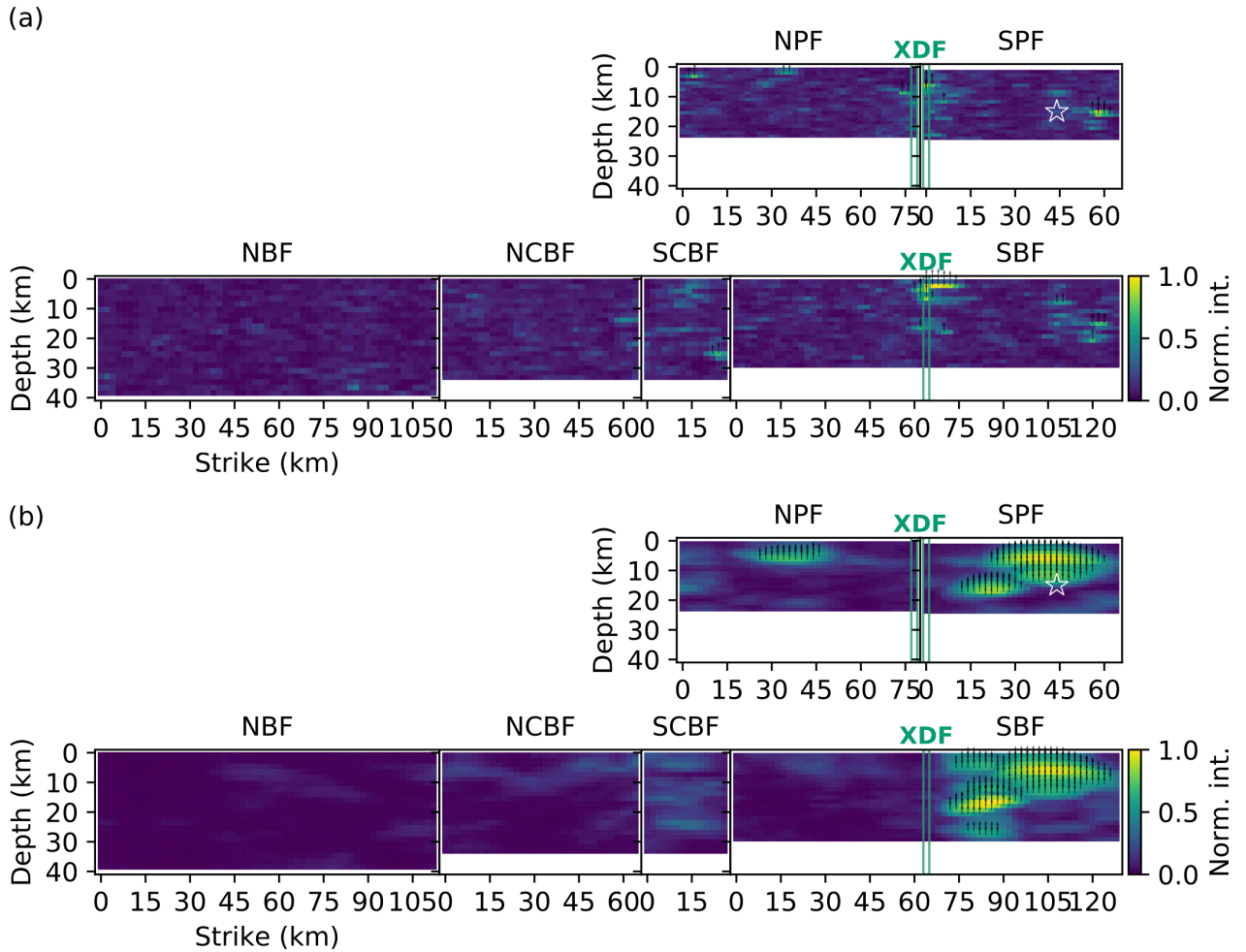
Figure 4.2 Alternative results with fixed rake angle at 90°. (a) Spatial distribution of high-frequency sources in a strike vs. depth view. Rake angle in Green's function is fixed at 90° for all the source nodes. Background colors represent normalized signal intensities. Arrows show rake angles, which for clarity are shown only on source cells for which signal intensities are greater than 0.5. Green lines indicate the estimated location of the XDF and the star marks the hypocenter. See caption of Fig. 2.5a for fault segment names. (b) Same as Fig. 4.2a, but for the low-frequency result.
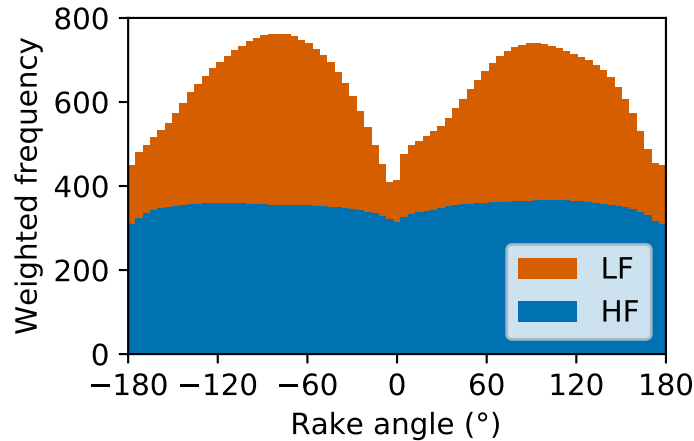
Figure 4.3 Histogram of rake angles weighted by signal intensity. The figure shows the histogram of full range of rake angles between -180° and 180° with an increment of 5°. Note that the bin-count of each rake angle is weighted by its signal intensity. Blue and orange bars are the high- and low-frequency (HF and LF) results, respectively.

imum signal intensity along the set of rake angles used for calculation of the Green's functions for the visibility of Figure 2.5, and we constrain the range of variability of the rake angle (0° to 180°) according to the field observations (Xu *et al.*, 2009a; Yu *et al.*, 2010). However, histograms of the full range of rake angles (-180° to 180°) weighted according to single intensity show symmetric distributions with twin peaks at about -90° and 90° for both high- and low-frequency analyses (Fig. 4.3). Even if we searched the best rake angle for each source node according the maximum intensity along all the set of rake angles, it was difficult to distinguish a unique rake angle (e.g., 120° or -60°) in our methodology, because the polarity of the *P*-phase in the Green's function can be flipped by 180° by phase shifts when we use a narrow low-frequency bandpass filter. However, constraining the range of rake angles on the basis of the field observations allowed us to estimate the reliable rake angles that are comparable to those obtained by inversion modeling by using low-frequency waveforms.

4.1.5 Geometric barrier: a proxy for future earthquake hazard

Irregularity of rupture propagation is significant for earthquakes in fault systems that include geometric barriers. Such a rupture behavior, which was captured through the analysis of the teleseismic high-frequency waveforms and discussed in this study, may only be valid in a certain length scale around 10^0 to 10^1 km. However in finer scale, fault roughness (topographic variations of the fault surface) also generates high-frequency radiation, as quantitatively shown by dynamic rupture simulations (e.g., Dunham et $al.$, 2011; Shi and Day, 2013; Bruhat et $al.$, 2016; Mai et $al.$, 2017), and the roughness-induced irregularity of rupture propagation also plays a key role in high-frequency wave radiation, although it is difficult to consider the stochastic nature of the fault surface in this study due to the limited spatial resolution of the HBP method.

4.2 | Inhomogeneous barrier and rupture evolution

4.2.1 Zigzagging rupture episodes

The seismic source model of the M_W 8.3 Illapel, Chile, earthquake, which integrates the inverted slip together with the high-frequency sources, shows that the rupture process involves two distinct episodes of rupture propagation, which can be divided into the first 25 s from the hypocentral time and the following ruptures. In the first sequence (0 s to 25 s), rupture mainly propagates up-dip to the northwest of the epicenter at the rupture-front velocity less than 2 km/s, and temporarily terminates at about 16 km northwest of the epicenter. High-frequency sources generally follow the rupture front edges but are distributed mainly at the deeper parts of the slip. During the second sequence (25 s to 90 s), rupture starts propagating up-dip from the down-dip part of the fault plane, after the excitation of the relatively strong high-frequency radiation at around 27 s. This burst of the high-frequency signals, shown in the panel of 26 s to 30 s in Fig. 2.17, is consistent with the rise of the moment rate function at around 25 s (Fig. 2.8). The propagation speed of rupture-front varies along the strike and dip directions.

The rupture speed along the strike direction (Fig. 2.18a) is estimated to be less than 2 km/s, which is the same as in the first rupture sequence, but the rupture velocity along the dip direction is relatively fast, exceeding 3 km/s (Fig. 2.18b).

4.2.2 High-frequency radiation triggers the secondary rupture episode

The switch from the first to the second rupture episodes is marked by the strong high-frequency radiation at the down-dip edge of the slip area below the coast. Theoretical studies show that high-frequency waves are generated by abrupt changes in rupture velocity and/or slip-rate (e.g., Madariaga, 1977; Bernard and Madariaga, 1984; Spudich and Frazer, 1984), and Spudich and Frazer (1984) concluded that it is difficult to distinguish which factor, discontinuity in rupture velocity or slip-rate, could be the main generator of high-frequency waves. Ohnaka and Yamashita (1989) also shows that slip-rate increases as the rupture velocity accelerates and diverges if the rupture velocity equals to shear wave velocity for the anti-plane crack, and Rayleigh wave velocity for the in-plane crack. Although we cannot see a clear propagation path from the first to the second rupture episode, the strong high-frequency radiation at the down-dip edge of the slip area may reflect the acceleration of the slip-rate or rupture velocity that could have triggered the second rupture sequence that produced the large slip. Such an interaction between the preceding strong high-frequency radiation and the following large-asperity rupture is also observed during the M_W 8.8 2010 Maule, Chile, earthquake (Okuwaki et al., 2014).

4.2.3 Depth dependence of high-frequency radiation

In both the rupture episodes during the 2015 Illapel earthquake, high-frequency sources tend to be distributed at deeper part of the slip distribution, and the strength of high-frequency sources is relatively weak in areas of ongoing large slip. The similar, spatial relationship between high-frequency sources and the large-inverted slip has been documented during the M_W 8.8 2010 Maule, Chile, earthquake (Okuwaki et al., 2014) using the same methodology as this study, as well as for the 2015 Illapel earthquake (Ye et al.,

2016a; Melgar *et al.*, 2016), and other subduction-zone megathrust earthquakes (e.g., Koper *et al.*, 2012; Lay *et al.*, 2012). Theoretical studies suggest that spatial heterogeneity of fracture energy or stress drop induces discontinuities in rupture propagation (e.g., Husseini *et al.*, 1975; Fukuyama and Madariaga, 1998), which in turn generates high-frequency waves (e.g., Spudich and Frazer, 1984). Hence our source model may reflect the heterogeneous distribution of fracture energy or stress drop along the fault. However, the observations, which apparently show the depth dependence of the high-frequency radiation, may not fully be consistent with the theoretical mechanism of the high-frequency radiation because, especially for the 2015 Illapel earthquake, we observed the rupture-front migration in both up- and down-dip directions, which should have the fluctuations of rupture propagation when the rupture direction switches to one another, but showed generally weak intensity of high-frequency signal in the shallow part of the model fault. We will discuss this intriguing discrepancy between the observation and theoretical knowledge in Chapter 4.3 from the viewpoint of the biasing effect of the BP methods.

4.2.4 Confirmation of rupture episodes by strong motion records

The two rupture episodes observed from our analyses of teleseismic records are also confirmed by the strong motion record at CO03 station, located at 134 km northeast of the epicenter (Fig. 4.4). The strong motion record indicates the modest amplitude of waves at the first rupture episode continuing about 15 s from the onset of the first P-phase, and then the large amplitude follows during the second rupture episode. Similar observation of the initial rupture phase followed by the intense secondary rupture event can be recognized during the 2014 Iquique, Chile, earthquake (Yagi *et al.*, 2014; Ruiz *et al.*, 2014), although the clear intense foreshock activity, which is the remarkable feature of the 2014 Iquique earthquake, has not been reported for the 2015 Illapel earthquake.
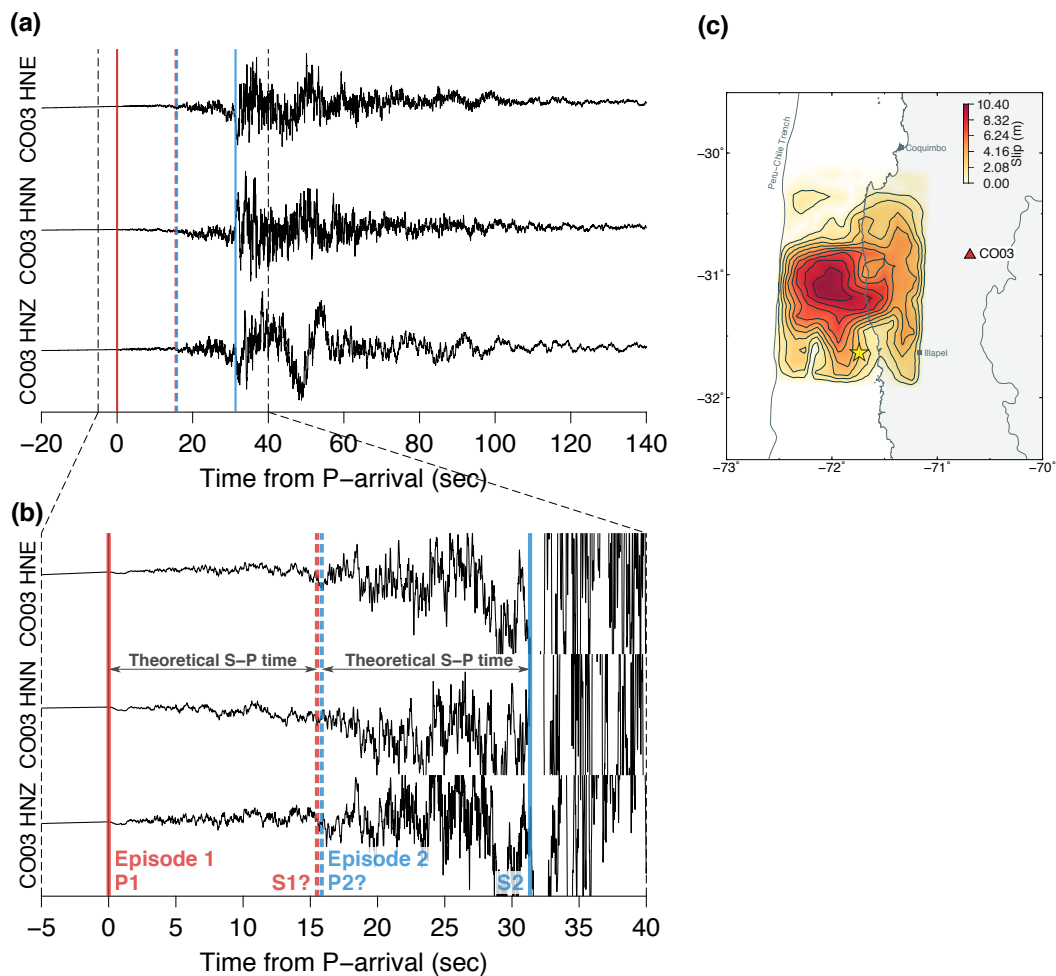
Figure 4.4 (a) Three components (east-west, north-south, and vertical from top to bottom) of unfiltered trace of velocity waveform at CO03 station (c) from the network of C1 operated by Red Sismologica Nacional, Universidad de Chile. Each trace is normalized by its absolute maximum amplitude. (b) The enlarged view of the upper panel. P1 and S2 indicate the onsets of P-phase and S-phase, which are manually picked. S1? and P2? are expected onset of S and P phase related to the P1 and S2 phases, respectively. Theoretical S-P time at CO03 station is calculated by using TauP (Crotwell *et al.*, 1999) based on ak135 model (Kennett *et al.*, 1995).

73

4.2.5 Gradual termination of rupture: Role of inhomogeneous barrier

Other prominent feature of our integrated source model can be highlighted at the termination of the second rupture episode (60 s to 90 s), where slip-rate gently declines from about 60 s, and high-frequency sources are almost absent. This tendency is contrary to what is observed during the 2015 Gorkha, Nepal, earthquake (Yagi and Okuwaki, 2015), where the rupture-front velocity abruptly decelerates and the strong high-frequency radiation is observed at the end of the rupture sequence, which can be interpreted as stopping phase (e.g., Madariaga, 1977). The northern end of the 2015 Illapel source region coincides with the transition zone between high- and low- coupled region (Moreno et al., 2010; Métois et al., 2013) based on the GPS observation and also coincides with the southern end of the northern part of the 1997–1998 swarm area (Lemoine et al., 2001; Pardo et al., 2002, Fig. 2.8). Holtkamp and Brudzinski (2014) discusses that the rupture of the large and mega earthquakes in subduction zone worldwide often terminates around the region where the active earthquake swarm is observed, and the collocation of this may be explained by the spatial change of stress regime, and the swarm activity may act as a proxy for the segmentation of the megathrust rupture. The weak excitation of high-frequency radiation at the northern end of rupture observed in our analyses of the 2015 Illapel earthquake may reflect gradual rupture deceleration (e.g., Spudich and Frazer, 1984), and this gradual-rupture-stopping behavior might suggest that the rupture front penetrates into the swarm-dominated region, where the significant change in frictional property or stress state may exist (e.g., Kaneko et al., 2010). As discussed in Meng et al. (2018), the intense earthquake swarm and the repeating earthquakes have been observed in and around the source region of the 2015 Illapel earthquake (Nishikawa and Ide, 2017; Huang et al., 2017, Fig. 4.5), suggesting that the source region is wrapped by the aseismic region, which may work as the inhomogeneous barrier against the rupture-front propagation. Independently, the GPS observations resolved the low-coupling area around the source region (Métois et al., 2016), which may also regarded as another proxy for the aseismic-transient zone that refused the further penetration of rupture front or intense generation of high-frequency radiation. However, we should note that the discus-
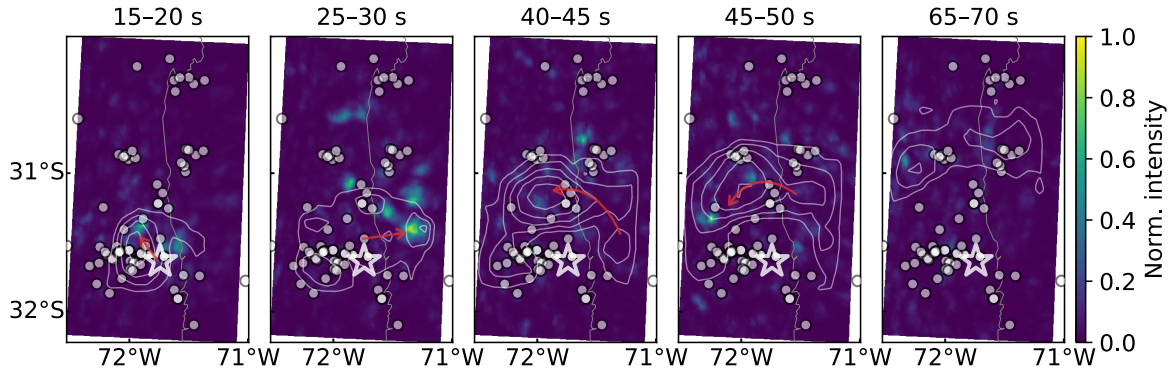
Figure 4.5 Snapshots selected from Fig. 2.17. White dots are the earthquake swarms detected by Nishikawa and Ide (2017). Arrow indicates the estimated rupturing path based on the high-frequency source location.

sion of the relative intensity of high-frequency signal resolved in the HBP method should carefully be done. As can be seen in the sensitivity test for the HBP method (Fig. 2.11), the strength of response from the multiple synthetic point sources at the shallower part of the fault is, in general, at most 30 to 40% weaker than that at the deeper part. This tendency of lacking the intense high-frequency signal at the shallow part of the model fault is the depth-dependent artifact of the HBP image, which is further discussed in the Chapter 3 in this thesis. Even considered this imaging-artifact in the synthetic test, the strength of the observed signals at around the terminus of the second rupture episode (60 s to 90 s) is still weaker than that of the strong high-frequency signals observed at the initiation of the second rupture episode at the down-dip edge of the slip, and this artifact does not significantly affect the validity of the discussion.

4.2.6 Background seismicity and rupture evolution

Slip distribution inferred from the waveform inversion analysis correlates well with the highly locked region in the plate-coupling models by Moreno *et al.* (2010) and Métois *et al.* (2013). The locations of the 1997–1998 swarms coincide with the northern and north-eastern edges of the slip area (Fig. 2.8), and for at least 5 years before the 2015 Illapel earthquake, seismicity around and south of the epicenter (from the CSN earthquake catalog) was more active than in the rest of the source region (Fig. 4.6).

These pre-seismic activities outline the source region of the 2015 Illapel earthquake and may have had a role in determining the area favorable to rupture. However, the slip deficit amounts to 5.3 m if assuming 100% coupled from the 1943 earthquake, while the maximum inverted slip is much larger than 5.3 m (Fig. 2.8). Although the peak slip amplitude is slightly fluctuated by the assumption of the maximum rupture velocity (Fig. 2.14), the slip deficit is still much less than the amount of inverted slip. We believe that the slip deficit since the 1943 earthquake is not enough for the occurrence of the 2015 event, and some amounts of slip deficit further before the 1943 earthquake should be necessary. Moreover, the field surveys of affected tsunami have suggested that there are spatial differences between tsunami inundation areas along the coast between the 1943 and the 2015 Illapel earthquakes (Aránguiz *et al.*, 2016). Thus, the 2015 Illapel earthquake is not likely a simple re-occurrence of the 1943 earthquake.

4.2.7 Rupture process controls tsunami generation

According to the post tsunami surveys, the tsunami arrival time at the Totoral village, near the northern edge of the slip area (Fig. 2.8) where the maximum tsunami inundation height reached 10.8 m, was 6 to 10 minutes. This arrival time is shorter than for other tsunamigenic earthquakes in the Chilean subduction zone (Aránguiz *et al.*, 2016). Numerical tsunami simulation suggests that this rapid tsunami propagation can be explained if the large slip patch is close to the coastline and a narrow continental shelf and steep bathymetry are present (Aránguiz *et al.*, 2016). Although the rupture front reaches the shallowest part near the trench in our source model (Fig. 2.17), the area of large slip concentrates at about 15 to 20 km depth on the fault plane close to the coast (Fig. 2.8). The occurrence of large slip near the coast in the second rupture episode may account for the shorter arrival time and large run-ups of tsunami near the northern edge of the source region.
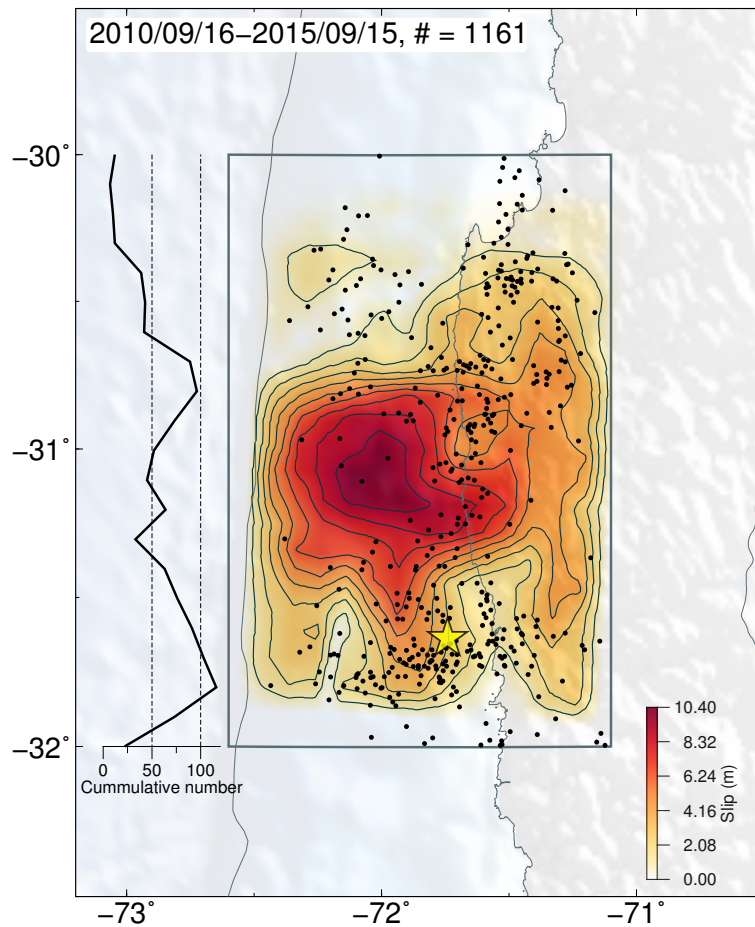
Figure 4.6 Comparison between the total slip distribution and the seismicity in 5 years before the 2015 Illapel earthquake. The contour outlines the slip every 1.04 m. Black dots correspond to the epicenters determined by the Centro Sismológico Nacional, Universidad de Chile (CSN: http://www.sismologia.cl, last accessed on 16 November 2015). Inset graph shows the cumulative number of the earthquakes (total 1161 events) counted by 0.1° sliding window along Latitude, with the criteria of M ≥ 3, shallower than 50 km depth, date 2010/09/16–2015/09/15, -32° ≤ Latitude ≤ -30° and -72.6° ≤ Longitude ≤ -71.1° (area within the rectangle). Star denotes the epicenter determined by the CSN. Background topography and bathymetry are from ETOPO1 (Amante and Eakins, 2009)

4.3 | Uncertainty in backprojection

4.3.1 Inherent depth dependence of backprojection

In Chapter 3.3.1, we proposed the variants of the BP and HBP methods in order to directly retrieve the slip motion from the backprojected images by modifying the normalizing factors adopted in the original BP and HBP methods, which successfully removes the depth-dependent bias in the original BP and HBP methods. However, the depth dependence of the signal intensity in the original BP and HBP images for megathrust earthquakes in subduction zone is still crucial information for assessing future-earthquake damage due to strong shaking, considering the resonant frequencies of the buildings that lie in the frequency band adopted for the BP analyses (e.g., Snieder and Şafak, 2006; Meng *et al.*, 2012a). The relative intensity of high-frequency wave radiation by a unit slip in the deeper part of the seismogenic zone tends to be stronger than that of the radiation in the shallower part of the fault, provided that a fault is dipping and the rigidity of the medium increases with depth.

4.3.2 Further uncertainty in backprojection image

As shown in Section 4.3.4, both mathematical representations and numerical test indicate that the signal intensity of the original BP and HBP images does not directly related to the slip amplitude. We verified through the numerical tests that the kinematic BP and HBP methods were well utilized for removing depth dependence of the signal intensity and extracting slip motion on a fault, which should be useful for unbiased discussion of high-frequency radiation during an earthquake rupture by using the BP techniques in the context of the source-rupture evolution, with the direct comparison with the inverted slip distribution. However, as can be seen in the numerical test, even if the kinematic BP and HBP methods are used, in the ideal model setting to generate the synthetic waveforms, the input sources were still imperfectly recovered, and the normalized intensity of the backprojected signal ranged from about 0.5 to 1.0 (Figs. 3.3 and 3.5). This spread in the distribution of signal intensity can be explained due to the noise given in the

second terms in eqs. (3.4) and (3.9). We assumed for both the original and kinematic BP and HBP methods that the noise terms can be suppressed by stacking as shown in eqs. (3.5) and (3.10) based on Fukahata *et al.* (2014). However, in our numerical test, where we assumed the multiple-point sources with a uniform slip-rate function (Fig. 3.1), the interference of the noise and signal terms cannot be neglected when the sources are close to each other because the convolution functions of the slip velocity and the Green's function get similar among the neighboring locations. As a result, the signal intensity may be either intensified or weakened by the noise, and the signal intensity at the specific source point may not exactly represent the slip amplitude. This imperfect recovery of the input sources is a common feature in both the original and kinematic BP and HBP methods, irrespective of the implementation of the normalizing factor, because this comes from the resemblance of the Green's function at sources (Fukahata *et al.*, 2014). We also have to mention that the assumptions we made in eqs. (3.19) and (3.21) may not work efficiently for the analysis of real data, because of the limitation to calculate the Green's function accurately (e.g., Yagi and Fukahata, 2011a), and the uncertainty of the depth and focal mechanism of the source may distort the kinematic BP and HBP images for real applications.

4.3.3 Revisiting complementarity of high- and low-frequency radiations

It is a general agreement that the low-frequency backprojection image becomes blurry compared to the one using the high-frequency data (e.g., Satriano *et al.*, 2012; Fan and Shearer, 2015). As we discussed above, incoherence of the slip motion a_i and the ones from the other sources $a_{i'}$ as well as dissimilarity among the Green's functions (G_{ij} and $G_{i'j}$) are necessary conditions for the BP and HBP methods to well extract the signal terms from eqs. (3.4) and (3.9), by suppressing the noise terms. In other words, the resolvability of the signal at the specific location is controlled by similarity of the convolution functions of the slip velocity and the Green's function between the neighboring locations. Such a similarity length is broaden in space and time when the low-frequency bandpass filter is applied to the data, compared to that filtered in high

frequency range. As a result, we obtain the blurred, low-frequency backprojection image.

As discussed in Section 4.1.2, another notable observation of the backprojection study is that the spatiotemporal location of the intense high-frequency source is shifted from the center of the low-frequency source to the edge of it (e.g., Kiser *et al.*, 2011; Okuwaki and Yagi, 2018). The similarity length for the high-frequency data is expected to be shorter than that for the low-frequency data. Thus, the small-scale change of slip behaviour is preferable to be resolved for the high-frequency backprojection. While the similarity length is extended by using the low-frequency filter and the coherent slip motion during the smooth asperity rupture can be emphasized by the low-frequency backprojection. As a result, the high-frequency signal of the backprojection is located at the edge of the low-frequency signal, which should also be a basis that explains the relationship between the intense high-frequency BP signals and the large-inverted slip distribution (e.g., Uchide *et al.*, 2013). Thus, the concept of the similarities of the slip motion and the Green's function, that explains the imperfect recovery of the signal in the numerical test, may also provide a clue to explain the frequency dependence of the backprojection image, which highlights the difference of the slip behaviour.

4.3.4 Non-linearity between the backprojected signal and slip motion of the original BP/HBP images

Through section , we argued the cause of depth dependence of the signal intensity in the original BP and HBP images by only considering the scaling factors involving the Green's functions in the numerators of the signal terms in eqs. (3.4) and (3.9). The normalizing factors adopted in the original BP and HBP methods, however, also contain the term of slip motion a_i since the normalizing factors are composed of the waveform u_j (eq. 3.3). For example, eq. (3.6) can be represented in an exact form by substituting eq. (3.3) as

$$s_i^{\mathrm{BP}}(t) \approx \sum_j w_j \frac{(a_i * G_{ij})\left(t + t_{ij}^p\right)}{\mathrm{pol}(u_j) \cdot \sqrt{\int_0^T \left[\sum_{i'} (a_{i'} * G_{i'j})(\tau + t_j^p)\right]^2 d\tau}}, \qquad (4.1)$$

for the original BP method, where a_i is included in both the numerator and denominator. Therefore in the original BP and HBP method, the relationship between the resultant signal intensity and the slip motion a_i is basically non-linear, which makes it difficult to clarify the effect of the Green's function on the depth dependence of the signal intensity. While in the kinematic BP and HBP methods, the normalizing factors are designed to solely include the Green's function. This feature in the formulations of the kinematic BP and HBP methods, directly relating the signal intensity to the slip motion, establishes a linear connection between the signal intensity and the slip motion.

4.3.5 A gap between mathematical expression and resultant image of kinematic BP and HBP methods

In the mathematical expressions, the signal intensity of the kinematic BP and HBP methods corresponds to the slip velocity or slip acceleration, but as discussed above, the noise term, which is a contribution from the neighboring source locations, is not negligible, and the signal at a certain location could work as the noise to other sources. Thus, the signal intensity at the specific source point does not exactly represent the slip. In the sense we should consider that the signal contains contributions from the nearby sources with a certain extent, which determines the spatial resolution of the backprojected image (Fukahata *et al.*, 2014), the image obtained by the kinematic BP and HBP methods may represent the potency distribution. Specifically, the signal intensity is related to the potency density tensor (Ampuero and Dahlen, 2005) of the specific components, since we fixed the fault geometry and the slip direction when calculating the theoretical Green's function in the numerical tests and the real application.

5 | Conclusions

In this thesis, we considered the deterministic relationship between the irregularity of earthquake-rupture evolution and the geometric and inhomogeneous barriers along the fault, though the analyses of the 2008 Wenchuan, China, and the 2015 Illapel, Chile, earthquakes by using the globally observed, high-frequency teleseismic waveforms in Chapter 2. We found that the geometric barrier played a role on deceleration and acceleration of rupture-front propagation, which may reflect the stress concentration and following triggering of rupture across the barriers during the 2008 Wenchuan earthquake. While in the 2015 Illapel earthquake, we found that the rupture front avoided the inhomogeneous barrier (intense swarm region), resulting in zigzagging, irregular rupturing paths. We also found that the rupture gradually decelerated and terminated with the weak excitation of high-frequency radiation, reflecting the gradual change of frictional property or stress state along the fault, which is dissimilar manner to the one with the geometric barrier. Our observations of high-frequency radiations highlight the critical role of the barriers as the extrinsic factor that controls the irregularity of rupture evolution.

We also considered the theoretical background of the BP methods in Chapter 3. Through the mathematical reviews and numerical tests of the time-domain BP and HBP methods, we confirmed that the signal intensity in the original BP and HBP methods was designed to retrieve the relative strength of wave radiation. Therefore, the signal intensity is proportional to the amplitude of the Green's function, which leads to clear depth dependence of the signal intensity. In other words, the original BP and HBP images involve a bias when the images are interpreted as rupture property along the fault, which are not directly comparable to the inverted slip distribution. The kinematic BP

and HBP methods, newly proposed in this thesis, can directly relate the signal intensity to the slip motion on a fault surface, which is free from the depth-dependent bias. The proposed methods are useful for quantifying the depth dependence of the high-frequency sources, which would deepen our understanding of the high-frequency radiation and its role on the rupture property during an earthquake.

Acknowledgements

My sincere and primary gratitude goes to my supervisor, Yuji Yagi (Yagi-san). This dissertation would not have been possible without his patient, enthusiastic, continuous, and tremendous supports and encouragements. I enjoyed whole research with him. I remember every discussion with him over the *fresh* source model of the large/great earthquake (2014 Iquique, 2015 Gorkha, 2015 Illapel, 2016 Kumamoto, 2016 Amatrice, 2017 Chiapas, 2018 Hokkaido, 2018 Sulawesi, and so on...) occurred during my PhD. Whenever I brought him a new result, he always showed me an excellent, simple, cool ways of explanation of the complex earthquake physics, clearing up my confusing, chaos mind. Through the entire research experience with him, I learned a lot from him, which enough motivated me to be a scientist. I would also like to say a huge thank you for Teruyuki Maruoka (Maru-san), my supervisor for my undergraduate class. For me, he is an archetype of scientist whom I want to be. I've always seen him a coolness of being scientist, whenever I chatted with him, over beers, mostly. I greatly appreciate Ken-ichiro Hisada, Shigehiro Fujino, and Yukitoshi Fukahata for their examination of this dissertation. I deeply thank faculty staffs for supporting the whole research; Yoko Yasuda, Mutsuko Kuwahara, and especially, Harumi Tobita. Sincere gratitude also goes for the professors and researchers in the faculty; Katuso Sashida, Sachiko Agematsu, Yoshihito Kamata, Kohtaro Ujiie, Naoki Nishiyama, Yoji Arakawa, Toshihiro Tsunogae, Kei Ikehata, Masanori Kurosawa, Atsushi Kyono, Kenichiro Hayashi, Kosei Komuro, Naoki Kohno, Yasunari Shigeta, and Yukiyasu Tsutsumi. Finally, I thank my family who encouraged me to do science.

References

Akaike, H., 1980. Likelihood and the Bayes procedure, *Trab. Estad. Y Investig. Oper.*, **31**(1), 143–166, doi:10.1007/BF02888350.

Aki, K., 1979. Characterization of barriers on an earthquake fault, *J. Geophys. Res.*, **84**(B11), 6140, doi:10.1029/JB084iB11p06140.

Aki, K. and Richards, P. G., 2002. *Quantitative seismology*.

Allmann, B. P. and Shearer, P. M., 2007. A High-Frequency Secondary Event During the 2004 Parkfield Earthquake, *Science*, **318**(5854), 1279–1283, doi:10.1126/science.1146537.

Amante, C. and Eakins, B. W., 2009. ETOPO1 1 arc-munite global relief model: Precedures, data sources and analysis. NOAA Technical Memorandum NESDIS NGDC-24, *Mar. Geol.*, (March), 19, doi:10.7289/V5C8276M.

Ampuero, J.-P. and Dahlen, F. A., 2005. Ambiguity of the moment tensor, *Bull. Seismol. Soc. Am.*, **95**(2), 390, doi:10.1785/0120040103.

An, C., Yue, H., Sun, J., Meng, L., and Báez, J. C., 2017. The 2015 Mw 8.3 Illapel, Chile, Earthquake: Direction-Reversed Along-Dip Rupture with Localized Water Reverberation, *Bull. Seismol. Soc. Am.*, **107**(5), 2416–2426, doi:10.1785/0120160393.

Aránguiz, R., González, G., González, J., Catalán, P. A., Cienfuegos, R., Yagi, Y., Okuwaki, R., Urra, L., Contreras, K., Del Rio, I., and Rojas, C., 2016. The 16 September 2015 Chile Tsunami from the Post-Tsunami Survey and Numerical Modeling Perspectives, *Pure Appl. Geophys.*, **173**(2), 333–348, doi:10.1007/s00024-015-1225-4.

Beck, S., Barrientos, S., Kausel, E., and Reyes, M., 1998. Source characteristics of historic earthquakes along the central Chile subduction zone, *J. South Am. Earth Sci.*, **11**(2), 115–129, doi:10.1016/S0895-9811(98)00005-4.

Beresnev, I. A., 2003. Uncertainties in Finite-Fault Slip Inversions: To What Extent to Believe? (A Critical Review), *Bull. Seism. Soc. Am.*, **93**(6), 2445–2458.

Beresnev, I. A., 2017. Factors controlling high-frequency radiation from extended ruptures, *J. Seismol.*, **21**(5), 1277–1284, doi:10.1007/s10950-017-9660-6.

Bernard, P. and Madariaga, R., 1984. A new asymptotic method for the modeling of near-field accelerograms, *Bull. Seismol. Soc. Am.*, **74**(2), 539–557.

Beroza, G. and Spudich, P., 1988. Linearized inversion for fault rupture behavior: Application to the 1984 Morgan Hill, California, earthquake, *J. Geophys. Res.*, **93**(B6), 6275–6296.

Bruhat, L., Fang, Z., and Dunham, E. M., 2016. Rupture complexity and the supershear transition on rough faults, *J. Geophys. Res. Solid Earth*, **121**(1), 210–224, doi:10.1002/2015JB012512.

Burchfiel, B., Royden, L., van der Hilst, R., Hager, B., Chen, Z., King, R., Li, C., Lü, J., Yao, H., and Kirby, E., 2008. A geological and geophysical context for the Wenchuan earthquake of 12 May 2008, Sichuan, People's Republic of China, *GSA Today*, **18**(7), 4, doi:10.1130/GSATG18A.1.

Clinton, J. F., 2006. The Observed Wander of the Natural Frequencies in a Structure, *Bull. Seismol. Soc. Am.*, **96**(1), 237–257, doi:10.1785/0120050052.

Contreras-Reyes, E., Becerra, J., Kopp, H., Reichert, C., and Díaz-Naveas, J., 2014. Seismic structure of the north-central Chilean convergent margin: Subduction erosion of a paleomagmatic arc, *Geophys. Res. Lett.*, **41**(5), 1523–1529, doi:10.1002/2013GL058729.

Crotwell, H. P., Owens, T. J., and Ritsema, J., 1999. The TauP Toolkit: Flexible Seismic Travel-time and Ray-path Utilities, *Seismol. Res. Lett.*, **70**(2), 154–160, doi:10.1785/gssrl.70.2.154.

D'Amico, S., Koper, K. D., Herrmann, R. B., Akinci, A., and Malagnini, L., 2010. Imaging the rupture of the Mw 6.3 April 6, 2009 L'Aquila, Italy earthquake using back-projection of teleseismic P-waves, *Geophys. Res. Lett.*, **37**(3), 1–5, doi:10.1029/2009GL042156.

Danielson, J. and Gesch, D., 2011. Global Multi-resolution Terrain Elevation Data 2010(GMTED2010), *U.S. Geol. Surv. Open-File Rep. 2011–1073*, **2010**, 26.

Das, S. and Aki, K., 1977. Fault plane with barriers: A versatile earthquake model, *J. Geophys. Res.*, **82**(36), 5658–5670, doi:10.1029/JB082i036p05658.

DeMets, C., Gordon, R. G., and Argus, D. F., 2010. Geologically current plate motions, *Geophys. J. Int.*, **181**(1), 1–80, doi:10.1111/j.1365-246X.2009.04491.x.

Dunham, E. M., Belanger, D., Cong, L., and Kozdon, J. E., 2011. Earthquake Ruptures with Strongly Rate-Weakening Friction and Off-Fault Plasticity, Part 2: Nonplanar Faults, *Bull. Seismol. Soc. Am.*, **101**(5), 2308–2322, doi:10.1785/0120100076.

Duputel, Z., Agram, P. S., Simons, M., Minson, S. E., and Beck, J. L., 2014. Accounting for prediction uncertainty when inferring subsurface fault slip, *Geophys. J. Int.*, **197**(1), 464–482, doi:10.1093/gji/ggt517.

Engdahl, E. R., 2002. Global seismicity: 1900-1999, *Int. Handb. Earthq. Eng. Seismol.*, pp. 665–690.

Fan, W. and Shearer, P. M., 2015. Detailed rupture imaging of the 25 April 2015 Nepal earthquake using teleseismic P waves, *Geophys. Res. Lett.*, **42**(14), 5744–5752, doi:10.1002/2015GL064587.

Fan, W. and Shearer, P. M., 2016. Local near instantaneously dynamically triggered aftershocks of large earthquakes, *Science*, **353**(6304), 1133–1136, doi:10.1126/science.aag0013.

Fan, W. and Shearer, P. M., 2017. Investigation of Backprojection Uncertainties With M6 Earthquakes, *J. Geophys. Res. Solid Earth*, **122**(10), 7966–7986, doi:10.1002/2017JB014495.

Fan, W., Shearer, P. M., Ji, C., and Bassett, D., 2016. Multiple branching rupture of the 2009 Tonga-Samoa earthquake, *J. Geophys. Res. Solid Earth*, **121**(8), 5809–5827, doi:10.1002/2016JB012945.

Fan, W., Bassett, D., Jiang, J., Shearer, P. M., and Ji, C., 2017. Rupture evolution of the 2006 Java tsunami earthquake and the possible role of splay faults, *Tectonophysics*, **721**, 143–150, doi:10.1016/j.tecto.2017.10.003.

Fielding, E. J., Sladen, A., Li, Z., Avouac, J.-P., Burgmann, R., and Ryder, I., 2013. Kinematic fault slip evolution source models of the 2008 M7.9 Wenchuan earthquake in China from SAR interferometry, GPS and teleseismic analysis and implications for Longmen Shan tectonics, *Geophys. J. Int.*, **194**(2), 1138–1166, doi:10.1093/gji/ggt155.

Fukahata, Y., Yagi, Y., and Rivera, L., 2014. Theoretical relationship between back-projection imaging and classical linear inverse solutions, *Geophys. J. Int.*, **196**(1), 552–559, doi:10.1093/gji/ggt392.

Fukuyama, E. and Madariaga, R., 1998. Rupture dynamics of a planar fault in a 3d elastic medium: Rate- and slip-weakening friction, *Bull. Seismol. Soc. Am.*, **88**(1), 1.

Gardi, A., Lemoine, A., Madariaga, R., and Campos, J., 2006. Modeling of stress transfer in the Coquimbo region of central Chile, *J. Geophys. Res. Solid Earth*, **111**(4), 1–10, doi:10.1029/2004JB003440.

Grandin, R., Vallée, M., Satriano, C., Lacassin, R., Klinger, Y., Simoes, M., and Bollinger, L., 2015. Rupture process of the M w = 7.9 2015 Gorkha earthquake

(Nepal): Insights into Himalayan megathrust segmentation, *Geophys. Res. Lett.*, **42**(20), 8373–8382, doi:10.1002/2015GL066044.

Guatteri, M. and Spudich, P., 1998. Coseismic temporal changes of slip direction: the effect of absolute stress on dynamic rupture, *Bull. Seismol. Soc. Am.*, **88**(3), 777–789.

Gusev, A. A. and Pavlov, V. M., 1991. Deconvolution of squared velocity waveform as applied to the study of a noncoherent short-period radiator in the earthquake source, *Pure Appl. Geophys. PAGEOPH*, **136**(2-3), 235–244, doi:10.1007/BF00876375.

Hartzell, S., Liu, P., and Mendoza, C., 1996. The 1994 Northridge, California, earthquake: Investigation of rupture velocity, risetime, and high-frequency radiation, *J. Geophys. Res. Solid Earth*, **101**(B9), 20091–20108, doi:10.1016/j.biopsycho.2012.07.004.

Hartzell, S., Mendoza, C., Ramirez-Guzman, L., Zeng, Y., and Mooney, W., 2013. Rupture History of the 2008 M w 7.9 Wenchuan, China, Earthquake: Evaluation of Separate and Joint Inversions of Geodetic, Teleseismic, and Strong-Motion Data, *Bull. Seismol. Soc. Am.*, **103**(1), 353–370, doi:10.1785/0120120108.

Hartzell, S. H. and Heaton, T. H., 1983. Inversion of strong ground motion and teleseismic waveform data for the fault rupture history of the 1979 imperial valley, california, earthquake, *Bull. Seismol. Soc. Am.*, **73**(6A), 1553.

Hashimoto, M., Enomoto, M., and Fukushima, Y., 2010. Coseismic Deformation from the 2008 Wenchuan, China, Earthquake Derived from ALOS/PALSAR Images, *Tectonophysics*, **491**(1-4), 59–71, doi:10.1016/j.tecto.2009.08.034.

Hayes, G. P., Wald, D. J., and Johnson, R. L., 2012. Slab1.0: A three-dimensional model of global subduction zone geometries, *J. Geophys. Res. Solid Earth*, **117**(1), 1–15, doi:10.1029/2011JB008524.

Hicks, S., Rychert, C., Harmon, N., Bogiaztis, P., Kendall, N., Schlaphorst, D., Abercrombie, R., Zahradnik, J., Okuwaki, R., Yagi, Y., and Shimizu, K., In prep. A

reversing super-shear rupture during the 2016 Mw 7.1 Romanche transform fault earthquake.

Holtkamp, S. and Brudzinski, M. R., 2014. Megathrust earthquake swarms indicate frictional changes which delimit large earthquake ruptures, *Earth Planet. Sci. Lett.*, **390**, 234–243, doi:10.1016/j.epsl.2013.10.033.

Huang, H., Xu, W., Meng, L., Bürgmann, R., and Baez, J. C., 2017. Early aftershocks and afterslip surrounding the 2015 Mw 8.4 Illapel rupture, *Earth Planet. Sci. Lett.*, **457**, 282–291, doi:10.1016/j.epsl.2016.09.055.

Hubbard, J. and Shaw, J. H., 2009. Uplift of the Longmen Shan and Tibetan plateau, and the 2008 Wenchuan (M = 7.9) earthquake, *Nature*, **458**(7235), 194–197, doi:10.1038/nature07837.

Hubbard, J., Shaw, J. H., and Klinger, Y., 2010. Structural Setting of the 2008 Mw 7.9 Wenchuan, China, Earthquake, *Bull. Seismol. Soc. Am.*, **100**(5B), 2713–2735, doi:10.1785/0120090341.

Husseini, M. I., Jovanovich, D. B., Randall, M. J., and Freund, L. B., 1975. The fracture energy of earthquakes, *Geophys. J. Int.*, **43**(2), 367–385, doi:10.1111/j.1365-246X.1975.tb00640.x.

Ide, S. and Aochi, H., 2005. Earthquakes as multiscale dynamic ruptures with heterogeneous fracture surface energy, *J. Geophys. Res. Solid Earth*, **110**(B11), 1–10, doi:10.1029/2004JB003591.

Ishii, M., Shearer, P. M., Houston, H., and Vidale, J. E., 2005. Extent, duration and speed of the 2004 Sumatra-Andaman earthquake imaged by the Hi-Net array, *Nature*, **435**(7044), 933–936, doi:10.1038/nature03675.

Ishii, M., Shearer, P. M., Houston, H., and Vidale, J. E., 2007. Teleseismic P wave imaging of the 26 December 2004 Sumatra-Andaman and 28 March 2005 Sumatra

earthquake ruptures using the Hi-net array, *J. Geophys. Res. Solid Earth*, **112**(11), 1–16, doi:10.1029/2006JB004700.

Ji, C., Wald, D. J., and Helmberger, D. V., 2002. Source Description of the 1999 Hector Mine, California, Earthquake, Part I: Wavelet Domain Inversion Theory and Resolution Analysis, *Bull. Seismol. Soc. Am.*, **92**(4), 1192–1207, doi:10.1785/0120000916.

Kakehi, Y. and Irikura, K., 1996. Estimation of high-frequency wave radiation areas on the fault plane by the envelope inversion of acceleration seismograms, *Geophys. J. Int.*, **125**(3), 892–900, doi:10.1111/j.1365-246X.1996.tb06032.x.

Kakehi, Y. and Irikura, K., 1997. High-frequency radiation process during earthquake faulting-envelope inversion of acceleration seismograms from the 1993 Hokkaido-Nansei-Oki, Japan, Earthquake, *Bull. Seismol. Soc. Am.*, **87**(4), 904–917.

Kakehi, Y., Irikura, K., and Hoshiba, M., 1996. Estimation of High-frequency Wave Radiation Areas on the Fault Plane of the 1995 Hyogo-ken Nanbu Earthquake by the Envelope Inversion of Acceleration Seismograms., *J. Phys. Earth*, **44**(5), 505–517, doi:10.4294/jpe1952.44.505.

Kaneko, Y., Avouac, J. P., and Lapusta, N., 2010. Towards inferring earthquake patterns from geodetic observations of interseismic coupling, *Nat. Geosci.*, **3**(5), 363–369, doi:10.1038/ngeo843.

Kase, Y. and Day, S. M., 2006. Spontaneous rupture processes on a bending fault, *Geophys. Res. Lett.*, **33**(10), L10302, doi:10.1029/2006GL025870.

Kelleher, J. and McCann, W., 1976. Buoyant Zones , Great Earthquakes , and Unstable Boundaries of Subduction to a low level Marianas-Bonins the tions of subduction appear interact with Tonga-Kermadec arc Katsumata and offsets in the Sykes of active depth and of the margin , lithosphere Pac, *J. Geophys. Res.*, **81**(26), 4885–4896, doi:10.1029/JB081i026p04885.

Kennett, B. L. N., Engdahl, E. R., and Buland, R., 1995. Constraints on seismic velocities in the Earth from traveltimes, *Geophys. J. Int.*, **122**(1), 108–124, doi:10.1111/j.1365-246X.1995.tb03540.x.

Kikuchi, M. and Kanamori, H., 1991. Inversion of complex body waves-III, *Bull. Seismol. Soc. Am.*, **81**(6), 2335–2350.

King, G. and Nábělek, J., 1985. Role of Fault Bends in the Initiation and Termination of Earthquake Rupture, *Science*, **228**(4702), 984–987, doi:10.1126/science.228.4702.984.

Kiser, E. and Ishii, M., 2011. The 2010 mw 8.8 chile earthquake: Triggering on multiple segments and frequency-dependent rupture behavior, *Geophys. Res. Lett.*, **38**(7), doi:10.1029/2011GL047140.

Kiser, E. and Ishii, M., 2013. Hidden aftershocks of the 2011 Mw 9.0 Tohoku, Japan earthquake imaged with the backprojection method, *J. Geophys. Res. Solid Earth*, **118**(10), 5564–5576, doi:10.1002/2013JB010158.

Kiser, E. and Ishii, M., 2017. Back-Projection Imaging of Earthquakes, *Annu. Rev. Earth Planet. Sci.*, **45**(1), 271–299, doi:10.1146/annurev-earth-063016-015801.

Kiser, E., Ishii, M., Langmuir, C. H., Shearer, P. M., and Hirose, H., 2011. Insights into the mechanism of intermediate-depth earthquakes from source properties as imaged by back projection of multiple seismic phases, *J. Geophys. Res. Solid Earth*, **116**(6), 1–26, doi:10.1029/2010JB007831.

Kohler, M. D., Heaton, T. H., and Bradford, S. C., 2007. Propagating Waves in the Steel, Moment-Frame Factor Building Recorded during Earthquakes, *Bull. Seismol. Soc. Am.*, **97**(4), 1334–1345, doi:10.1785/0120060148.

Koper, K. D., Hutko, A. R., Lay, T., and Sufri, O., 2012. Imaging short-period seismic radiation from the 27 February 2010 Chile (MW 8.8) earthquake by back-projection of P , PP , and PKIKP waves, *J. Geophys. Res. Solid Earth*, **117**(B2), 1–16, doi:10.1029/2011JB008576.

Krüger, F. and Ohrnberger, M., 2005. Tracking the rupture of the Mw = 9.3 Sumatra earthquake over 1,150 km at teleseismic distance, *Nature*, **435**(June), 937–939, doi:10.1038/nature03696.

Laske, G., Masters, G., Ma, Z., and Pasyanos, M., 2013. Update on CRUST1. 0—A 1-degree global model of Earth's crust, *EGU Gen. Assem.*, **15**, 2658.

Lay, T., Kanamori, H., Ammon, C. J., Koper, K. D., Hutko, A. R., Ye, L., Yue, H., and Rushing, T. M., 2012. Depth-varying rupture properties of subduction zone megathrust faults, *J. Geophys. Res. Solid Earth*, **117**(B4), 1–12, doi:10.1029/2011JB009133.

Lemoine, A., Madariaga, R., and Campos, J., 2001. Evidence for earthquake interaction in central Chile: the July 1997-September 1998 Sequence, *Geophys. Res. Lett.*, **28**(14), 2743–2746, doi:10.1029/2000GL012314.

Liu-Zeng, J., Sun, J., Wang, P., Hudnut, K. W., Ji, C., Zhang, Z., Xu, Q., and Wen, L., 2012. Surface ruptures on the transverse Xiaoyudong fault: A significant segment boundary breached during the 2008 Wenchuan earthquake, China, *Tectonophysics*, **580**, 218–241, doi:10.1016/j.tecto.2012.09.024.

Llenos, A. L., McGuire, J. J., and Ogata, Y., 2009. Modeling seismic swarms triggered by aseismic transients, *Earth Planet. Sci. Lett.*, **281**(1-2), 59–69, doi:10.1016/j.epsl.2009.02.011.

Lomnitz, C., 2004. Major Earthquakes of Chile: A Historical Survey, 1535-1960, *Seismol. Res. Lett.*, **75**(3), 368–378, doi:10.1785/gssrl.75.3.368.

Madariaga, R., 1977. High-frequency radiation from crack (stress drop) models of earthquake faulting, *Geophys. J. Int.*, **51**(3), 625–651, doi:10.1111/j.1365-246X.1977.tb04211.x.

Madariaga, R., Ampuero, J. P., and Adda-Bedia, M., 2006. Seismic radiation from simple models of earthquakes, in *Earthquakes Radiated Energy Phys. Faulting*, no. 1999, pp. 223–236, doi:10.1029/170GM23.

Mai, P. M., Galis, M., Thingbaijam, K. K. S., Vyas, J. C., and Dunham, E. M., 2017. Accounting for Fault Roughness in Pseudo-Dynamic Ground-Motion Simulations, *Pure Appl. Geophys.*, **174**(9), 3419–3450, doi:10.1007/s00024-017-1536-8.

McFadden, P. L., Drummond, B. J., and Kravis, S., 1986. The Nth-root stack: Theory, applications, and examples, *Geophysics*, **51**(10), 1879–1892, doi:10.1190/1.1442045.

Melgar, D., Fan, W., Riquelme, S., Geng, J., Liang, C., Fuentes, M., Vargas, G., Allen, R. M., Shearer, P. M., and Fielding, E. J., 2016. Slip segmentation and slow rupture to the trench during the 2015, M w 8.3 Illapel, Chile earthquake, *Geophys. Res. Lett.*, **43**(3), 961–966, doi:10.1002/2015GL067369.

Meng, L., Inbal, A., and Ampuero, J.-P., 2011. A window into the complexity of the dynamic rupture of the 2011 Mw 9 Tohoku-Oki earthquake, *Geophys. Res. Lett.*, **38**(7), 1–6, doi:10.1029/2011GL048118.

Meng, L., Ampuero, J.-P., Sladen, A., and Rendon, H., 2012a. High-resolution back-projection at regional distance: Application to the Haiti M 7.0 earthquake and comparisons with finite source studies, *J. Geophys. Res. Solid Earth*, **117**(B4), 1–16, doi:10.1029/2011JB008702.

Meng, L., Ampuero, J.-P., Stock, J., Duputel, Z., Luo, Y., and Tsai, V. C., 2012b. Earthquake in a Maze: Compressional Rupture Branching During the 2012 Mw 8.6 Sumatra Earthquake, *Science*, **337**(6095), 724–726, doi:10.1126/science.1224030.

Meng, L., Zhang, A., and Yagi, Y., 2016. Improving back projection imaging with a novel physics-based aftershock calibration approach: A case study of the 2015 Gorkha earthquake, *Geophys. Res. Lett.*, **43**(2), 628–636, doi:10.1002/2015GL067034.

Meng, L., Bao, H., Huang, H., Zhang, A., Bloore, A., and Liu, Z., 2018. Double pincer movement: Encircling rupture splitting during the 2015 mw 8.3 illapel earthquake, *Earth Planet. Sci. Lett.*, **495**, 164 – 173, doi:https://doi.org/10.1016/j.epsl.2018.04.057.

Métois, M., Vigny, C., Socquet, A., Delorme, A., Morvan, S., Ortega, I., and Valderas-Bermejo, C. M., 2013. GPS-derived interseismic coupling on the subduction and seismic hazards in the Atacama region, Chile, *Geophys. J. Int.*, **196**(2), 644–655, doi:10.1093/gji/ggt418.

Métois, M., Vigny, C., and Socquet, A., 2016. Interseismic Coupling, Megathrust Earthquakes and Seismic Swarms Along the Chilean Subduction Zone (38°–18°S), *Pure Appl. Geophys.*, **173**(5), 1431–1449, doi:10.1007/s00024-016-1280-5.

Michel, R. and Avouac, J.-P., 2002. Deformation due to the 17 August 1999 Izmit, Turkey, earthquake measured from SPOT images, *J. Geophys. Res. Solid Earth*, **107**(B4), ETG 2–1–ETG 2–6, doi:10.1029/2000JB000102.

Mikumo, T. and Miyatake, T., 1978. Dynamical rupture process on a three-dimensional fault with non-uniform frictions and near-field seismic waves, *Geophys. J. Int.*, **54**(2), 417–438, doi:10.1111/j.1365-246X.1978.tb04267.x.

Minson, S. E., Simons, M., and Beck, J. L., 2013. Bayesian inversion for finite fault earthquake source models I-theory and algorithm, *Geophys. J. Int.*, **194**(3), 1701–1726, doi:10.1093/gji/ggt180.

Miyatake, T., 1992. Reconstruction of dynamic rupture process of an earthquake with constraints of kinematic parameters, *Geophys. Res. Lett.*, **19**(4), 349–352, doi:10.1029/92GL00082.

Moreno, M., Rosenau, M., and Oncken, O., 2010. 2010 Maule earthquake slip correlates with pre-seismic locking of Andean subduction zone, *Nature*, **467**(7312), 198–202, doi:10.1038/nature09349.

Muirhead, K. J. and Datt, R., 1976. The N-th root process applied to seismic array data, *Geophys. J. Int.*, **47**(1), 197–210, doi:10.1111/j.1365-246X.1976.tb01269.x.

Nakahara, H., 2008. Seismogram Envelope Inversion for High-Frequency Seismic Energy

Radiation from Moderate-to-Large Earthquakes, in *Adv. Geophys.*, vol. 50, pp. 401–426, doi:10.1016/S0065-2687(08)00015-0.

Nishikawa, T. and Ide, S., 2017. Detection of earthquake swarms at subduction zones globally: Insights into tectonic controls on swarm activity, *J. Geophys. Res. Solid Earth*, **122**(7), 5325–5343, doi:10.1002/2017JB014188.

Oglesby, D., 2008. Rupture Termination and Jump on Parallel Offset Faults, *Bull. Seismol. Soc. Am.*, **98**(1), 440–447, doi:10.1785/0120070163.

Oglesby, D. D. and Mai, P. M., 2012. Fault geometry, rupture dynamics and ground motion from potential earthquakes on the North Anatolian Fault under the Sea of Marmara, *Geophys. J. Int.*, **188**(3), 1071–1087, doi:10.1111/j.1365-246X.2011.05289.x.

Ohnaka, M. and Yamashita, T., 1989. A cohesive zone model for dynamic shear faulting based on experimentally inferred constitutive relation and strong motion source parameters, *J. Geophys. Res.*, **94**(B4), 4089–4104, doi:10.1029/JB094iB04p04089.

Okubo, P. G. and Dieterich, J. H., 1984. Effects of Physical Fault Properties on Frictional Instabilities Produced Faults on of a preexisting Neverthe- at the possible, **89**, 5817–5827.

Okuwaki, R. and Yagi, Y., 2017. Rupture Process During the Mw8.1 2017 Chiapas Mexico Earthquake: Shallow Intraplate Normal Faulting by Slab Bending, *Geophys. Res. Lett.*, **44**(23), 11,816–11,823, doi:10.1002/2017GL075956.

Okuwaki, R. and Yagi, Y., 2018. Role of geometric barriers in irregular-rupture evolution during the 2008 Wenchuan earthquake, *Geophys. J. Int.*, **212**(3), 1657–1664, doi:10.1093/gji/ggx502.

Okuwaki, R., Yagi, Y., and Hirano, S., 2014. Relationship between High-frequency Radiation and Asperity Ruptures, Revealed by Hybrid Back-projection with a Nonplanar Fault Model, *Sci. Rep.*, **4**(1), 7120, doi:10.1038/srep07120.

Okuwaki, R., Yagi, Y., Aránguiz, R., González, J., and González, G., 2016. Rupture Process During the 2015 Illapel, Chile Earthquake: Zigzag-Along-Dip Rupture Episodes, *Pure Appl. Geophys.*, **173**(4), 1011–1020, doi:10.1007/s00024-016-1271-6.

Okuwaki, R., Yagi, Y., Shimizu, K., and Aranguiz, R., In prep. Inchworm-like supershear rupture across geometric barriers during the 2018 Palu Indonesia earthquake.

Olson, A. H. and Apsel, R. J., 1982. Finite faults and inverse theory with applications to the 1979 imperial valley earthquake, *Bull. Seismol. Soc. Am.*, **72**(6A), 1969.

Pardo, M., Comte, D., Monfret, T., Boroschek, R., and Astroza, M., 2002. The October 15, 1997 Punitaqui earthquake (Mw=7.1): A destructive event within the subducting Nazca plate in the Central Chile, *Tectonophysics*, **345**(1-4), 199–210, doi:10.1016/S0040-1951(01)00213-X.

Quin, H., 1990. Dynamic stress drop and rupture dynamics of the October 15, 1979 Imperial Valley, California, earthquake, *Tectonophysics*, **175**(1-3), 93–117, doi:10.1016/0040-1951(90)90132-R.

Ruiz, S., Metois, M., Fuenzalida, A., Ruiz, J., Leyton, F., Grandin, R., Vigny, C., Madariaga, R., and Campos, J., 2014. Intense foreshocks and a slow slip event preceded the 2014 Iquique Mw8.1 earthquake, *Science (80-.).*, **1165**(6201), 1165–1169, doi:10.1126/science.1256074.

Satriano, C., Kiraly, E., Bernard, P., and Vilotte, J.-P., 2012. The 2012 Mw 8.6 Sumatra earthquake: Evidence of westward sequential seismic ruptures associated to the reactivation of a N-S ocean fabric, *Geophys. Res. Lett.*, **39**(15), 1–6, doi:10.1029/2012GL052387.

Satriano, C., Dionicio, V., Miyake, H., Uchida, N., Vilotte, J. P., and Bernard, P., 2014. Structural and thermal control of seismic activity and megathrust rupture dynamics in subduction zones: Lessons from the Mw 9.0, 2011 Tohoku earthquake, *Earth Planet. Sci. Lett.*, **403**, 287–298, doi:10.1016/j.epsl.2014.06.037.

Sekiguchi, H., 2000. Fault Geometry at the Rupture Termination of the 1995 Hyogo-ken Nanbu Earthquake, *Bull. Seismol. Soc. Am.*, **90**(1), 117–133, doi:10.1785/0119990027.

Shen, Z.-K., Sun, J., Zhang, P., Wan, Y., Wang, M., Bürgmann, R., Zeng, Y., Gan, W., Liao, H., and Wang, Q., 2009. Slip maxima at fault junctions and rupturing of barriers during the 2008 Wenchuan earthquake, *Nat. Geosci.*, **2**(10), 718–724, doi:10.1038/ngeo636.

Shi, Z. and Day, S. M., 2013. Rupture dynamics and ground motion from 3-D rough-fault simulations, *J. Geophys. Res. Solid Earth*, **118**(3), 1122–1141, doi:10.1002/jgrb.50094.

Shimizu, K., Yagi, Y., Okuwaki, R., and Fukahata, Y., In prep. Development of an inversion method to extract information on fault geometry from teleseismic data, *Geophys. J. Int.*.

Snieder, R. and Şafak, E., 2006. Extracting the building response using seismic interferometry: Theory and application to the Millikan Library in Pasadena, California, *Bull. Seismol. Soc. Am.*, **96**(2), 586–598, doi:10.1785/0120050109.

Spudich, P. and Frazer, L., 1984. Use of ray theory to calculate high-frequency radiation from earthquake sources having spatially variable rupture velocity and stress drop, *Bull. Seismol. Soc. Am.*, **74**(6), 2061–2082.

Suzuki, M. and Yagi, Y., 2011. Depth dependence of rupture velocity in deep earthquakes, *Geophys. Res. Lett.*, **38**(5), 1–5, doi:10.1029/2011GL046807.

Tassara, A. and Echaurren, A., 2012. Anatomy of the Andean subduction zone: Three-dimensional density model upgraded and compared against global-scale models, *Geophys. J. Int.*, **189**(1), 161–168, doi:10.1111/j.1365-246X.2012.05397.x.

Trifunac, M. D., 1974. A three-dimensional dislocation model for the San Fernando, California, earthquake of February 9, 1971, *Bull. Seismol. Soc. Am.*, **64**(I), 149–172.

Uchide, T., Yao, H., and Shearer, P. M., 2013. Spatio-temporal distribution of fault slip and high-frequency radiation of the 2010 El Mayor-Cucapah, Mexico earthquake, *J. Geophys. Res. Solid Earth*, **118**(4), 1546–1555, doi:10.1002/jgrb.50144.

Udías, A., Madariaga, R., Buforn, E., Muñoz, D., and Ros, M., 2012. The large Chilean historical earthquakes of 1647, 1657, 1730, and 1751 from contemporary documents, *Bull. Seismol. Soc. Am.*, **102**(4), 1639–1653, doi:10.1785/0120110289.

Vallée, M. and Satriano, C., 2014. Ten year recurrence time between two major earthquakes affecting the same fault segment, *Geophys. Res. Lett.*, **41**(7), 2312–2318, doi:10.1002/2014GL059465.

Walker, K. T., Ishii, M., and Shearer, P. M., 2005. Rupture details of the 28 March 2005 Sumatra M w 8.6 earthquake imaged with teleseismic P waves, *Geophys. Res. Lett.*, **32**(24), L24303, doi:10.1029/2005GL024395.

Wan, Y., Shen, Z.-K., Bürgmann, R., Sun, J., and Wang, M., 2017. Fault geometry and slip distribution of the 2008 M w 7.9 Wenchuan, China earthquake, inferred from GPS and InSAR measurements, *Geophys. J. Int.*, **208**(2), 748–766, doi:10.1093/gji/ggw421.

Wang, D. and Mori, J., 2011. Frequency-dependent energy radiation and fault coupling for the 2010 Mw8.8 Maule, Chile, and 2011 Mw9.0 Tohoku, Japan, earthquakes, *Geophys. Res. Lett.*, **38**(22), 1–7, doi:10.1029/2011GL049652.

Wesnousky, S. G., 2008. Displacement and Geometrical Characteristics of Earthquake Surface Ruptures: Issues and Implications for Seismic-Hazard Analysis and the Process of Earthquake Rupture, *Bull. Seismol. Soc. Am.*, **98**(4), 1609–1632, doi:10.1785/0120070111.

Wright, T., Fielding, E., and Parsons, B., 2001. Triggered slip: Observations of the 17 August 1999 Izmit (Turkey) Earthquake using radar interferometry, *Geophys. Res. Lett.*, **28**(6), 1079–1082, doi:10.1029/2000GL011776.

Xu, X., Wen, X., Yu, G., Chen, G., Klinger, Y., Hubbard, J., and Shaw, J., 2009a. Coseismic reverse- and oblique-slip surface faulting generated by the 2008 Mw 7.9 Wenchuan earthquake, China, *Geology*, **37**(6), 515–518, doi:10.1130/G25462A.1.

Xu, Y., Koper, K. D., Sufri, O., Zhu, L., and Hutko, A. R., 2009b. Rupture imaging of the M w 7.9 12 May 2008 Wenchuan earthquake from back projection of teleseismic P waves, *Geochemistry, Geophys. Geosystems*, **10**(4), Q04006, doi:10.1029/2008GC002335.

Yagi, Y. and Fukahata, Y., 2011a. Introduction of uncertainty of green's function into waveform inversion for seismic source processes, *Geophys. J. Int.*, **186**(2), 711–720, doi:10.1111/j.1365-246X.2011.05043.x.

Yagi, Y. and Fukahata, Y., 2011b. Rupture process of the 2011 Tohoku-oki earthquake and absolute elastic strain release, *Geophys. Res. Lett.*, **38**(19), n/a–n/a, doi:10.1029/2011GL048701.

Yagi, Y. and Okuwaki, R., 2015. Integrated seismic source model of the 2015 Gorkha, Nepal, earthquake, *Geophys. Res. Lett.*, **42**(15), 6229–6235, doi:10.1002/2015GL064995.

Yagi, Y., Nakao, A., and Kasahara, A., 2012a. Smooth and rapid slip near the Japan Trench during the 2011 Tohoku-oki earthquake revealed by a hybrid back-projection method, *Earth Planet. Sci. Lett.*, **355-356**, 94–101, doi:10.1016/j.epsl.2012.08.018.

Yagi, Y., Nishimura, N., and Kasahara, A., 2012b. Source process of the 12 May 2008 Wenchuan, China, earthquake determined by waveform inversion of teleseismic body waves with a data covariance matrix, *Earth, Planets Sp.*, **64**(7), e13–e16, doi:10.5047/eps.2012.05.006.

Yagi, Y., Okuwaki, R., Enescu, B., Hirano, S., Yamagami, Y., Endo, S., and Komoro, T., 2014. Rupture process of the 2014 Iquique Chile earthquake in relation with the foreshock activity, *Geophys. Res. Lett.*, **41**(12), 4201–4206, doi:10.1002/2014GL060274.

Yao, H., Shearer, P. M., and Gerstoft, P., 2013. Compressive sensing of frequency-dependent seismic radiation from subduction zone megathrust ruptures, *Proc. Natl. Acad. Sci.*, **110**(12), 4512–4517, doi:10.1073/pnas.1212790110.

Ye, L., Lay, T., Kanamori, H., and Koper, K. D., 2013. Energy release of the 2013 Mw 8.3 Sea of Okhotsk earthquake and deep slab stress heterogeneity, *Science*, **341**(6152), 1380–1384, doi:10.1126/science.1242032.

Ye, L., Lay, T., Kanamori, H., and Koper, K. D., 2016a. Rapidly Estimated Seismic Source Parameters for the 16 September 2015 Illapel, Chile Mw8.3 Earthquake, *Pure Appl. Geophys.*, **173**(2), 321–332, doi:10.1007/s00024-015-1202-y.

Ye, L., Lay, T., Kanamori, H., and Rivera, L., 2016b. Rupture characteristics of major and great (Mw $\geq$ 7.0) megathrust earthquakes from 1990 to 2015: 2. Depth dependence, *J. Geophys. Res. Solid Earth*, **121**(2), 845–863, doi:10.1002/2015JB012427.

Yin, J., Yang, H., Yao, H., and Weng, H., 2016. Coseismic radiation and stress drop during the 2015 Mw 8.3 Illapel, Chile megathrust earthquake, *Geophys. Res. Lett.*, **43**(4), 1520–1528, doi:10.1002/2015GL067381.

Yin, J., Denolle, M. A., and Yao, H., 2018. Spatial and Temporal Evolution of Earthquake Dynamics: Case Study of the Mw 8.3 Illapel Earthquake, Chile, *J. Geophys. Res. Solid Earth*, pp. 1–24, doi:10.1002/2017JB014265.

Yu, G., Xu, X., Klinger, Y., Diao, G., Chen, G., Feng, X., Li, C., Zhu, A., Yuan, R., Guo, T., Sun, X., Tan, X., and An, Y., 2010. Fault-Scarp Features and Cascading-Rupture Model for the Mw 7.9 Wenchuan Earthquake, Eastern Tibetan Plateau, China, *Bull. Seismol. Soc. Am.*, **100**(5B), 2590–2614, doi:10.1785/0120090255.

Zeng, Y., Aki, K., and Teng, T.-L., 1993. Mapping of the high-frequency source radiation for the Loma Prieta Earthquake, California, *J. Geophys. Res. Solid Earth*, **98**(B7), 11981–11993, doi:10.1029/93JB00346.

Zhang, H. and Ge, Z., 2010. Tracking the Rupture of the 2008 Wenchuan Earthquake by Using the Relative Back-Projection Method, *Bull. Seismol. Soc. Am.*, **100**(5B), 2551–2560, doi:10.1785/0120090243.